Imperial College of Science, Technology and Medicine
Department of Civil and Environmental Engineering

Reconstructing flow from thermal wall imprints

Md Rakib Hossain

Supervised by

Dr. Maarten Van Reeuwijk
&
Dr. John Craske

Submitted in part fulfilment of the requirements for the degree of
Doctor of Philosophy in Civil and Environmental Engineering of the
Imperial College London, September 2021

Declaration & copyright

I hereby declare that all the work presented in this thesis is my own. Any contribution or work from others has been appropriately acknowledged or referenced.

Md Rakib Hossain

September 30, 2021

Acknowledgements

Thanks Maarten and John. I will be always grateful to both of you. You always push me to do some extra and fill my void with your valuable suggestions. Perhaps it is our weekly meetings that I will be missing the most in future.

I thank you all my lab mates, especially Ivo, Tom and Johanna for your caring response in any situation. I was lucky to have such kind and friendliest friends in these five years.

I gratefully acknowledge the UK Turbulence Consortium which is funded by the Environmental and Physical Sciences Research Council (EPSRC) through grant number EP/R029326/1 and the High Performance Computing service at Imperial College London for computational resources. I also acknowledge the Commonwealth Scholarship Commission in the UK for their funding.

I would like to thank my beloved Taslima and Tasnin for your continuous supports, sufferings and infinite love. Tasnin, I will always feel void for not being there in your childhood. Thanks both for understanding me.

Finally to my parents - Mom & Dad - I lost you both but you will be at my heart, forever. Thank you.

Abstract

This thesis develops data-driven flow reconstruction methods to reconstruct the velocity of plane Couette flow from wall temperature. We performed a Direct Numerical Simulation (DNS) for a heated plane Couette flow with imposed flux boundary condition at the bottom wall to create a data-set. Due to the the imposed flux the temperature at bottom wall is free and wall temperature patterns can develop. The focus of this thesis is on the investigations of the strong correlation between the flow velocity and the wall temperature. We analyse their joint probability density function and cross variance spectrum to develop a spectral linear regression model. This model successfully reconstructs wall shear stress from wall temperature except possibly at peaks. To reconstruct flow velocity from wall temperature, we apply flow decomposition modes such as the Proper Orthogonal Decomposition (POD) modes [Holmes et al., 2012]. We design test problems to develop a framework to reconstruct *gappy* fields with missing information. In this framework, we prescribe suitable regularisation for the under-determined *gappy* fields. We also develop a decomposition method - the subdomain POD method which divides a physical domain into a number of subdomains and then applies the POD method in each subdomain individually. This subdomain POD are locally optimised and inherits properties of the POD modes. In both cases, namely the POD and the subdomain POD method, the reconstructions are found to be in good agreement with the flow velocity obtained form the DNS. To develop data-driven methods with imposed physical constraints, we propose a linear dynamical model based on Orr-Sommerfeld-Squire [Kim and Bewley, 2007, Murray, 2006] system and the scalar transport equation. This model successfully reconstruct some of the key flow structures at $z^+ = 35$.

Contents

Nomenclature

$\boldsymbol{u}$	Velocity vector
$\langle \cdot \rangle$	Temporal-only averaging operator
$\mathbf{S}_j$	Transformed field using background profile $\mathbf{s^j}_b$
$\tilde{\mathbf{x}}$	Error vector
$\mathbf{C_y}$	Projection operator
$\mathbf{d}$	Disturbance vector
$\mathbf{r}$	Control vector
$\mathbf{s^j}_b$	Background profile for $\mathbf{s_j}$
$\mathbf{u}$	Velocity vector
$\mathbf{u}_e$	The estimated velocity
$\mathbf{v}$	Measurement noise
$\mathbf{x}$	State vector
$\mathbf{x}_e$	Estimated state vector
$\mathbf{y}$	Measurement vector

M System matrix

V State matrix

$\overline{(\cdot)}$ The standard spatio-temporal averaging operator

$\|\cdot\|_w$ A weighted $\ell_2 norm$

V State Matrix

A System matrix

a, b, p Parameters for the modulus of the parameter C

B Disturbance matrix

b_i^j ith temporal coefficient of subdomain POD modes corresponding to the subdomain j.

C Parameter of the spectral model

c The modulus of the parameter C

D Spatial domain

D_j Subdomain j

F Input matrix

f Right side vector

f_1 Forcing of the pendulum-cart system

h Channel height

K Kalman gain

L The length of the pendulum

$L^2(\cdot)$ Hilbert space

L_x Channel length

L_y	Channel width
m	Mask function
M,σ	Parameters for the phase of the parameter C
m_1	The mass of the cart
m_2	The mass of the pendulum
N	Number of modes
N_d	Number of subdomains
N_g	Number of grid points
N_q	Number of modes within each subdomain
N_s	Number of snapshots
n_x	Wavenumber in streamwise direction
n_y	Wavenumber in spanwise direction
P	Solution of the algebraic Riccati equation
p	Kinematic pressure
Q_d	Disturbance variance
Q_v	Measurement variance
q_w	Heat flux at bottom wall
R	Correlation operator
T	Total time
t	Time
$t^{(k)}$	k-th discrete time step

U Half of the streamwise velocity at Top wall

u Streamwise component of velocity

U_b Transformed field using background profile θ_b^j

u_b Background profile for u

v Spanwise component of velocity

w Wall-normal component of velocity

w Weight for the norm $\|\cdot\|_w$

x Streamwise coordinate

y Spanwise coordinate

z Wall-normal coordinate

Greek Symbols

Ψ_l Eigenvectors of $V^T V$

φ_k Eigenvectors of VV^T

$\theta^{(k)}$ Scalar snapshot at time $t^{(k)}$ arranged in a long vector

α Regularisation parameter

χ_w Estimated wall temperature

γ Relative error

$\hat{\psi}^j_{in_y}$ Fourier coefficient of the ith subdomain POD mode of the subdomain D_j

$\hat{\varphi}_{nn_y}$ Fourier coefficient of POD modes φ_{nn_y}

κ Thermal diffusivity of the fluid

λ_i Eigenvalues

λ_y The spanwise wavelength

μ The Cumulative energy fraction

ν Kinematic viscosity of the fluid

ψ_i^j ith subdomain POD mode of the subdomain D_j

Σ Matrix with diagonal elements σ_i

σ_i Singular values of V

τ_w Streamwise component of wall shear stress

θ,ϑ Passive scalar/temperature

Θ_b^j Transformed field using background profile θ_b^j

θ_b^j Background profile for θ_j

θ^k Passive scalar/temperature at $t = t^k$

θ_j Restriction of θ within and on the subdomain D_j

θ_w Bottom wall temperature

φ_i POD modes

List of Tables

List of Figures

Chapter 1

Introduction

1.1 Motivation

More than half of the world population lives in cities and this proportion is expected to continue to increase in future [United Nations, 2019]. Due to this continuing urbanization, the interaction between the city dwellers and the ever changing urban climate is becoming increasingly important. Among others, an important research area is to enhance the capabilities in addressing the growing urban environmental risks (e.g. air pollution [Manisalidis et al., 2020], the urban heat island effects [Taha, 2004]), as these risks directly influence public health [United Nations, 2014]. According to the World Health Organization (WHO), air pollution alone causes one in nine deaths worldwide [World Health Organization, 2016], costing seven million lives per year. The environmental risks predominantly depend on the characteristics of air flow within street canopies. For example, strong winds can rapidly transport pollutants hundred of kilometers, whereas under weak wind conditions, pollutants tend to accumulate around their sources [Bergin et al., 2005]. Thus, to confront the environmental risks, it is essential to measure, to understand and to be capable of controlling the airflow in the urban environment.

To measure airflow, a number of different approaches have been employed in the literature, such as field measurements [Oke, 1988, Van Pul et al., 1994], physical models [Lateb et al., 2016] and numerical simulations [Kasagi et al., 1992, Nagano and Tagawa, 1995]. Among

Figure 1.1: Thermal images for two urban landscapes in Berlin, Germany [Oke et al., 2017].

these, field measurements and physical modelling are costly and experimental set up is time consuming. In addition, noisy results obtained from field measurements need filtering and thus lose information. Although field measurements are performed under real conditions utilising all possible phenomena such as shear, buoyancy and humidity, the number of measurement points are limited [Inagaki et al., 2013, Montazeri and Blocken, 2013]. Besides, weather status can change rapidly and repetition of experiments under identical conditions is impossible [Lateb et al., 2016]. Physical models are performed in controlled environments and thus the receptivity of the experiment can be ensured [Barlow and Coceal, 2009]. However, the results from physical models are subject to noise and there are technical difficulties involved in the measurement procedure [Blocken et al., 2008], such as, the measurement of skin friction.

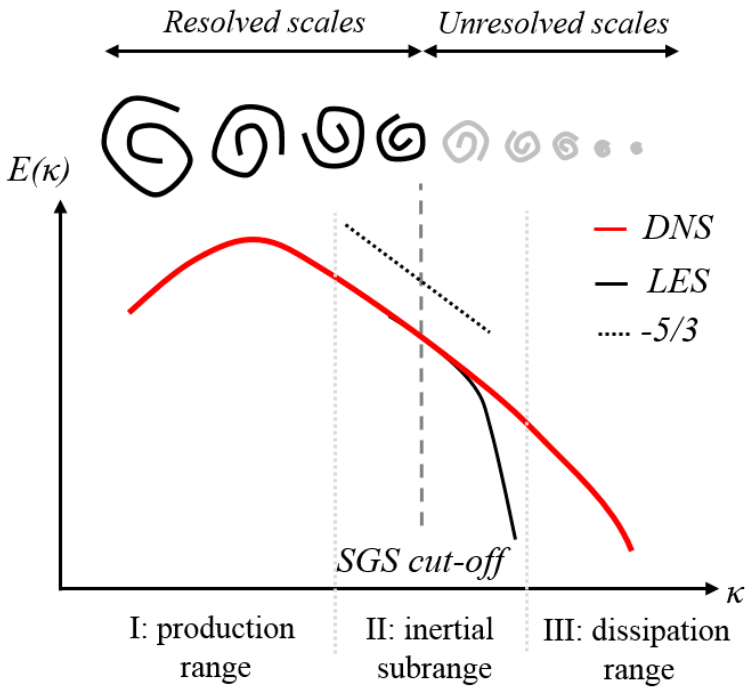

Figure 1.2: A diagram showing the scales resolved by the DNS and LES [Ouro Barba et al., 2017]. The DNS resolves scales upto Kolmogorov scale in the dissipation range whereas the LES resolves only the large eddies and the remaining unresolved eddies (shown with SGS cut-off) are needed to be modelled. At the top of the diagram the size of eddies are reducing from the production range to the dissipation range.

Another frequently used measurement approach is numerical simulation, which can provide detailed spatial and temporal flow information. Unlike field measurements, exact boundary conditions and parameters can be set according to a given problem. Two frequently used simulation approaches in fluid dynamics are − direct numerical simulation (DNS) [Pirozzoli et al., 2014] and large eddy simulation (LES) [Podvin et al., 2006]. In DNS, the whole range of spatial and temporal scales upto Kolmogorov length scale are resolved. Despite the requirement of high computational cost, DNS provide reliable data for the validation of turbulence models and is a necessary tool to discover fundamental physics of turbulence. On the other hand, LES ignores smaller length scales and resolves dynamically important larger scales only. The effect of such truncation is modelled to incorporate the dynamical interactions of neglected scales with largest scales. Since, it is not required to resolve all scales, LES is computationally cheaper than DNS. A schematic diagram showing the scales resolved by the DNS and the LES is presented in figure 1.2 using a energy spectrum.

To obtain accurate results while minimising computational costs, flow reconstruction techniques can be a useful tool to investigate the flows. Flow reconstruction techniques are methods that provide information of the states of a flow, such as velocity and temperature, from a set of limited observations. In many circumstances, the flow states may not be available throughout the physical domain or some of the states may be missing completely, and thus the flow reconstruction techniques are important in these situations. The advantages of reconstruction techniques are: (a) they require limited observations which are simpler to measure and (b) they are cost effective. Some examples of flow reconstruction are the estimation of velocity fields from wall pressure measurements [Bui-Thanh et al., 2004], flow controls by reducing wall friction [Lee et al., 2001] and wall thermal imprints [Inagaki et al., 2013]. The similarity between these examples of flow reconstruction techniques is that they estimate/control the flow using wall data. But, among these partial observations, that is pressure, skin friction and thermal imprints, thermal imprints can provide more detailed spatial information compared to the others. For example, to measure the pressure at the wall of an aerodynamic body, the available spatial information (degrees of freedom) is the same as the number of sensors used, whereas a digital infrared camera can capture millions of pixels on a 2D plane. Figure 1.1 shows an example of thermal imaging in urban landscapes chosen from the literature. Another motivation of using wall thermal imprints as the limited observation is the strong correlation between the thermal dynamics and the driving air flow [Antonia et al., 1988]. The wall thermal imprints can be considered as the footprints of the turbulent flow around the wall.

Thermal image velocimetry (TIV) is an example of a flow reconstruction technique which uses wall thermal images as limited observations. In comparison to other flow visualization techniques, such as particle image velocimetry (PIV), the TIV is more robust when applied to the urban environment. The size of the measurement area for the PIV is reported to be limited to about $10m^2$ [Inagaki et al., 2013] due to the difficulties in tracking and controlling the particle distributions within the test area. On the other hand, the TIV can be applied over a large landscape in open environment. A schematic diagram is shown in figure 1.3 describing the TIV. The TIV requires a low cost infrared thermal camera to evaluate 2D airflow velocity distribution near a surface, such as the exterior of buildings, using a set of wall thermal imprints.

From these thermal imprints, advection velocity of the thermal patterns are evaluated. The advection velocity is the time rate of change at which the thermal patterns on the wall are moving. A regression line is then fit using advection velocity and flow velocity around the wall. The slope of the regression line is chosen as multiplier and finally, the multiplier is simply multiplied to the thermal patterns to obtain the flow velocity.

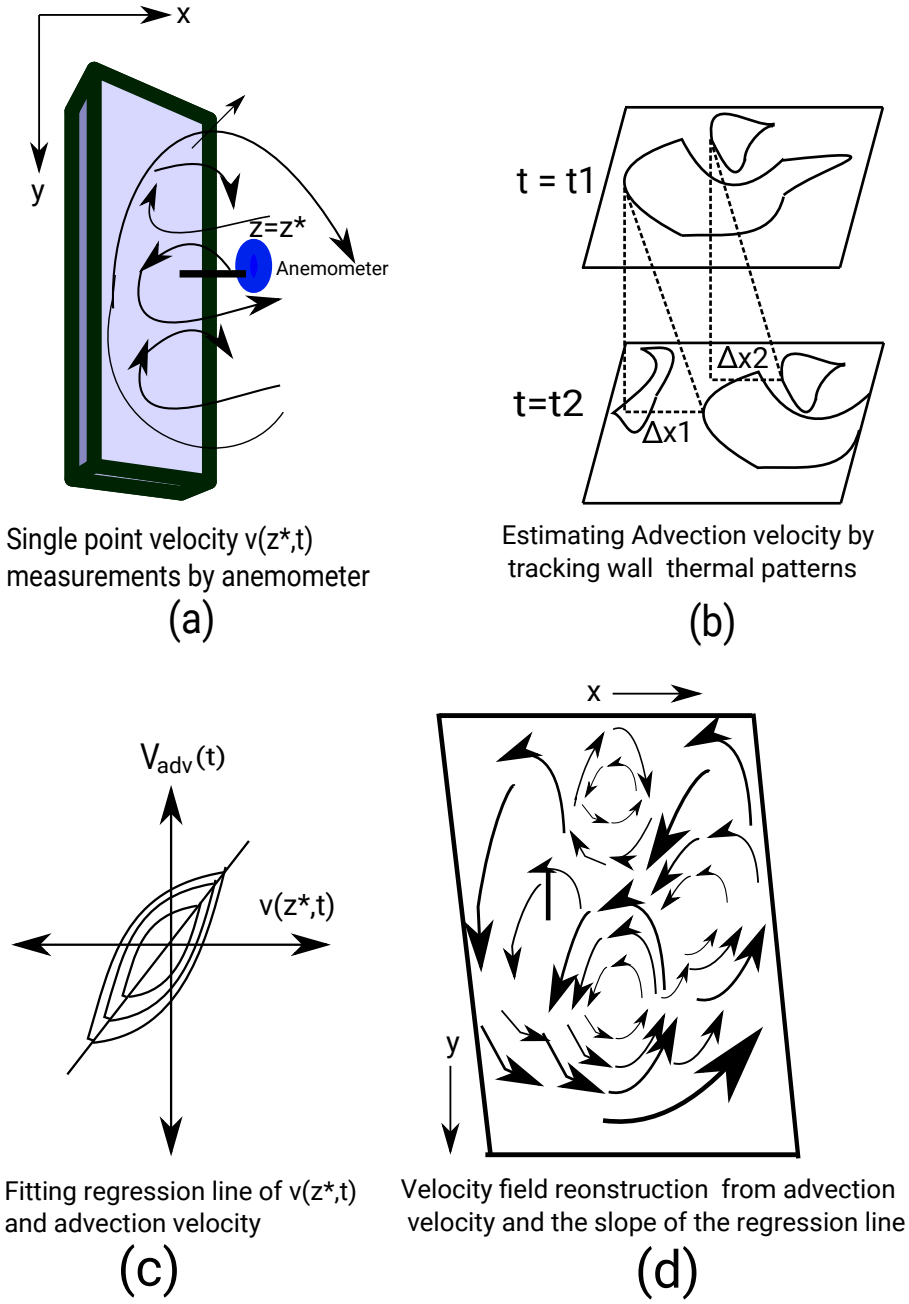

Figure 1.3: Schematic diagram describing TIV technique. Here, $v(z^*, t)$ is the velocity measured by anemometer at $z = z^*$, $\Delta x1$ and $\Delta x2$ are the displacements of thermal structures within time period $(t2 - t1)$ and V_{adv} is the advection velocity. The coordinate x and y is shown in the top left corner of the figure.

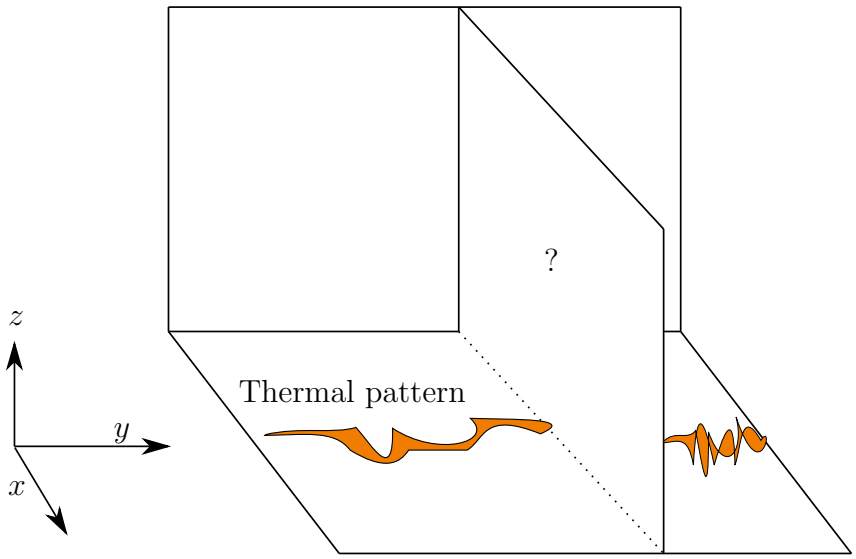

Figure 1.4: A schematic diagram of a cubic box visualizing the aim of the thesis. The temperature on the bottom wall are the limited observation. The objective is to obtain the flow information on the zx plane.

Although TIV technique can provide detailed spatial velocity distribution, its ability to reconstruct velocity far from the wall is limited. One inherent limitation of TIV is the use of linear regression which assumes the near wall linearity of flows. Far from the wall, velocity follows the well known log law and a linear analysis would not yield a good reconstruction of the velocity field in far wall region. TIV technique has been applied to reconstruct velocity field only 35mm away from the wall [Inagaki et al., 2013]. TIV technique also suffers from locality effects, especially if the physical domain contains stagnation points. In this case, reconstructed velocity would not be representative of the entire surface as local velocity at a stagnation point is zero. The other limitations of this technique are the difficulties in tracking complex patterns near any corners, conditions of the walls, buoyancy effects.

This thesis is based on the core idea of the TIV - *the thermal wall patterns are correlated with the turbulent flow structures near the wall.* The aim of the research is to use this correlation to get the turbulent flow structures near the wall. Correlation coefficient is the highest near to the wall and tends to decrease further away from the wall. Therefore, the important research questions are (1) how far from the wall can the turbulent flow structures be reconstructed? and (2) to what extent (accuracy of the reconstruction) reconstruction is possible? The aim of the current research are visualized in the figure 1.4 by an idealistic scheme of a cubic box - given

the thermal patterns on the bottom wall, what is flow field in the plane perpendicular to the bottom wall?

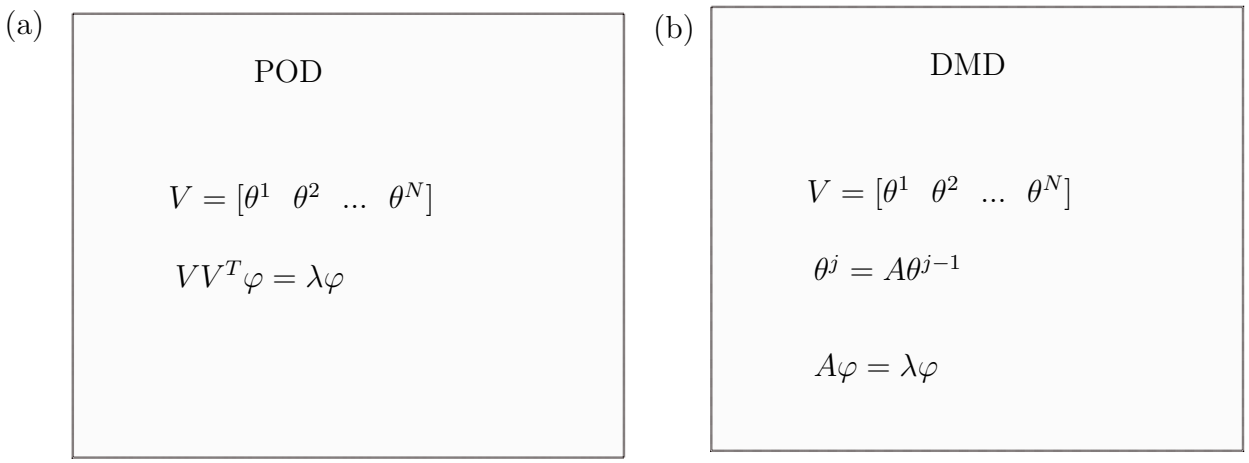

Figure 1.5: A diagram showing different flow decomposition methods (a) the POD mmodes are the eigenvectors of VV^T, where $V = [\theta^1 \quad \theta^2 \quad \dots \quad \theta^N]$ and θ^j are the observations at discrete time steps, (b) the DMD modes are the eigenvectors of the operator A, where A maps θ^{j-1} to θ^j.

Flow decomposition methods [Taira et al., 2017], e.g, proper orthogonal decomposition (POD) [Holmes et al., 2012, Moehlis et al., 2002] and dynamic mode decomposition (DMD) [Schmid, 2010, Taira et al., 2017], are two widely used methods to reconstruct flow fields from limited observation. These flow decomposition techniques are a tool of data-driven analysis. Generally, a flow decomposition method extract a set of modes from a data-set. The meaning of such modes depends on the particular decomposition method used. For example, POD uses correlation to extract modes from experimental/simulated data. POD modes are in fact, eigenmodes of the correlation matrix of a flow field. The decomposition technique POD at it heart is a statistical method that extracts the best features of a data set to represent it optimally (in an L_2 sense). A data set is expressed as a linear combination of POD modes and such a linear representation eases any further analysis/development while the dynamics of the data could be highly non-linear. On the other hand, in DMD it is assumed that the dynamics of a set of data is governed by a linear mapping (e.g. a tangent operator to non-linear dynamical operator) and the eigenmodes of this linear operators are DMD modes. Unlike POD, DMD modes are not orthogonal and can not be arranged in an order based on the energy they capture. However, DMD modes are efficient to present a dynamically important feature which

might not energetically important. To reconstruct flows using these decomposition modes, one need to know how these modes are modulated with time from a set of available full/partial measurements [Holmes et al., 2012]. It is also in practice to use flow decomposition modes to build up a dynamical model, as can be found in [Moehlis et al., 2002] where they used POD based dynamical model to analyse and determine some flow features of plane Couette flow ($Re = 400$). Figure 1.5(a,b) shows how the POD and the DMD modes are related to the flow observations, respectively.

Another important approach is the use of dynamical models. The data driven flow decomposition methods discussed earlier, do not take into account any dynamical relation but only extract some important features (modes) from a set of data. Use of dynamical models can thus be an attractive approach for flow reconstructions as it provides some physical constraints whereas observations can be assimilated into the model - which is still a data-driven approach. These models can be divided into two subgroups - linear and non-linear models. A description of the linear and non-linear models and flow control/estimation using these models can be found in [Kim and Bewley, 2007]. The non-linear models are expensive to solve as they required iterative procedures (e.g. adjoint method) [Giles and Pierce, 2000,Protas et al., 2004,Yamaleev et al., 2008]. An example of the linear model can be found in [Illingworth et al., 2018] which used Orr-Sommerfeld-squire model to reconstruct velocity field. The main advantage of using a linear model is that the linear control and estimation theory is readily applicable to the model. There are established methods, such as Kalman filter [Trentelman et al., 2002,Kim and Bewley, 2007] that can be used to estimate flow from partial observations.

In this thesis, we will reconstruct flow from partial observations. Linking back to TIV, in each case thermal wall imprints will be used as partial observations. We will investigate different flow decomposition methods and dynamical models using suitably chosen test problems, and will discuss the advantages and disadvantages of each method. With these methods/models, if succeeded, the limitations of TIV can be overcome and frameworks can be established for flow reconstructions away from wall using wall temperature.

1.2 Aims and objectives

The aim of the thesis is to reconstruct flow structures using wall thermal imprints. A series of objectives has been set to achieve the aim as listed below:

- **O1. Creating a data-set for flow reconstructions:** The objective is to obtain steady state DNS data-set of plane Couette flow and compare with analytic and published results.
- **O2. Inferring wall shear stress from wall temperature:** The objective is to develop a spectral model to reconstruct wall shear stress using the strong correlation between flow velocity and wall temperature.
- **O3. Flow reconstruction using data driven decomposition methods:** The objective is to use data driven decomposition method, such as the POD, to reconstruct the velocity field. The temporal amplitude of the modes are unknown at a given time and these temporal amplitudes are to be evaluated from the wall temperature.
- **O4. Flow reconstruction using dynamical models:** The objective is to estimate velocity field using dynamical models, such as Orr-Sommerfeld-Squire system [Illingworth et al., 2018] and wall temperature.

1.3 Outline of the thesis

In chapter 2, we perform a DNS of plane Couette flow at $Re_\tau = 263$ and verify the validity using published results. We build up a data-set which will be used in the remainder of the thesis. In chapter 3, we use a spectral model to estimate the wall shear stress from the wall temperatures and parameterise the model to reduce the degrees of freedom.

We discuss the POD method in chapter 4. The POD decomposes a flow field into a set of orthonormal modes and these modes can be ordered by the kinetic energy. That is, the kinetic energy(variance) of the first mode is higher than the second mode, the second mode contains

higher kinetic energy than the third mode and so on. We set up a number of test problems with increasing difficulty to test the performance of the POD modes for flow reconstructions. To reconstruct flow velocity from wall temperature, we choose suitable regularisation method to solve the resulting under-determined system. In chapter 5, we develop a subdomain POD method where the domain is divided into subdomains and the POD method is applied to each subdomain. These modes are different from the standard POD modes as the subdomain modes are locally optimised and are efficient to reconstruct the local flow structures. Here, we consider the same set of problems as in chapter 4 and compare the reconstructed flows using both the standard and subdomain POD modes. In chapter 4 and 5, we successfully reconstruct the streamwise component of the flow velocity using only wall temperature.

In Chapter 6, we use linear dynamical model [Illingworth et al., 2018] to reconstruct the flow velocity. The dynamical model provide a physical constraint, which is a new inclusion compared to the data-driven methods used in chapter 4 and 5. To estimate velocity field from wall temperature, we develop a dynamical model using the Orr-Sommerfeld-Squire system [Illingworth et al., 2018] and the scalar transport equation. In this chapter, the non-linear terms in the perturbed quantities is considered as the random forcing with finite variance. We use wall temperature to approximate the variance of this random forcing and flow velocity is estimated from the resulting response of the model.

Chapter 2

Creating a data-set for flow reconstruction using Direct Numerical Simulation

In this chapter, we create a data-set for flow reconstruction by performing Direct Numerical Simulation (DNS) of plane Couette flow with the top wall moving while keeping the bottom wall fixed. In addition, the bottom wall is subjected to a constant temperature flux q_w and the top wall is kept at a fixed temperature. We compare turbulence statistics obtained from DNS with other published results and find good agreement. We generate DNS data-sets which will be used in upcoming chapters to reconstruct the wall shear stress and the velocity field of plane Couette flow.

2.1 Direct numerical simulation

The DNS is performed with the code SPARKLE, which numerically integrates the incompressible Navier-Stokes equations [Craske and Van Reeuwijk, 2015]

$$\frac{\partial \mathbf{u}}{\partial t} + \mathbf{u} \cdot \nabla \mathbf{u} = -\nabla p + \nu \nabla^2 \mathbf{u}, \tag{2.1}$$

$$\nabla \cdot \mathbf{u} = 0, \tag{2.2}$$

$$\frac{\partial \theta}{\partial t} + \mathbf{u} \cdot \nabla \theta = \kappa \nabla^2 \theta. \tag{2.3}$$

Here, $\mathbf{x} = (x, y, z)^T$, where x, y and z are the streamwise, spanwise and wall normal directions, respectively, $\mathbf{u} = (u, v, w)^T$ is the flow velocity, p is the kinematic pressure and ν and κ are the kinematic viscosity and the thermal diffusivity of the fluid, respectively. SPARKLE is parallelised with a two-dimensional domain decomposition. Since the flow is homogeneous in the directions x and y, periodic boundary conditions are applied in this directions. The spatial operators are discretised using a symmetry preserving finite volume method [Verstappen and Veldman, 2003] which is accurate to fourth order. The variables are arranged on a staggered grid. Each control volume is centred on the location of the transported variable and fluxes are defined on the centre of each face. The time marching is implemented by using an adaptive third order explicit Adams-Bashforth numerical scheme.

DNS resolves the whole range of temporal and spatial scales from the Kolmogorov scale to the integral scale. The Kolmogorov scale η is determined by

$$\eta = \left(\nu^3/\epsilon\right)^{\frac{1}{4}} \tag{2.4}$$

where, ϵ is the rate of turbulent kinetic energy dissipation. For DNS, the spatial increment $\Delta\mathbf{x}$ should be considered less than η. Chapman estimated the number of grid points that is required to resolve up to the Kolmogorov scale as [Chapman, 1979]

$$N \sim Re^{9/4} \tag{2.5}$$

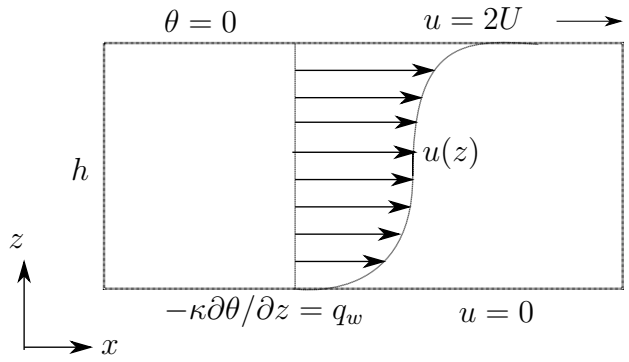

Figure 2.1: Schematic diagram of the simulated domain

where, $Re = 2U/L_x$ is the Reynolds number, $2U$ is the mean velocity and L_x is the streamwise length. Thus the DNS requires high computational cost and is not suitable for practical engineering applications. However, the DNS are used widely as a tool to understand the fundamental aspects of canonical flows and to develop/validate turbulence models.

2.2 Case setup

We perform Direct Numerical Simulation (DNS) of plane Couette flow, for which the bottom wall is static and the top wall is moving with velocity $2U$ (figure 2.1). In addition, the bottom wall is subjected to a constant temperature flux q_w and the top wall is kept at a fixed temperature. Due to the prescription of a fixed temperature flux, the temperature on the bottom wall is free. The dimensions of the cuboidal domain are $6h \times 3h \times h$, where h is the channel height. To simulate the flow, the computational domain is discretised into $864 \times 432 \times 432$ grid points. The mesh is uniform in all directions and no grid stretching is considered.

In the simulation, we assume that the Richardson number $Ri = g\beta q_w h^2/U^2 \ll 1$, where g, β and h are the gravitational acceleration, thermal expansion coefficient and domain height domain respectively. This assumption allows us to represent the temperature as a passive scalar [Kasagi et al., 1992].

Two averaging operators will be used. The first type is the standard spatio-temporal average $\overline{(\cdot)} = \frac{1}{L_x L_y T}\int_0^T \int_0^{L_x} \int_0^{L_y} (\cdot)\,\mathrm{d}y\,\mathrm{d}x\,\mathrm{d}t$, whilst the second type is a temporal-only average $\langle\cdot\rangle = \frac{1}{T}\int_0^T (\cdot)\,\mathrm{d}t$, where L_x, L_y are the lengths in the streamwise and spanwise directions respectively

and T is the averaging period. The temporal-average operator will be used for the spectral analysis. The two averaging operators naturally lead to two distinct definitions of fluctuations

$$A' = A - \overline{A}, \qquad A'' = A - \langle A \rangle. \tag{2.6}$$

We note that $A' = A''$ for a long time average. In this simulation the Prandtl number $Pr = \nu/\kappa = 1$ and the shear Reynolds number $Re_\tau = u_\tau h/(2\nu) = 263$, where Re_τ is based on the half channel height $h/2$, kinematic viscosity ν and the friction velocity $u_\tau = \sqrt{\tau_w/\rho}$. Here, τ_w and ρ are the wall shear stress and fluid density, respectively. Plus units are used to non-dimensionalise the data according to $u^+ = u/u_\tau$ and $\theta^+ = (\overline{\theta}_w - \theta)/\theta_\tau$, where $\theta_\tau = -\kappa \partial\overline{\theta}/\partial z\big|_w / u_\tau = q_w/u_\tau$ is the reference wall temperature and the subscript w represents measurements at the bottom wall ($z = 0$). To obtain time in plus units we non-dimensionalise time according to $t^+ = 2tu_\tau/h$. To acquire the turbulent statistics, the simulation is carried out until it reaches a statistically steady steady state at time $t^+ = 420$ and then averages are computed over a time period of 21 plus units.

2.3 Turbulence statistics

Figure 2.2(a) shows the (spatio-temporal) mean streamwise velocity. The mean velocity profile is in good agreement with the DNS of [Pirozzoli et al., 2014] at $Re_\tau = 260$. The mean velocity can be fitted to the log-law $\overline{u}^+ = (1/k)\log(Ez^+)$ with coefficients $k = 0.41$ and $E = 8.34$. The root mean square (RMS) of the three velocity components and the (spatio-temporal) mean of stress as a function of the wall normal coordinate are presented in figure 2.2(c,e). The velocity statistics are in good agreement with those from [Pirozzoli et al., 2014].

Plotted in figure 2.2(b,d,e) are the (spatio-temporal) mean temperature, the RMS of temperature and the (spatio-temporal) mean of the total temperature flux alongside its components, namely the diffusive and the turbulent temperature flux, respectively. Due to a scarcity of plane Couette simulations with a passive scalar, we also include channel flow simulations in the

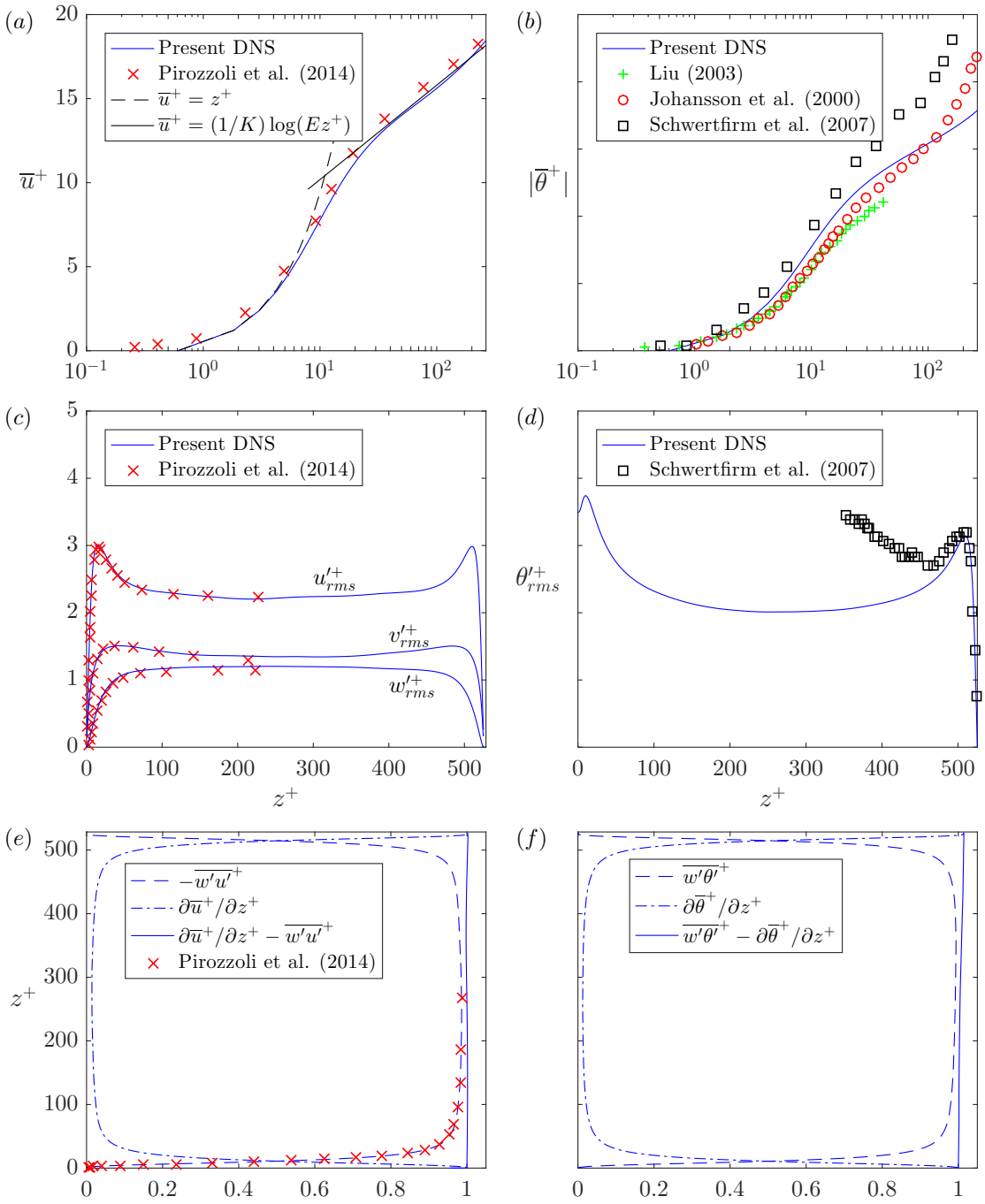

Figure 2.2: DNS results (a) the mean velocity; (b) the mean temperature; (c) RMS profiles of u, v, w-components of the velocity; (d) RMS profiles of θ; (e) stress profiles and (f) temperature flux profiles. In figures (a,c,e), comparisons with published results from [Pirozzoli et al., 2014] at $Re_\tau = 260$, in figure (b) comparisons with the result from [Liu, 2003] at $Re_\tau = 52.8$, [Johansson and Wikström, 2000] at $Re_\tau = 265$ and [Schwertfirm and Manhart, 2007] at $Re_\tau = 180$, and in figure (d) comparisons with the result from [Schwertfirm and Manhart, 2007] at $Re_\tau = 180$ have been shown, respectively. In figures (a-d), horizontal axis represents z^+ and in figures (e-f) z^+ is along vertical axis.

comparison. These have very similar inner layer properties, but the outer layer behaviour is different. The mean temperature is compared with data from [Liu, 2003] at $Re_\tau = 52.8$, [Schwertfirm and Manhart, 2007] at $Re_\tau = 180$ (channel flow) and [Johansson and Wikström, 2000] at $Re_\tau = 265$ (channel flow), and a reasonably good agreement is found for all three cases. In figure 2.2(d), the RMS temperature at the bottom wall is non-zero due to the applied temperature flux and the maximum RMS temperature is found at $z^+ = 10.34$. A comparison with [Schwertfirm and Manhart, 2007] at $Re_\tau = 180$ (channel flow) is also shown in figure 2.2(d) and good agreement is found at the near-wall (top wall) region. We chose the top wall for comparison to match with the fixed temperature boundary condition of the reference [Schwertfirm and Manhart, 2007].

The temperature flux profiles in figure 2.2(f) are similar to the shear stress profiles. Along the channel height, the total temperature flux matches the theoretical constant value closely, with a relative error in the ℓ^2-norm that is less than 1%.

2.4 Conclusions

A data-set for flow reconstruction was created using Direct Numerical Simulation of plane Couette flow with imposed heat flux condition on the bottom wall. Due to the prescription of a fixed temperature flux, the temperature on the bottom wall is free and temperature patterns can develop on the wall. DNS wall patterns will be used as a proxy for flow reconstructions in upcoming chapters. in the simulation, Richardson number Ri is assumed zero in limiting sense. That is, the role of gravity is not considered in the simulation.

We computed turbulence statistics of the flow and compared them with published results. The mean velocity and the mean temperature follow a log-law. The root mean squares, stress and heat flux statistics are found to be in good agreement with previously published results. The RMS temperature at the bottom wall is non-zero due to the applied temperature flux and the maximum RMS temperature is found at $z^+ = 10.34$.

Chapter 3

Estimating wall shear stress from thermal wall patterns

In this chapter[1], we reconstruct the wall shear stress of plane Couette flow from thermal wall imprints generated by direct numerical simulation at $Re_\tau = 263$ discussed in chapter 2, using an imposed surface temperature flux and fixed temperature at the bottom and top boundary, respectively. We explore the strong correlation between wall shear stress and wall temperature by analysing their joint probability density function and cross variance spectrum, before developing a spectral model based on linear regression. We then use observed symmetries in the estimator parameters to reduce the degrees of freedom of the model. The reconstructed wall shear stress reproduces streamwise streaky structures. The relative error in the ℓ^2-norm of 0.25 is primarily associated with the absence of local maxima in the reconstructed wall shear stress.

3.1 Introduction

The wall shear stress is an important quantity in fluid dynamics that plays a leading role in many industrial applications, such as in aviation and the shipping industry [Douvi et al., 2015]. The wall shear stress can be directly linked to fuel consumption and energy efficiency; hence

[1]Chapter 2 and 3 are under review with the International Journal of Heat and Fluid Flow.

measurements of the wall shear stress have attracted attention for many decades [Douvi et al., 2015, Mayer, 1998, Haff et al., 2018]. A thorough review of the early attempts to measure the wall shear stress can be found in [Haritonidis, 1989]. Measurement techniques in this regard can be divided into two categories: indirect and direct methods. Indirect methods rely on established correlations between a flow and its wall shear stress. For example, the Preston tube technique relies on the law of the wall to measure the wall shear stress [Winter, 1977]. Other possible correlations are the pressure gradient in channel flow [Örlü and Vinuesa, 2020] and the momentum thickness over a flat plate [Haritonidis, 1989].

In contrast, direct methods sense a force acting on a surface. Examples include the flush-mounted floating element [Naughton and Sheplak, 2002] and the micro-electro-mechanical system (MEMS) based sensors [Ho and Tai, 1998, Löfdahl and Gad-el Hak, 1999]. The small physical size of the MEMS sensors makes them suitable for a vast number of applications requiring relatively high spatial and temporal resolutions. With the advance of physics in the field of thermal [Leu et al., 2016, Liepmann and Skinner, 1954] and laser [Naqwi, 1993] sensors, the uses of MEMS sensors are increasing.

Both direct and indirect techniques have their shortcomings, including disturbance due to sensor probing and a lack of capability to measure the spatial distribution of the wall shear stress, which limits their viability in industrial applications. To overcome these limitations, flow visualisation techniques have been developed. The thin oil film technique [Maltby R. L., 1962, Tanner and Blows, 1976, Tanner, 1977] based on the thin-oil-film equations derived by Squire [Maltby R. L., 1962] and the liquid crystal coating [Reda and Muratore, 1994, Zhao, 2018] are two such techniques.

In the non-intrusive TIV [Hetsroni et al., 2001, Kowalewski et al., 2003, Inagaki et al., 2013] thermal images at a wall are tracked to find the velocity of the thermal structures. Whilst the aim of TIV is not directly to reproduce the wall shear stress, it is clear that high velocities inferred with TIV are likely to correlate with high wall shear stresses. The aim of this chapter is to investigate to what extent the spatial distribution of the wall temperature can be used to estimate the instantaneous wall shear stress. We discussed direct numerical simulation of a

plane Couette flow with constant surface temperature flux in previous chapter 2 and generated a data-set of thermal wall imprints. These are then correlated with the wall shear stress, and a spectral model is developed to link the two.

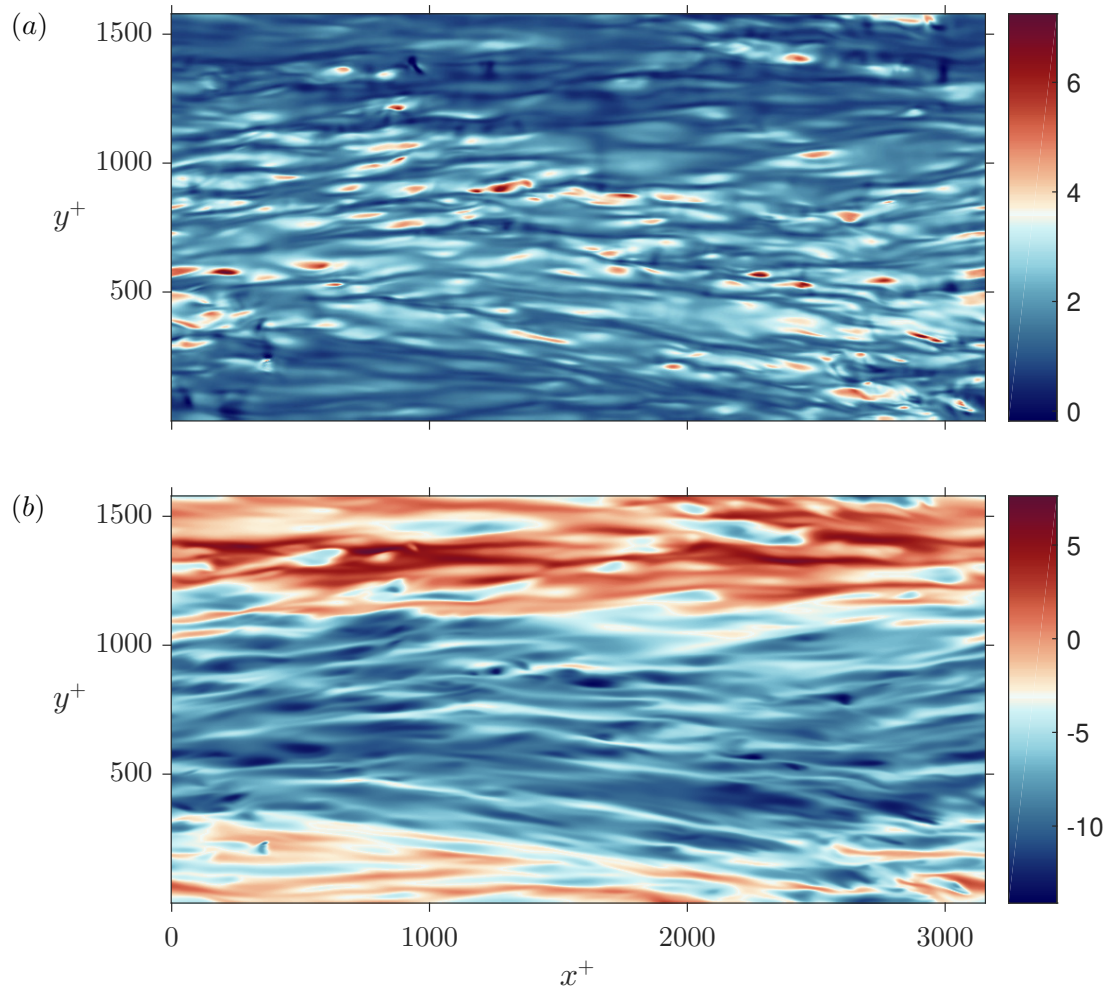

Figure 3.1: Snapshots acquired from the DNS, (a) wall shear stress and (b) wall temperature. The contour plots show the color from the minimum (blue) to the maximum (red) (a) $\tau_w^+ = -0.18$ to $\tau_w^+ = 7.25$ and (b) $\theta_w^+ = -14.11$ to $\theta_w^+ = 7.62$.

3.2 Joint PDF and spectral analysis

The aim of this section is to establish the link between the wall temperature θ_w and the wall shear stress τ_w. We start by presenting a pair of snapshots of the θ_w and τ_w in figure 3.1, obtained from the DNS at the same time step. Visual inspection of the figure 3.1 suggests

similarities between the two fields. Both fields contain large streamwise streaky structures, which are the signature of a wall bounded shear flow [Waleffe, 1997, Hetsroni et al., 2001].

The snapshots show that the wall shear stress is low when the temperature is high and vice versa, suggesting that these two physical quantities are negatively correlated [Wallace et al., 2006]. Indeed, the correlation coefficient

$$R_{\theta_w \tau_w} = \frac{\overline{\theta'_w \tau'_w}}{\sqrt{\overline{\theta'^2_w}}\sqrt{\overline{\tau'^2_w}}} \tag{3.1}$$

between θ_w and τ_w is equal to -0.69. The faster (relative to the mean velocity) patches of the fluid cool down (relative to the mean wall temperature) the corresponding sections of the wall, whereas the slower patches give rise to the higher temperature regions. This is because sweeps, which cause high shear stress, bring low-temperature fluid to the wall.

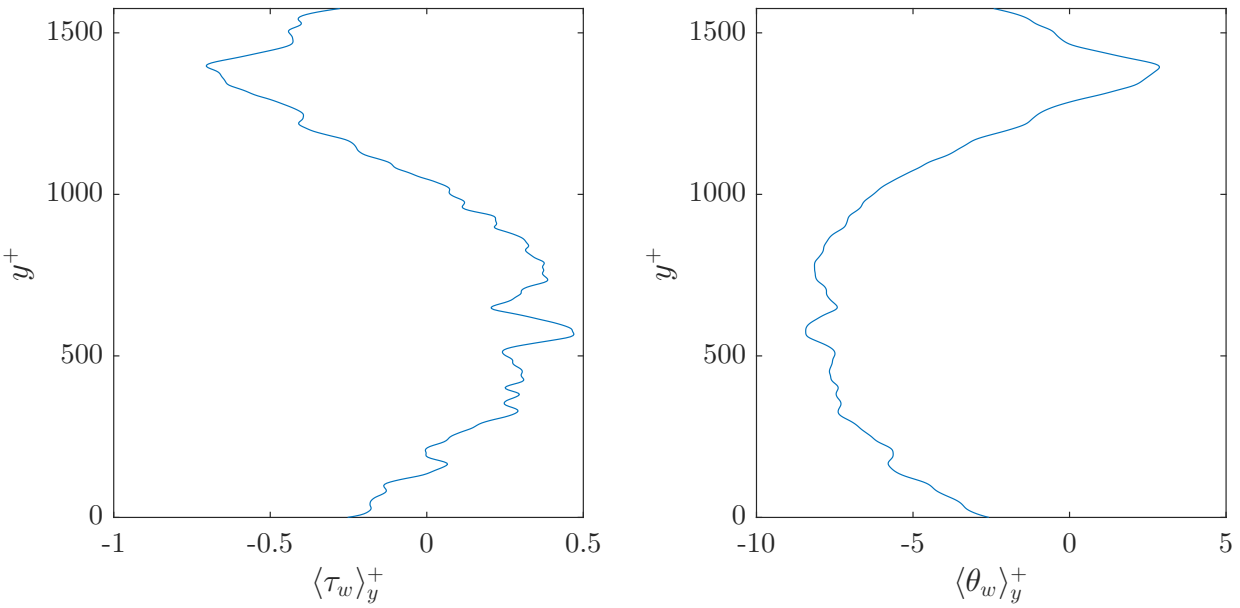

(a) (b)

Figure 3.2: (a) $\langle \tau_w \rangle_y^+$ and (b) $\langle \theta_w \rangle_y^+$ against y^+, respectively.

The figure 3.2(a,b) show $\langle \tau_w \rangle_y^+$ and $\langle \theta_w \rangle_y^+$, respectively against y^+. The averaging operator $\langle \cdot \rangle_y$ is defined as below

$$\langle \cdot \rangle_y = \int_0^{L_x} (\cdot) \quad dx$$

It is evident that from the figures 3.2(a,b) that wall shear stress τ_w and θ_w are strongly (negatively) correlated. In both figures, a large mean structure with streak size about 1100 plus-units is visible.

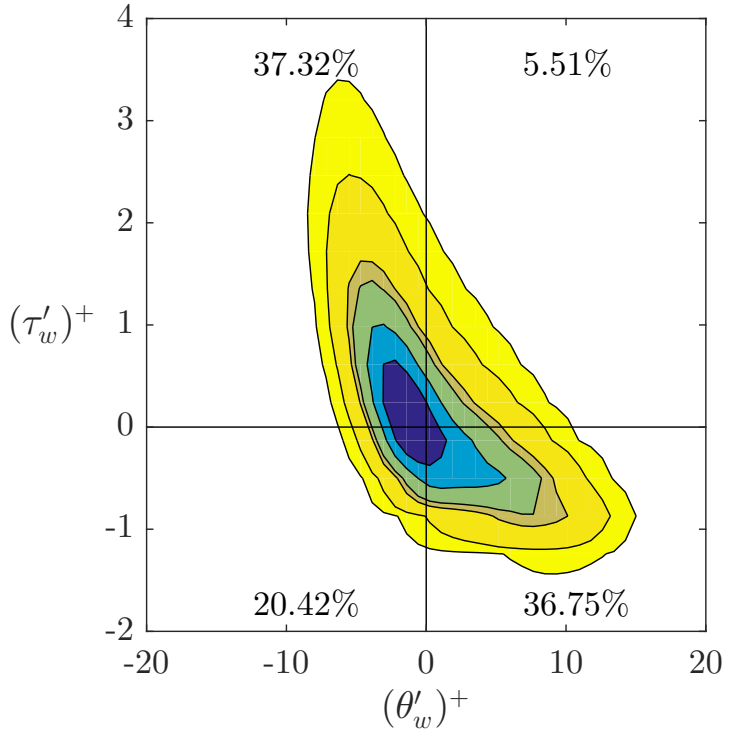

Figure 3.3: Joint PDF of wall shear stress fluctuation and thermal wall pattern fluctuation. The contour labels represent the probability of data points inside the contours. From inside (dark blue) to outside (yellow) the contours represent 25%, 50%, 70%, 80%, 95% and 99% data respectively. The percentage in each quadrant is the percentage of data points within the quadrant.

The joint probability density function of the wall temperature θ_w and the wall shear stress τ_w is presented in figure 3.3. The contours represent the probability of data pairs inside the contours. The data pairs are concentrated in the second and the fourth quadrants (which collectively contain 74% of the data pairs) and suggest a strong negative correlation between the wall temperature θ_w and the wall shear stress τ_w. In addition, the contribution of the second and fourth quadrants are almost the same. The next largest contribution corresponds to the third quadrant, which corresponds to low stress and the transport of low temperature fluid to the wall. Another important observation is that the joint PDF is not symmetric about the $(\theta'_w)^+ = 0$ line. This asymmetry clearly differentiates the relationships between θ_w and τ_w for high and low temperature regions.

In the remainder of this section we discuss the relationship between θ_w and τ_w in Fourier space. The 2D Fourier transform of χ in x, y is denoted by $\hat{\chi}(k_x, k_y, z, t)$, where χ is an arbitrary quantity and $k_x = 2\pi n_x / L_x$ and $k_y = 2\pi n_y / L_y$ are the wavenumbers in the streamwise and the spanwise directions. The wavelengths in the streamwise and spanwise directions are defined as $\lambda_x = 2\pi/k_x$ and $\lambda_y = 2\pi/k_y$, respectively. The relation between the spatio-temporal fluctuation and those in Fourier space (based on a temporal mean $< \cdot >$) are provided using the Plancherel theorem (see appendix A for derivation) [Wiener, 2010]

$$\overline{\tau_w'^2} = \sum_{n_x}\sum_{n_y}\langle \hat{\tau}_w''^* \hat{\tau}_w'' \rangle, \qquad \overline{\theta_w' \tau_w'} = \sum_{n_x}\sum_{n_y}\langle \hat{\theta}_w''^* \hat{\tau}_w'' \rangle, \qquad \overline{\theta_w'^2} = \sum_{n_x}\sum_{n_y}\langle \hat{\theta}_w''^* \hat{\theta}_w'' \rangle \tag{3.2a-c}$$

The left side of equation 3.2(b) is the total cross covariance of the wall shear stress and the wall temperature, and the quantities $\langle \hat{\theta}_w''^* \hat{\tau}_w'' \rangle$ on the right side are the cross-variances in the wavenumber space. That is, the cross-spectrum $\langle \hat{\theta}_w''^* \hat{\tau}_w'' \rangle$ shows how the total covariance $\overline{\theta_w' \tau_w'}$ is distributed over different wavenumber pairs (k_x, k_y). The same principle holds for $\overline{\tau_w'^2}$ and $\overline{\theta'^2}$, using the equations 3.2(a) and 3.2(c), respectively.

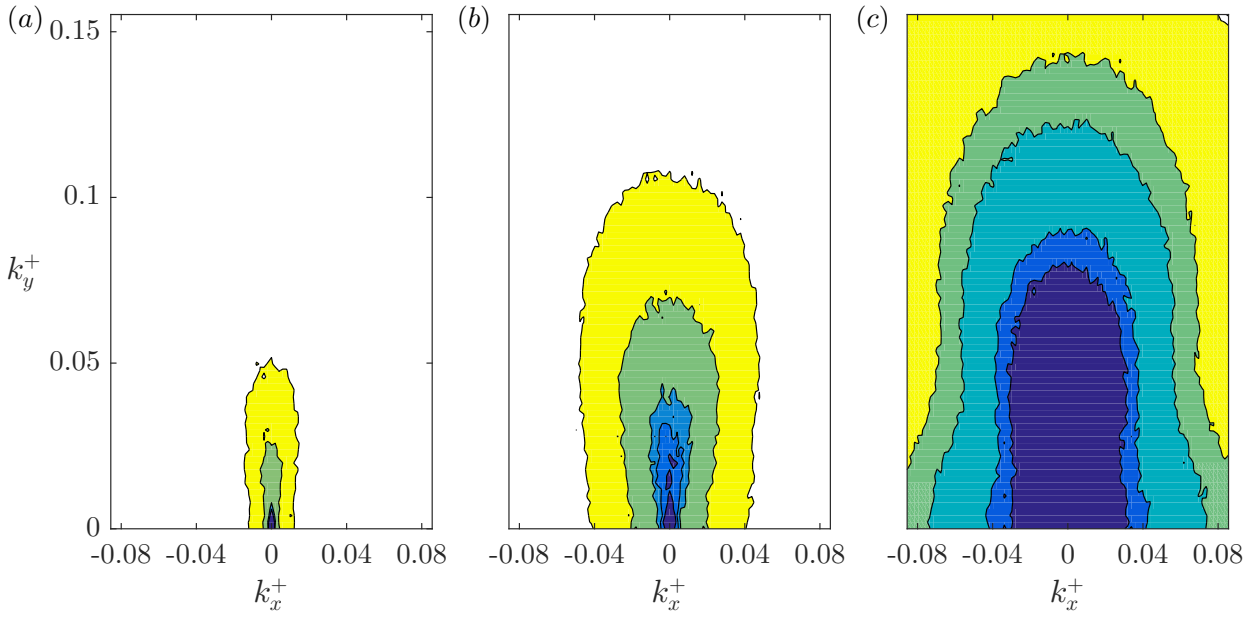

Figure 3.4: (a) spectrum of the wall temperature $\overline{\hat{\theta}'^* \hat{\theta}'}$; (b) The modulus of shear stress and wall temperature cross-spectrum $\overline{\hat{\theta}'^* \hat{\tau}'}$; (c) spectrum of the wall shear stress $\overline{\hat{\tau}'^* \hat{\tau}'}$. The contours represent the percentage of the variance captured by the wavenumber pairs within the contours. From the inner-most contour (dark blue) to the out-most contour (yellow) the percentages are 57%, 70%, 80%, 95% and 99% respectively.

Figure 3.4 shows the modulus of the cross-spectrum along with the individual spectrum of the wall shear stress and the thermal wall patterns. The contours show the percentages of variance/covariance captured by the wavenumber pairs within the contours. As can be seen from figure 3.4, the wavenumber pairs around the $k_x^+ = 0$ line are the most energetic pairs for both wall quantities $\hat{\tau}_w''$ and $\hat{\theta}_w''$. Compared to the wall shear stress spectrum, the temperature spectrum is more dominated by the first few low wavenumbers pairs. The energetically dominant pairs around $k_x^+ = 0$ are responsible for the coherent streamwise streaky structures which are long in the streamwise direction and short in the spanwise direction.

3.3 Inferring τ_w from θ_w

In order to use the wall temperature to estimate the wall shear stress, a spectral model will be developed that relies on a linear least-squares estimator. The linear least squares estimator assumes that, for each wavenumber pair (k_x, k_y), the input $\hat{\theta}_w''(k_x, k_y, t)$ and the output $\hat{\tau}_w''(k_x, k_y, t)$ are related linearly as

$$\hat{\tau}_w''(k_x, k_y, t) = C(k_x, k_y)\hat{\theta}_w''(k_x, k_y, t) \tag{3.3}$$

where $C(k_x, k_y)$ is an unknown time-independent estimator parameter. To obtain C, we minimise $\left\langle \hat{\tau}_w'' - C(k_x, k_y)\hat{\theta}_w'' \right\rangle^2$ with respect to C. For minimisation,

$$\begin{aligned}
0 =& \frac{d}{dC}\left\langle \hat{\tau}_w(k_x, k_y)'' - C(k_x, k_y)\hat{\theta}_w(k_x, k_y)'' \right\rangle^2 \\
&= 2\left\langle \hat{\theta}_w(k_x, k_y)''^* \left(\hat{\tau}_w(k_x, k_y)'' - C(k_x, k_y)\hat{\theta}_w(k_x, k_y)'' \right) \right\rangle \\
&= 2\left\langle \hat{\theta}_w(k_x, k_y)''^* \hat{\tau}_w(k_x, k_y)'' - C(k_x, k_y)\hat{\theta}_w(k_x, k_y)''^* \hat{\theta}_w(k_x, k_y)'' \right\rangle \\
&= 2\left\langle \hat{\theta}_w(k_x, k_y)''^* \hat{\tau}_w(k_x, k_y)'' \right\rangle - 2C(k_x, k_y)\left\langle \hat{\theta}_w(k_x, k_y)''^* \hat{\theta}_w(k_x, k_y)'' \right\rangle
\end{aligned}$$

By rearranging, the estimator parameter $C(k_x, k_y)$ for each k_x and k_y pair is then given by

$$C(k_x, k_y) = \frac{\langle \hat{\theta}_w(k_x, k_y)''^* \hat{\tau}_w(k_x, k_y)'' \rangle}{\langle \hat{\theta}_w(k_x, k_y)''^* \hat{\theta}_w(k_x, k_y)'' \rangle} \tag{3.4}$$

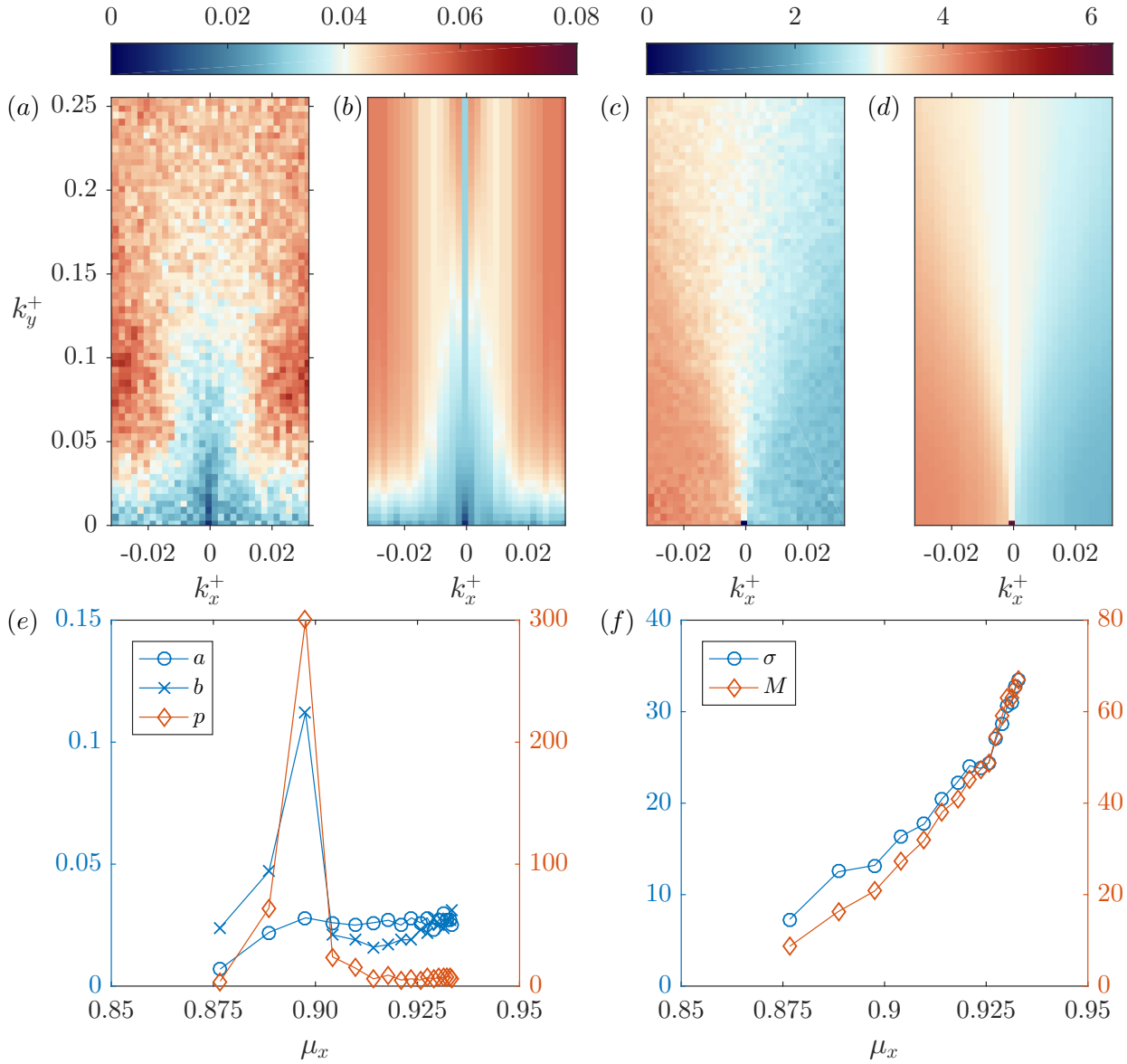

Figure 3.5: (a) $|C|$, obtained from the DNS; (b) The exponential fit c; (c) $\arg C$, obtained from the DNS; (d) The Gaussian fit φ; The exponential fit parameters (e) a, b and p, and the Gaussian fit parameters (f) σ and M. The figures (a-d) are shown in the $k_x^+ k_y^+$ plane. The horizontal coordinate μ_x in figures (e,f) is defined as equation 3.9.

To determine C, we use half the data set (230 snapshots). The other half is used to test the performance of the model. In Fourier space, we consider the interval $|k_x^+| \leq 0.03$ and $|k_y^+| \leq 0.26$. This choice is motivated from the cross spectrum of τ_w and θ_w in figure 3.4(b), where

more than 95% of the total cross variances is associated with the chosen wavenumber pairs. Therefore, $33 \times 129 = 4257$ wavenumber pairs are considered in total. However, the symmetries of the Fourier transform imply that $\hat{\chi}(k_x, k_y) = \hat{\chi}^*(-k_x, -k_y)$ and $\hat{\chi}(k_x, -k_y) = \hat{\chi}^*(-k_x, k_y)$ for all k_x, k_y. The combination of these with the fact that the wall shear stress is real-valued in physical space, leaves only $17 \times 65 = 1105$ pairs.

In order to determine C, we acquired the wall temperature and wall shear stress at a temporal resolution of $\Delta t^+ = 0.0021$, which corresponds to approximately 10 DNS time steps. We consider 460 consecutive snapshots; within this time period, the top wall moves approximately three channel lengths ($2TU = 3.067L_x$) in the streamwise direction. The choice of the temporal resolution can be explained via Taylor's hypothesis which implies that a structure with streamwise wavenumber k_x at a wall-normal height z gives rise to a temporal frequency $\omega = k_x U(z)$ as it convects downstream Illingworth2018. For our choice of the largest streamwise wavenumber $k_x^+ = 0.03$ and the largest mean velocity (at the top wall), the maximum temporal frequency is $\omega^+ = 0.606$. That is, to resolve the maximum frequency at the largest k_x^+, the required temporal resolution is 0.0063 in plus-unit (3 times larger than $\Delta t^+ = 0.0021$). Since, Δt^+ is chosen much smaller than the required minimum temporal resolution for the largest wavenumber considered, our choice of Δt^+ is justified.

Plotted in figure 3.5(a, c) are the modulus and phase of C, which linearly correlates the wall temperature mode $\hat{\theta}_w$ to the wall shear stress mode $\hat{\tau}_w$ for each (k_x^+, k_y^+). Visual inspection of the modulus of C suggests that modes $k_x^+ = 0$ of $\hat{\theta}_w$ and $\hat{\tau}_w$ are strongly negatively correlated, whereas the higher wavenumber modes ($k_x^+ \geq 0.01$) are positively correlated for $k_y^+ \geq 0.02$. The phase of C, as shown in figure 3.5(c), converges to π for all k_x^+. For higher wavenumbers k_x^+, the phase of C converges to π at higher k_y^+.

In order to be able to predict wall shear stress from the wall temperature, it is convenient to parameterise C by considering its modulus $c(k_x, k_y)$ and phase $\varphi(k_x, k_y)$ independently as $C = c\exp(i\varphi)$. The data suggest a reasonably good model can be obtained by using the

approximation:

$$c(k_x, k_y) = a(k_x) + b(k_x)\left(1 - \exp\left(-|k_y|/p(k_x)\right)\right) \tag{3.5}$$

$$\varphi(k_x, k_y) = \pi - \frac{M(k_x)}{\sqrt{2\pi\sigma^2(k_x)}} \exp\left(-\frac{1}{2}\frac{k_y^2}{\sigma^2(k_x)}\right) \tag{3.6}$$

where a, b and p are the parameters of the exponential fit for c and M, σ are the parameters for φ. All of the 5 parameters are functions of the streamwise wavenumber k_x only. Thus, this approximation of C significantly reduces the degrees of freedom of the estimation from $17 \times 65 = 1105$ (17 and 65 are the numbers of the streamwise and spanwise wavenumbers considered, respectively) to $17 \times 5 = 85$.

To be able to fit the parameters for each k_x in the approximations (3.5)-(3.6) we minimise $\|c - |C|\|_w$ and $\|\varphi - \arg C\|_w$ with respect to $\{a, b, p\}$ and $\{M, \sigma\}$, respectively, where, $\left|C\right|$ and $\arg C$ are obtained from the DNS and the norm $\|\cdot\|_w$ is a weighted ℓ^2-norm, defined for any arbitrary χ as

$$\| \hat{\chi} \|_w (k_x) = \sqrt{\sum_{n_y=0}^{N_y} \hat{\chi}\left(k_x, \frac{2\pi n_y}{L_y}\right) w\left(k_x, \frac{2\pi n_y}{L_y}\right)} \tag{3.7}$$

where

$$w(k_x, k_y) = \frac{\hat{\tau}_w^*(k_x, k_y)\,\hat{\tau}_w(k_x, k_y)}{\sum_{n_x=0}^{N_x}\sum_{n_y=0}^{N_y} \hat{\tau}_w^*\left(\frac{2\pi n_x}{L_x}, \frac{2\pi n_y}{L_y}\right)\hat{\tau}_w\left(\frac{2\pi n_x}{L_x}, \frac{2\pi n_y}{L_y}\right)} \tag{3.8}$$

Here, N_x and N_y are the number of modes in the streamwise and spanwise directions, respectively. This norm is designed to give the most energetic modes more weight in the minimisation, and is similar to the norm described in [Colonius et al., 2002] based on stagnation enthalpy for compressible flow that accounts for the three components of the velocity, the speed of sound and pressure.

Plotted in figure 3.5(b,d) are the fitted c and φ. Comparison with figure 3.5(a,c) suggests that the approximations (3.5)-(3.6) are in good agreement with the DNS. In figure 3.5(e,f) the five parameters a, b, p, M and σ are shown. The horizontal axis represents the cumulative energy

fraction μ_x, where μ_x is defined for $m = 0, 1, 2, \ldots, N_x$ as

$$\mu_x(m) = \sum_{n_x=0}^{m} \sum_{n_y=0}^{N_y} w\left(\frac{2\pi n_x}{L_x}, \frac{2\pi n_y}{L_y}\right) = \sum_{n_x=0}^{m} \sum_{n_y=0}^{N_y} \hat{\tau}_w^* \hat{\tau}_w \Bigg/ \sum_{n_x=0}^{N_x} \sum_{n_y=0}^{N_y} \hat{\tau}_w^* \hat{\tau}_w \tag{3.9}$$

Note that μ_x does not depend on the spanwise wavenumbers due to the full summation over N_y modes.

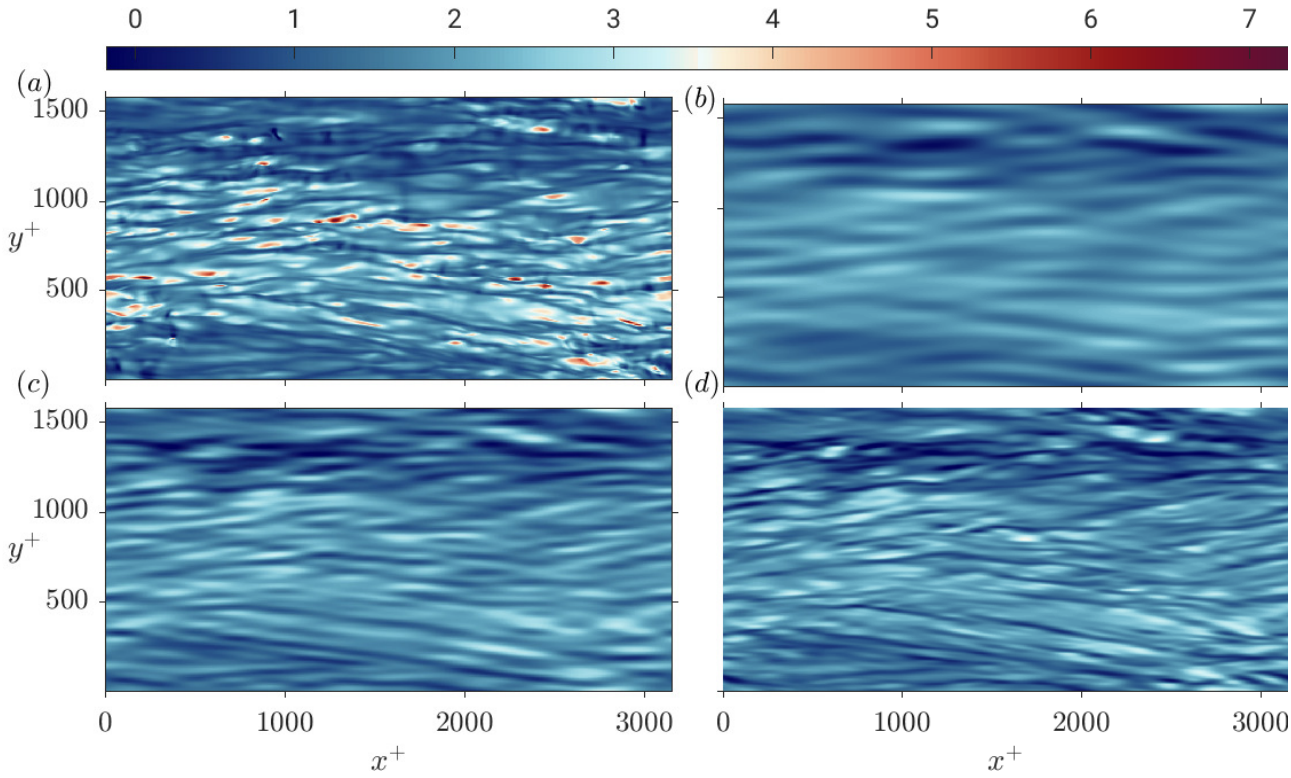

Figure 3.6: (a) Instantaneous wall shear stress from the DNS; estimated wall shear stress using (b) 9×33, (c) 17×65 and (d) 33×129 wavenumber pairs. The contour plots show the color from the minimum $\tau_w^+ = -0.18$ (blue) to the maximum $\tau_w^+ = 7.25$ (red).

As shown in figure 3.5(e), the parameters b and p for the first three smallest μ_x, seem to act differently from the rest. The first three modes, including the mean mode, constitute approximately 90% of the total variance and are therefore very important for the estimation. The decay rate p for the third mode is found to be high and equal to the maximum limit set to solve the minimisation problem (3.5) numerically. For large values of μ_x the parameters show a consistent behaviour. For example, the almost identical decay rate p indicates a similar asymptotic behaviour for the higher streamwise wavenumbers. Figure 3.5(f) shows the parameters σ and M are increasing with μ_x. Specifically, as μ_x increases, the phase of C converges to π at a

higher k_y.

The model (3.5)-(3.6) with the calibrated coefficients shown in figure 3.5(e,f) will now be used to estimate the wall shear stress from the wall temperature for a snapshot that was not used in the calibration of the coefficients and therefore provides a more stringent test. The shear stress is shown in figure 3.6(a), and the estimations are shown in figures 3.6(b-d) with number of modes 9×33 (b), 17×65 (c) and 33×129 (d). The spanwise wavelengths considered in figures 3.6(b-d) are $\lambda_y^+ \geq 98.44$, $\lambda_y^+ \geq 49.22$ and $\lambda_y^+ \geq 24.61$, respectively, whereas the mean streak width is obtained from the DNS as 94.79, in plus units. Since the minimum spanwise wavelength considered in figure 3.6(b) is close to the mean streak width, some of the streaky structures have started to appear. In figure 3.6(c), the minimum spanwise wavelength is almost the half of the mean streak width found in the DNS and most of the streaky structures are visible. In figure 3.6(d), where $\lambda^+ \geq 24.61$, the streaky structures become more prominent. Visual inspection reveals that figure 3.6(d) is a good reconstruction of the wall shear stress in figure 3.6(a), which is to be expected, since from the cross spectrum in figure 3.4(b), 33×129 wavenumber pairs are associated with more than 95% of the total cross variances. The reconstructed wall shear stress is unable to reproduce the local maxima (colored red), due to the truncation in wavenumber space. The relative errors of the estimate in figure 3.6(b-d) in ℓ^2-norm are 0.36, 0.28 and 0.25, respectively.

3.4 Conclusions

We used the wall temperature patterns as a proxy for the wall shear stress. Indeed, the wall shear stress and the wall temperature are strongly correlated and both possess the signature of coherent streamwise streaky structures.

In order to reconstruct the shear stress, we analysed the wall temperature in Fourier space and developed a simple spectral linear regression model between τ_w and θ_w. The first three streamwise wavenumbers were found to constitute about 90% of the total variance and the higher wavenumbers showed a asymptotic behaviour in the weighted (energy) wavenumber space. In

addition, the phase of C was found to deviate increasingly from π at higher wavenumbers.

The complex correlation coefficient C was successfully parameterised by its modulus and phase independently, reducing the degrees of freedom of the estimation substantially (from 1105 modes to 85 modes, 13 times reduced). The spectral model reproduces the wall shear stress well (the relative ℓ^2-norm error was 0.25), except for the local maxima due to the truncation of the number of modes.

The idea of using the wall temperature was motivated by the need for measurement techniques that are capable of estimating distributed wall shear stress in a non-intrusive manner with low set-up cost. Use of wall temperature patterns meet both of these requirements and can estimate wall shear stress of plane Couette flow well, with the exception of local stress maxima. The spectral model discussed here could in theory be readily applied to the estimation of wall shear stress in other flows, such as Rayleigh-Bénard convection [Ahlers et al., 2009, Grossmann and Lohse, 2000, van Reeuwijk et al., 2008]. Further work should also incorporate appropriate modifications for non-homogeneous surfaces such as flows with obstacles. For non-homogeneous surfaces, Fourier modes are no longer applicable and would need to be replaced with other decompositions such as the proper orthogonal decomposition [Lumley, 1967, Holmes et al., 2012].

Chapter 4

Estimating flow from thermal wall patterns using the POD method

In this chapter, we aim to evaluate and use proper orthogonal decomposition (POD) modes to reconstruct streamwise velocity of plane Couette flow using wall temperature. To achieve the aim, we carefully design two sets of test cases/problems with increasing complexity. The first set of problems are designed to evaluate and test the performance of the POD modes. In the first problem of this set, we first evaluate POD modes of $1D$ Kuramoto-Sivashinsky (KS) chaotic dynamics. The second problem consists of evaluation and testing of the POD modes for the plane Couette flow at $Re_\tau = 263$ discussed in chapter 2. The second set of problems are designed to test the performance of POD modes to reconstruct a gappy field. A gappy field is where some of the information is missing. Once again, we first test with the simpler KS dynamics and followed by plane Couette flow data-set. Finally, we proceed to the key aim — reconstruct the flow velocity using wall temperature only, which represents a large amount of 'gappiness' and therefore a limiting case of the second set of problems.

4.1 Proper orthogonal decomposition

The proper orthogonal decomposition (POD) of an ensemble is a statistical technique that provides an orthonormal set of modes. The special property of POD modes is the optimal ability to capture a physically important quantity, such as the kinetic or the thermal energy of an ensemble. For example, if the POD technique is applied on the velocity ensemble of a fluid flow, the first k POD modes captures more kinetic energy of the flow compared to any k modes obtained from any other modal decomposition. The POD was first introduced in turbulence by John L. Lumley [Lumley, 1967] and is also known as Karhunen-Loéve decomposition and Principal Component Analysis (PCA).

The POD is widely used in the field of random variables, image processing, signal analysis, data compression, oceanography, process identification and control in chemical engineering [Gal Berkooz et al., 1993]. A good review of POD can be found in [Holmes et al., 2012] and [Gal Berkooz et al., 1993]. After Lumley, POD was explored by Sirovich and others in a series of investigations [Sirovich, 1989], for channel flow [Deane and Sirovich, 1991, Sirovich and Deane, 1991] and for transitional jet flow [Sirovich et al., 1990]. But perhaps the two most important results were presented in [Sirovich, 1987] and [Everson and Sirovich, 1995]. In the first, Sirovich proposed an alternative computational approach to evaluate POD modes –the method of snapshots– which greatly reduced the computational cost. In the second work [Everson and Sirovich, 1995], POD modes were used to reconstruct human faces from 10% available pixels using gappy POD method. [Podvin et al., 2006] used this gappy POD method later for reconstructing a turbulent flow past an open cavity. They reconstructed $3D$ velocity fields using POD modes and $2D$ velocity on a wall-normal plane.

The core idea of any modal decomposition technique is to represent a field, such as a scalar field ϑ, as the linear superposition of a set of orthonormal spatial modes $\{\varphi_i\}$. An illustration of a flow decomposition is presented in the Figure 4.1. If a_i are the temporal coefficients, then

$$\vartheta(\mathbf{x}, t) = \sum_{i=1}^{\infty} a_i(t)\varphi_i(\mathbf{x}) \tag{4.1}$$

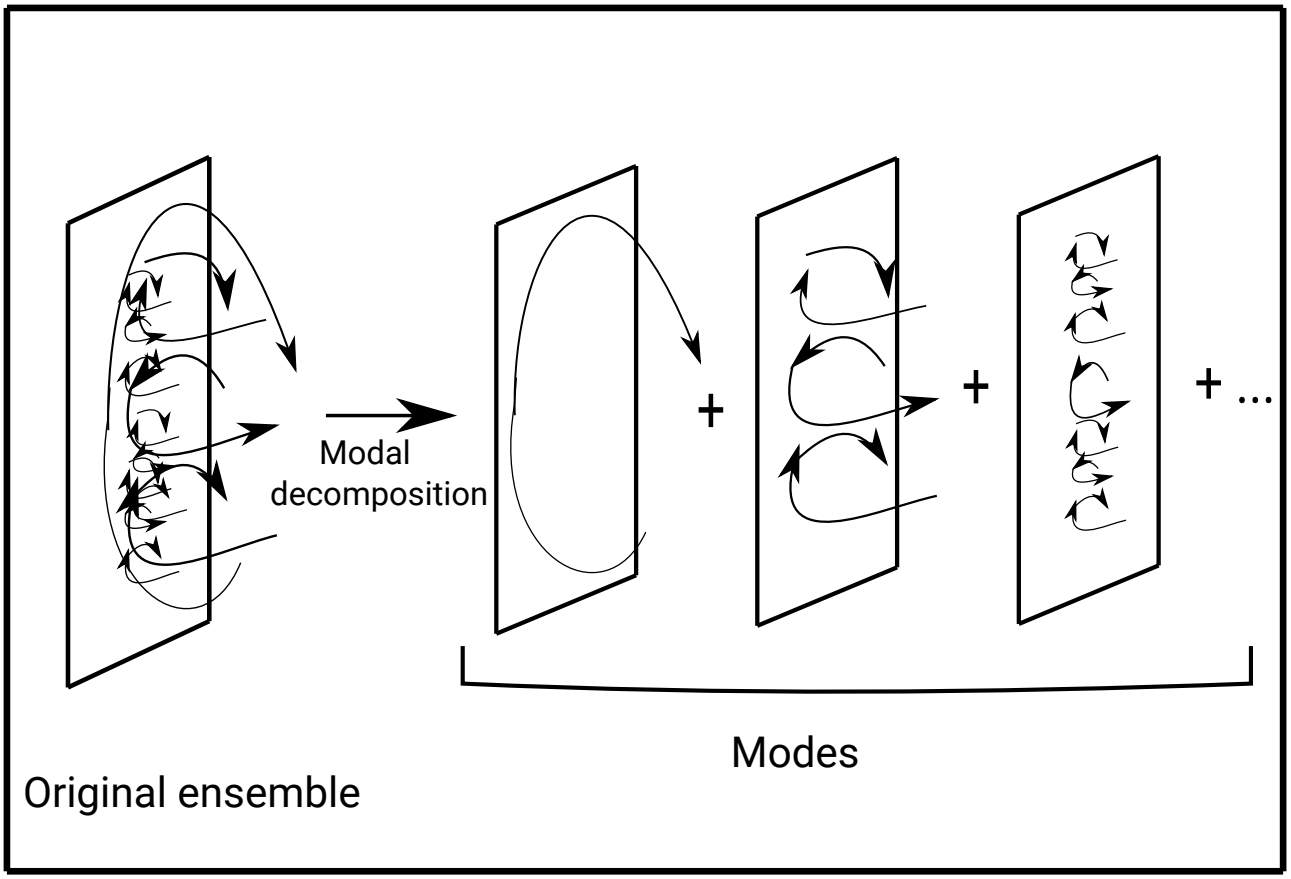

Figure 4.1: Schematic diagram describing a modal decomposition technique.

In practice, the scalar field ϑ is approximated by a finite number of modes. A finite-dimensional approximation θ of ϑ, using N modes can be expressed as

$$\theta(\mathbf{x},t) = \sum_{i=1}^{N} a_i(t)\varphi_i(\mathbf{x}) \tag{4.2}$$

The Fourier expansion is a good example of a modal decomposition techniques and arises over statistically homogeneous dimension of a flow (see section 4.2.2). The scalar field θ is assumed to belong to the Hilbert space $L^2(D)$, of square integrable functions, defined from the spatial domain D of the ensemble to the complex field $\mathbb{C}$. The validity of this assumption is trivial, since, for any physically realistic flow field, $\int_D \theta^2(\mathbf{x},t)\,d\mathbf{x}$ is finite. The inner product of the $L^2(D)$–space is defined as

$$(f,g) = \int_D f(\mathbf{x})g^*(\mathbf{x})\,d\mathbf{x} \tag{4.3}$$

where, $*$ stands for the complex conjugate and, f and g are some functions of $L^2(D)$. The

norm of the $L^2(D)$–space can be expressed as

$$\| f \| = (f, f)^{1/2} = \sqrt{\int_D f(\mathbf{x}) f^*(\mathbf{x})\, d\mathbf{x}} \tag{4.4}$$

Among the infinite number of functions in the $L^2(D)$–space, the POD technique searches for a function φ that minimises the averaged squared norm between the ensemble θ and its projection onto φ, i.e., the quantity $\left\langle \left\| \theta - (\theta, \varphi)\, \varphi / \|\varphi\|^2 \right\|^2 \right\rangle$ is minimised. The angle brackets denote time averaging over the ensemble time T as $\langle \theta \rangle = T^{-1} \int_0^T \theta\,(\mathbf{x}, t)\, dt$. The above minimisation problem is equivalent to maximising the averaged projection of θ onto φ, normalised by $\| \varphi \|^2$ [Holmes et al., 2012]; that is,

$$\max_{\varphi \in D} \frac{\langle | (\theta, \varphi) |^2 \rangle}{\| \varphi \|^2} \tag{4.5}$$

Solution of the (4.5) yields the best approximation for φ and the critical points of the functional in (4.5) form a set of functions which provides the desired basis. The maximisation problem (4.5) can be solved as a variational problem and shown to be equivalent to the eigenfunction problem [Holmes et al., 2012],

$$R\varphi = \lambda\varphi \tag{4.6}$$

where, R is a linear operator, defined as

$$R\varphi = \langle (\varphi, \theta)\, \theta \rangle\,. \tag{4.7}$$

Any mode φ_i of the equation 4.2 will be a POD mode, if the mode satisfies the eigenfunction problem (4.6). In other words, if the equation 4.6 is an N–dimensional eigenfunction problem then the eigenfunctions (solutions of the equation 4.6), $\varphi_1, \varphi_2, \varphi_3, \ldots, \varphi_N$ are the POD modes of the scalar field θ with corresponding eigenvalues $\lambda_1, \lambda_2, \lambda_3 \ldots, \lambda_N$.

The eigenvalue problem (4.6) can be extended for any multi-component state variable. For example, a state variable $\mathbf{s}$ can be defined as $\mathbf{s} = (u, v, w, \theta)$, where $\mathbf{u} = (u, v, w)^T$ are velocity components and so, $\mathbf{s}$ is a vector-valued function. The state vector $\mathbf{s}$ is assumed to belong to

the space D and the inner product is defined for any $\mathbf{f}, \mathbf{g} \in D$ [Holmes et al., 2012] as

$$(\mathbf{f}, \mathbf{g}) = \int_D (\mathbf{g}^*(\mathbf{x}))^T Q(\mathbf{x}) \mathbf{f}(\mathbf{x})\, d\mathbf{x} \tag{4.8}$$

where, $Q \in \mathbb{C}^{4\times4}$ is a positive-definite Hermitian matrix. In general, Q is assumed to be the identity matrix $\mathbf{I}$, in which case the eigenvalue problem (4.6) becomes

$$R\boldsymbol{\varphi}(\mathbf{x}) = \int_D \left\langle \mathbf{s}(\mathbf{x}, t)\mathbf{s}^*(\mathbf{x}', t)^T \right\rangle \boldsymbol{\varphi}(\mathbf{x}')\, d\mathbf{x}' = \lambda \boldsymbol{\varphi}(\mathbf{x}) \tag{4.9}$$

The eigenfunctions of the equation (4.9) (that is the POD modes of $\mathbf{s}$) are now also vector-valued functions.

The continuous operator R is a non-negative definite, compact and self-adjoint operator [Holmes et al., 2012]. Also, the Hilbert-Schmidt theorem and the non-negative definite property ensure the eigenvalues of R are monotonically non-increasing and non-negative, and the eigenfunctions φ_i are mutually orthogonal. So, without loss of generality, the eigenvalues of R can be ordered as, $\lambda_1 \geq \lambda_2 \geq \lambda_3 \geq ... \geq \lambda_N \geq 0$.

4.2 Finding POD modes

Both in experiments and simulations, a flow is often measured/recorded at a finite number of points (mesh/grid points) within a physical domain. For the computation of POD modes in the discrete observation space, the definition of the norm involved in the linear operator R (equation 4.6) needs to be adjusted. Let $\{\theta^k : k = 1, 2, \ldots, N_s\}$ be N_s observations of the scalar field θ, obtained at different times $t = t_k$. If N_g is the total number of grid points within a domain D, then each of the $\theta^k \in \mathbb{R}^{N_g}$ is a column vector that contains the information at N_g grid points. We now form a matrix, $V = [\theta^1 \quad \theta^2 \quad \ldots \quad \theta^{N_s}] \in \mathbb{R}^{N_g \times N_s}$, which is defined as the state matrix of the scalar θ. Then, the matrix VV^T is simply the auto-correlation matrix of the scalar θ, where the superscript T denotes the transpose. In $\mathbb{R}^{N_g}$, the standard inner product is defined for any θ^m and θ^n as $(\theta^m, \theta^n) = (\theta^n)^T \theta^m$. Since the time average refers to

the arithmetic mean over the ensemble, for any $g \in \mathbb{R}^{N_g}$, Rg becomes [Holmes et al., 2012],

$$Rg = \frac{1}{N_s} \sum_{k=1}^{N_s} (\theta^k)^T g \theta^k \tag{4.10}$$

The operator R is now a discrete operator which is given by

$$R = \frac{1}{N_s} \sum_{k=1}^{N_s} \theta^k (\theta^k)^T = \frac{1}{N_s} V V^T \tag{4.11}$$

That is, the discrete operator R is the averaged auto-correlation matrix VV^T/N_s. The eigenfunction problem (4.2) then reduces to a matrix eigenvalue problem

$$VV^T \varphi = \lambda \varphi \tag{4.12}$$

where, $\varphi \in \mathbb{R}_g^N$ is a column vector. Here, the factor $(1/N_s)$ has been dropped and assumed to be lumped into λ.

4.2.1 Method of snapshots

In general, a direct computational approach to solve the eigenvalue problem (4.12) is costly as the matrix VV^T is of size N_g^2 and for flow problems, N_g is generally very large. For example, if the domain $D \subset \mathbb{R}$ and the grid size N_g is 10^4, then the matrix VV^T is of order 10^8. To reduce the computational cost, Sirovich [Sirovich, 1987] developed an alternative approach known as the method of snapshots. This alternative method is described below.

As V is a rectangular matrix, the singular value decomposition can be applied to V. The singular value decomposition of the matrix $V \in \mathbb{R}^{N_g \times N_s}$ is a factorisation of the form [Taira et al., 2017],

$$V = \Phi \Sigma \Psi^T, \tag{4.13}$$

where,

1. $\Phi \in \mathbb{R}^{N_g \times N_g}$ whose columns φ_k for $k = 1, 2, \ldots, N_g$, are orthogonal eigenvectors of VV^T .

2. $\Psi \in \mathbb{R}^{N_s \times N_s}$ whose columns, Ψ_l for $l = 1, 2, \ldots, N_s$, are orthogonal eigenvectors of $V^T V$.

3. $\Sigma \in \mathbb{R}^{N_g \times N_s}$, is a diagonal matrix whose diagonal elements are the singular values σ_k, of the matrix V for $k = 1, 2, \ldots, p$, where $p = \min(N_g, N_s)$.

That is, for $k = 1, 2, \ldots, N_g$ and $l = 1, 2, \ldots, N_s$;

$$\begin{aligned} V V^T \varphi_k &= \lambda_k \varphi_k \\ V^T V \Psi_l &= \lambda_l \Psi_l \end{aligned} \tag{4.14}$$

The two equations in (4.14) possess the same eigenvalues. Now depending on the values of M and N, one of the following schemes can be adopted,

1. If $N_g < N_s$, then solve $V V^T \varphi_k = \lambda_k \varphi_k$ to find φ_k. This procedure is described as the direct method.

2. If $N_g > N_s$, then solve $V^T V \Psi_l = \lambda_l \Psi_l$ to find Ψ_l. Then the POD modes φ_l can be found as

$$\varphi_l = \frac{1}{\sqrt{\lambda_l}} V \Psi_l \tag{4.15}$$

The equation (4.15) is known as method of snapshots [Sirovich, 1987] and, can be derived substituting $V = \Phi \Sigma \Psi^T$ and $\lambda_l = \sigma_l^2$ in equation 4.14. Usually, for a flow problem, $N_g \gg N_s$ and thus the method of snapshot is computationally economical to find POD modes. The eigenvalue problem in the method of snapshots is of order N_s^2 and the number of grid points, or the dimension of the domain do not have any effect on the computation of the eigenvalues of $V^T V$. The computational costs depend only on the number of observations N_s, used to evaluate the POD modes.

Since, $V \Psi = \Phi \Sigma \Psi^T \Psi = \Phi \Sigma$ and $V = [\theta^1 \quad \theta^2 \quad \ldots \quad \theta^{N_s}]$, we can derive the following equations for $k = 1, 2, \ldots, N_g$,

$$\varphi_k = \frac{1}{\sqrt{\lambda_k}} \sum_{l=1}^{N_s} \Psi_{lk} \theta^l \tag{4.16}$$

where, Ψ_{lk} is the l-th component of Ψ_k. The equation (4.16) implies that POD modes can be expressed as a linear combination of the snapshots and thus POD modes inherit the properties of the flow field, such as boundary conditions, incompressibility and homogeneity.

In the following algorithm, a step by step procedure to find the POD modes by the method of snapshots is listed.

Algorithm

1. Arrange the flow field components for the N snapshots as, $V = [\theta^1 \quad \theta^2 \quad \dots \quad \theta^{N_s}]$.
2. Compute the matrix, $R = V^T V$.
3. Solve the eigenvalue problem $R\Psi = \lambda\Psi$ and arrange the eigenvalues in descending order.
4. Compute the POD modes using equation (4.15).

4.2.2 POD modes in the homogeneous direction

Let us consider a flow problem that is statistically homogeneous in space. That is, the statistics depend only on time. Due to the homogeneity in space, for any two points $\mathbf{x}$ and $\mathbf{x}'$ in space, the auto-correlation operator R satisfies the following property [Holmes et al., 2012],

$$R(\mathbf{x}, \mathbf{x}') = R(\mathbf{x} - \mathbf{x}') \tag{4.17}$$

Substituting the equation (4.17) in the vector-valued eigenvalue problem (4.9) results in,

$$R(\mathbf{x} - \mathbf{x}')\boldsymbol{\varphi}(\mathbf{x}') = \lambda\boldsymbol{\varphi}(\mathbf{x}) \tag{4.18}$$

Now taking the Fourier transform on the both sides of equation (4.18) and using the convolution property,

$$\widehat{R}\widehat{\boldsymbol{\varphi}} = \lambda\widehat{\boldsymbol{\varphi}} \implies \widehat{R} = \lambda \tag{4.19}$$

Where, $\widehat{\ }$ denotes the Fourier transform of the relevant quantities. The equation (4.19) implies that, in a homogeneous direction, the eigenvalues of the problem (4.9) are the Fourier coefficients of R and the eigenfunctions $\boldsymbol{\varphi}$ are the Fourier modes [Holmes et al., 2012].

4.2.3 Application to the Kuramoto-Sivashinsky equation

In this section, we design a problem to use the POD method for velocity reconstruction of the $1D$ Kuramoto-Sivashinsky (KS) equation [Hyman and Nicolaenko, 1986, Lakestani and Dehghan, 2012]. The one dimensional KS equation can be presented in normalized form [Papageorgiou, 1991, Lakestani and Dehghan, 2012] as,

$$\frac{\partial u}{\partial t} + u\frac{\partial u}{\partial x} + \frac{\partial^2 u}{\partial x^2} + \nu\frac{\partial^4 u}{\partial x^4} = 0 \tag{4.20}$$

with $u(x,0) = -\sin(x)$ and $u(x+2\pi,t) = u(x,t)$. The parameter ν is the viscosity. The PDE (4.20) arises in many physical problems including propagation of concentration waves, plasma physics, flame propagation, reaction-diffusion combustion dynamics, free surface film flows and two-phase flows [Papageorgiou, 1991]. It has reported in [Papageorgiou, 1991] that ν plays an important role to control the dynamics of the system and presented the types of attractors for a wide range of ν. For example, if $0.0599 \leq \nu \leq 0.06695$, then the trimodal steady attractor appears and for $\nu \leq 0.023$, the solution becomes chaotic. Therefore, in the present study, the value of ν is chosen as 0.01 to allow the dynamics to be chaotic. The PDE (4.20) is first transformed into Fourier space (spectral form [Gentian Zavalani, 2014])

$$\frac{d\hat{u}_k}{dt} + (\nu k^4 - k^2)\hat{u}_k = -0.5ik\hat{w} \tag{4.21}$$

where $\hat{w}_k(t) = \frac{1}{2\pi}\int_0^{2\pi} u^2(x,t)\exp(-ikx)\,dx$. Now, using the integrating factor $\exp(\nu k^4 - k^2)t$ on (4.21), we get

$$\frac{d}{dt}(\hat{u}_k \exp(\nu k^4 - k^2)t) = -\frac{ik}{2}\hat{w}_k \exp(\nu k^4 - k^2)t \tag{4.22}$$

The resulting ODE is then numerically solved using a fourth order Runge-Kutta method. For

computations a high resolution grid, $N_x = 2048$ is chosen to capture the chaotic KS dynamics. The time marching is carried out with $\Delta t = 0.01$.

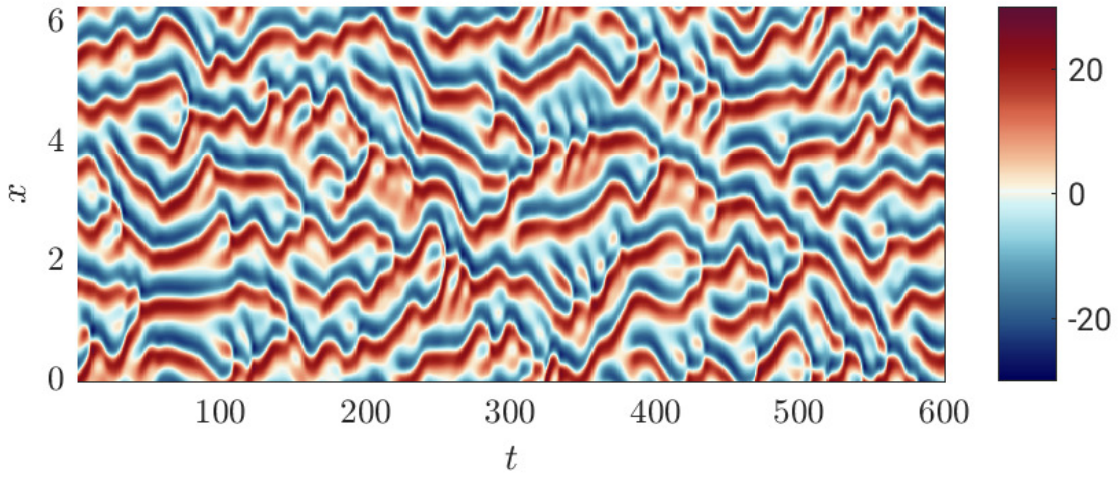

Figure 4.2: Solution of the KS equation with $\nu = 0.01$.

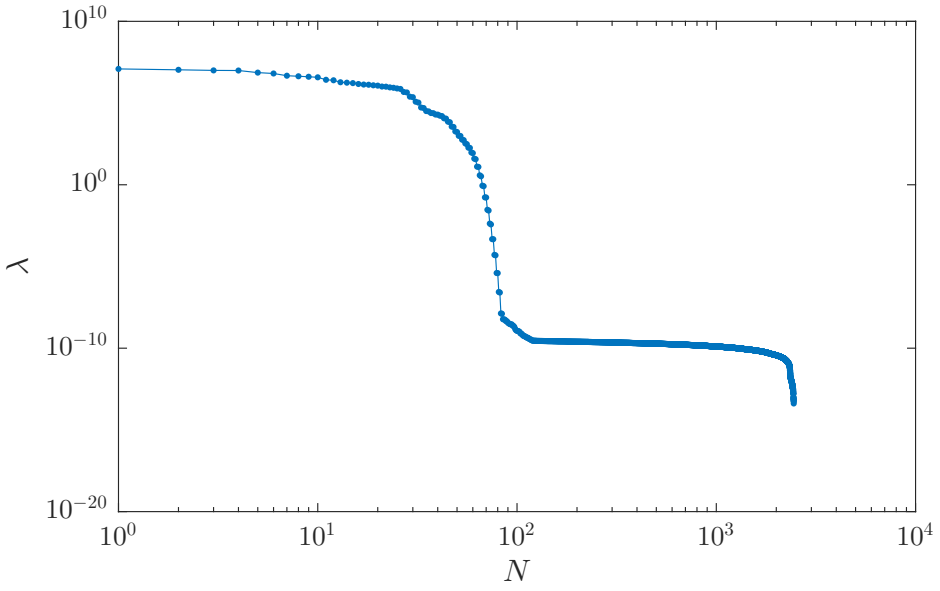

Figure 4.3: spectrum of POD modes of KS solution with $\nu = 0.01$.

Once the system is solved for a sufficiently long time, a series of 2000 snapshots are collected for the computation of POD modes. The solution is shown in the xt-plane as in the figure 4.2 for the first 300 time steps considered for the computation. Since periodic boundary conditions are adopted, the field u is homogeneous in space and the POD modes are the Fourier modes (see section 4.2.2). The snapshot at $t = 6000$ is chosen as the sample snapshot, which is not used

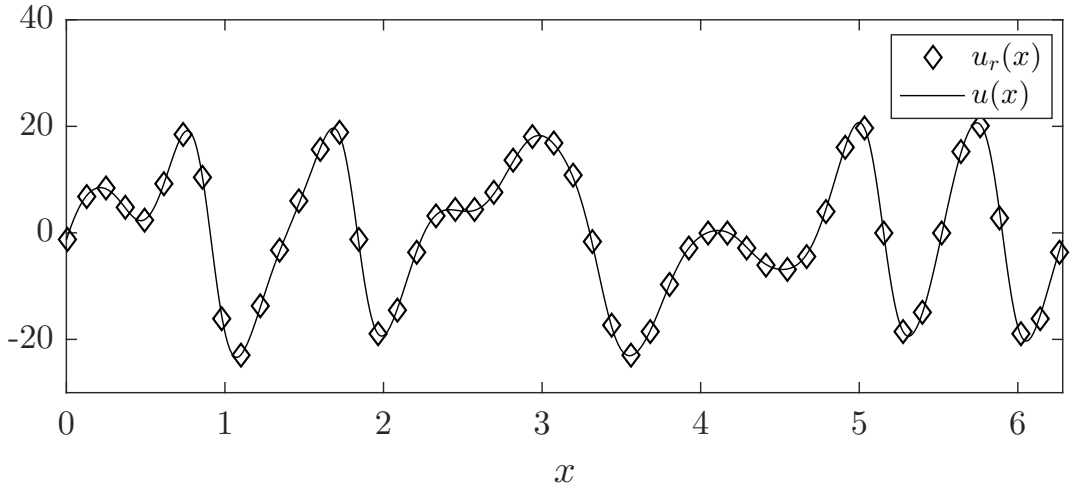

Figure 4.4: Reconstruction of the sample snapshot using 80 POD modes.

to evaluate POD modes. To reconstruct the sample snapshot as a combination of the POD modes, we need to compute the temporal coefficients $a_i(t)$. The temporal coefficients $a_i(t)$ for $i = 1, 2, \ldots, N$ are obtained by projecting the POD modes $\varphi_i(x)$ on the scalar field $\theta(x,t)$ over the entire domain D as

$$a_i(t) = (\theta, \varphi_i)_D = \int_D \theta(x,t)\varphi_i(x)\, dx \tag{4.23}$$

As seen from the spectrum of the POD modes (figure 4.3(b)), there are about 80 modes corresponding to nonzero eigenvalues (eigenvalues $< 10^{-6}$ are ignored). We use the first 80 POD modes to evaluate the temporal modes using equation (4.23). The reconstructed sample snapshot u_r is presented in the following figure 4.4 along with the original snapshot u.

To quantify the performance of the reconstructed snapshots, we define a measure of performance [Illingworth et al., 2018] as,

$$\gamma = \sqrt{\int_0^{2\pi}\int_0^T (u-u_r)^2\, dt\, dx} \Big/ \sqrt{\int_0^{2\pi}\int_0^T u^2\, dt\, dx} \tag{4.24}$$

Thus, γ is the ℓ^2-norm of the error $(u-u_r)$ normalised by the ℓ^2-norm of u. For the reconstructed snapshot u_r in figure 4.4, $\gamma = 10^{-7}$. γ is close to 0, since the spectrum 4.3 shows that there are about 128 non-zero modes exists. For a perfect reconstruction $\gamma = 0$.

Figure 4.5 shows how γ changes with the number of modes N, used for the reconstructions. For

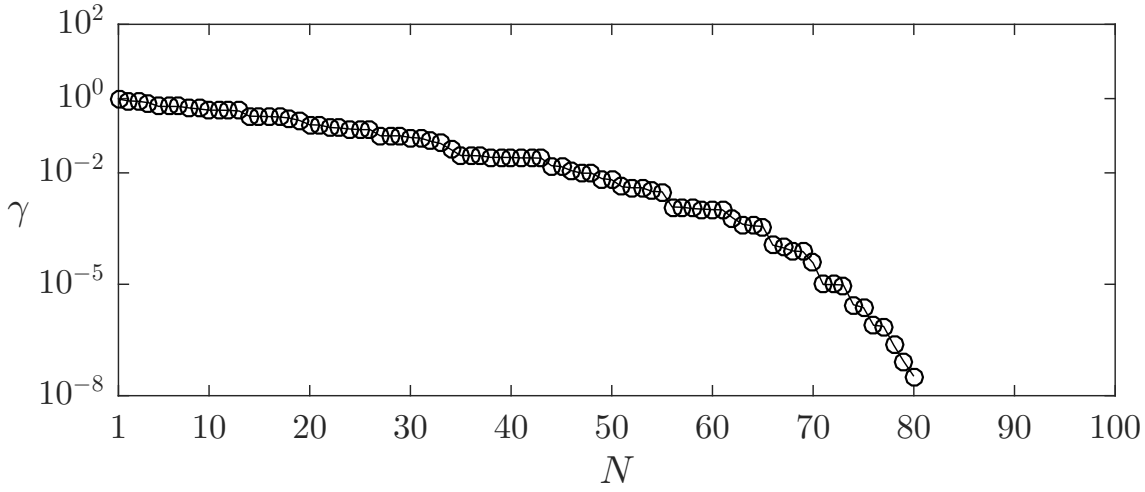

Figure 4.5: The relative error of the POD method as a function of number of the modes used for reconstruction N.

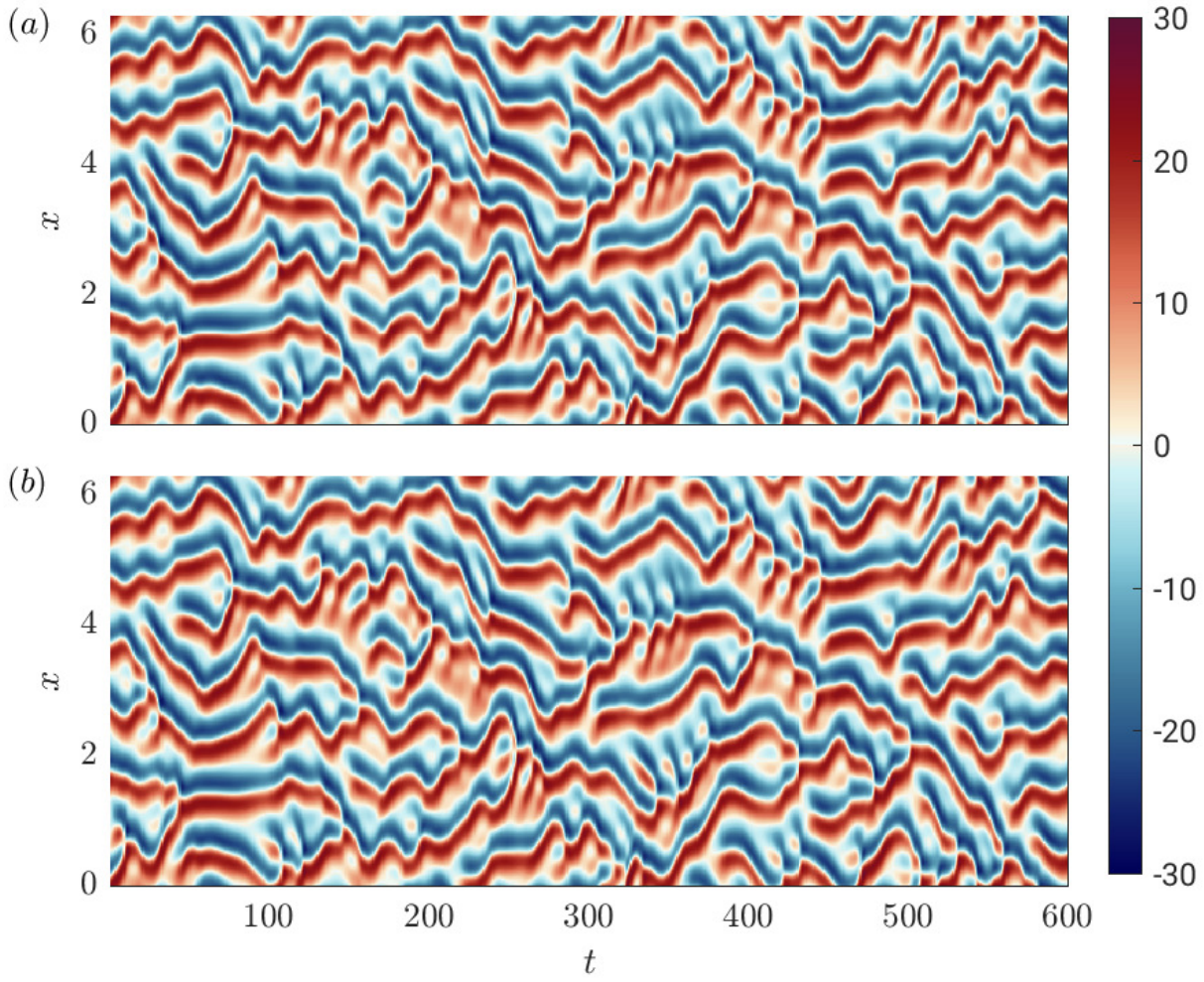

Figure 4.6: KS solution (a) and reconstruction of KS solution using 80 POD modes (b). Here, the parameter $\nu = 0.01$

example, the POD method requires about 40 modes to obtain $\gamma < 0.1$. That is, a reconstruction using the first 40 POD modes can have maximum 10% mismatches with actual snapshots. The measure γ exponentially decay for $N > 40$ and for the reconstruction using 80 modes $\gamma = 10^{-8}$. A reconstruction of KS solution with 80 POD modes in the x-t plane with $\nu = 0.01$ is shown in figure 4.6, which shows a good reconstruction is achieved.

4.2.4 Application to plane Couette flow

We will now evaluate POD modes of the DNS results of plane Couette flow. To keep the problem simple, we will restrict the reconstruction to the yz-plane only, where y and z are the spanwise and the wall normal direction respectively.

Since the flow is homogeneous in the spanwise direction, the POD modes in spanwise direction become the Fourier modes (section 4.2.2). That is, the POD modes in the spanwise direction can be written as

$$\boldsymbol{\varphi}_n(\mathbf{x}) = \sum_{n_y} \hat{\boldsymbol{\varphi}}_{nn_y}(z) \exp\left(i\frac{2\pi n_y y}{L_y}\right)$$

where, $(\mathbf{x}, t)$ is the n-th POD mode and $\hat{\boldsymbol{\varphi}}_{nn_y}$ are the POD modes in the wall normal direction.

The state variable in the yz-plane can be expressed as the linear combination of the POD modes as [Moehlis et al., 2002]

$$\mathbf{s}(\mathbf{x}, t) = \sum_{n} \sum_{n_y} a_{nn_y}(t) \hat{\boldsymbol{\varphi}}_{nn_y}(z) \exp\left(i\frac{2\pi n_y y}{L_y}\right) \tag{4.25}$$

Here, $\mathbf{x} = (y, z)^T$ are the coordinates, $\mathbf{s} = (u, \theta_w)^T$ is the state variable, u is the streamwise velocity component and θ_w is the wall temperature, n_y is the spanwise wavenumber, a_{nn_y} are the temporal coefficients, L_y is the lengths in the spanwise direction. The state variable $\mathbf{s}$ has two components – the streamwise flow velocity u and the wall temperature θ_w. This choice of the state variable is motivated from the key problem at hand – reconstructing the flow velocity

using only the wall temperature. However, we are not solving the key problem in this section and it will be a topic for section 4.4.

Since, $\mathbf{s}$ is vector-valued, $\hat{\boldsymbol{\varphi}}_{nn_y}$ are also vector-valued with components $\hat{\varphi}_{nn_y,\theta_w}$ and $\hat{\varphi}_{nn_y,u}$, corresponding to θ_w and u, respectively. The index n is sometimes termed as the quantum number [Moehlis et al., 2002] and $\hat{\boldsymbol{\varphi}}_{nn_y}$ is the n-th POD mode corresponding to wavenumber n_y.

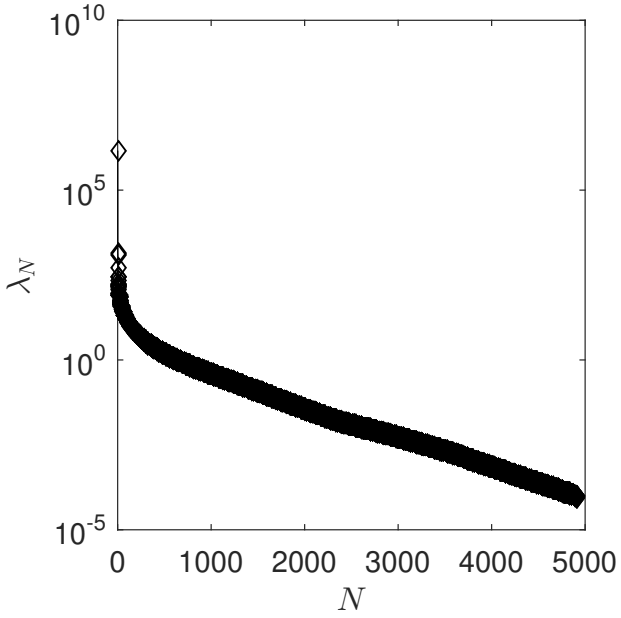

Figure 4.7: POD spectrum of the state variable $\mathbf{s} = (u, \theta_w)^T$.

To evaluate the POD modes we use the plane Couette flow data-set DNS described in chapter 2. An ensemble of total 5600 DNS snapshots of the state variable $\mathbf{s} = (u, \theta_w)^T$ on the yz–plane at $x^+ = 526$ is used. We apply the method of snapshots to evaluate POD modes and plotted in figure 4.7 is the eigenvalue spectrum of the modes. The spectrum does not vanish within the first few modes and for a good reconstruction, we need to use a large number of modes [Podvin et al., 2006, Moehlis et al., 2002, Wang et al., 2012, Gal Berkooz et al., 1993]. How the quality of reconstructions depend on the number of modes is discussed later in this chapter.

The first three modes are shown in the figure 4.8. The first mode is the mean mode $(n_y, n) = (0, 0)$, and the other two modes corresponds to $(n_y, n) = (0, 2)$ and $(1, 0)$, respectively. The mode $(0, 0)$ is the mean mode and is the only real mode of the flow. The modulus of the modes

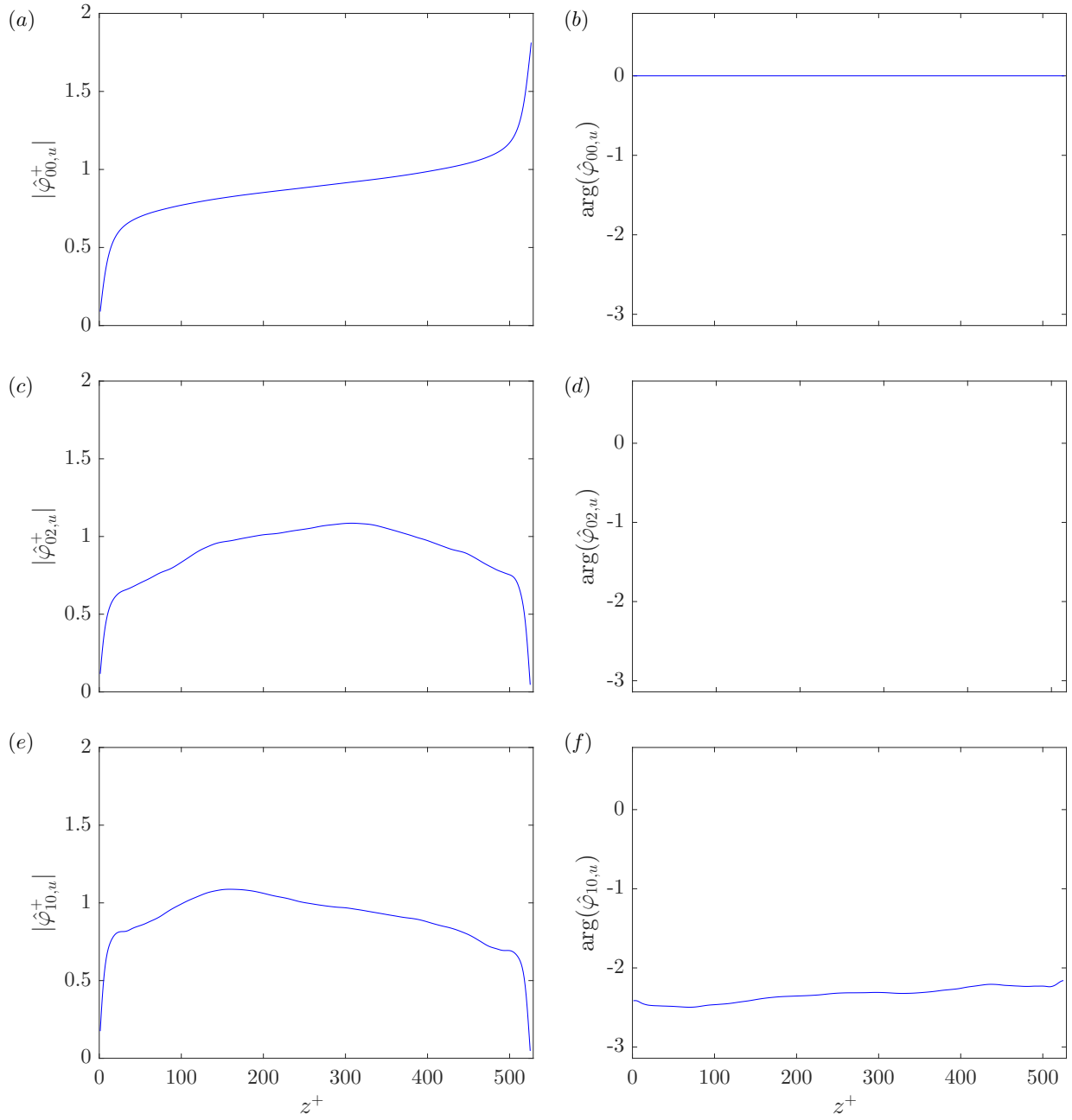

Figure 4.8: The first three POD modes, presented in ascending order: (a) $|\hat{\varphi}^+_{00,u}|$, (b) $\arg(\varphi_{00,u})$, (c)$|\hat{\varphi}^+_{02,u}|$, (d) $\arg(\varphi_{02,u})$, (e) $|\hat{\varphi}^+_{10,u}|$ and (f) $\arg(\varphi_{10,u})$. The moduli of the modes are shown in Plus unit.

$(0, 2)$ and $(1, 0)$ have a common pattern as they sharply rise in the buffer layer. The phases of the modes $(0, 2)$ and $(1, 0)$ are not constant along the channel height, and have a phase lag $\pi/4$ approximately.

A sample snapshot (figure 4.9)(a), which is not used to compute the POD modes, is chosen to be reconstructed. The temporal coefficients are computed by using the equation (4.23) and the reconstructed snapshot using 500 modes is presented in the figure 4.9(b). Visual inspection of

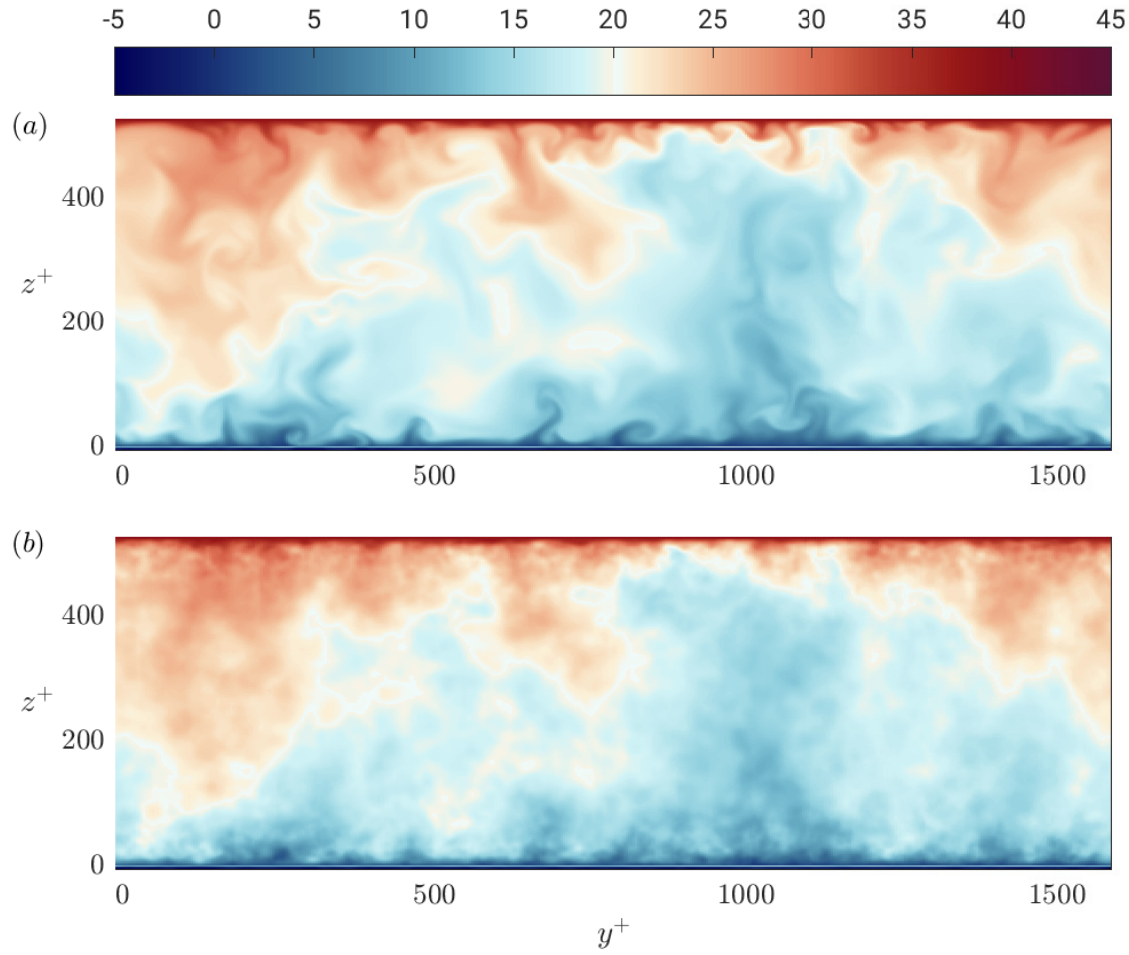

Figure 4.9: A DNS snapshot of the streamwise component u of velocity on the yz plane at $x^+ = 526$ (a) and reconstructed snapshot using 500 POD modes (b). The measure of performance γ of the reconstructed snapshot in figure (b) is 0.03.

the reconstructed snapshot confirms the good quality of the reconstruction except possibly for the peaks, which is due to the truncation of modes $N > 500$. The reconstructed velocity in the yz-plane is presented for $t^+ = 110.526$ in figure 4.9. We found similar results for a set of other time steps and evaluate the measure of performance γ over all the time steps on the set as

$$\gamma = \sqrt{\int_0^T \int_0^{L_y} \int_0^h (u - u_r)^2 dz dy dt} / \sqrt{\int_0^T \int_0^{L_y} \int_0^h u^2 dz dy dt}$$

where, u and u_r are the velocity obtained from DNS and the reconstructed velocity, respectively. The measure of performance γ of the set of reconstructed snapshots is 0.03.

4.3 Reconstruction of a gappy field

In this section, we will discuss how the POD method can be used for reconstructions with incomplete observations. Suppose, φ_i are the POD modes of a scalar field θ. Then to reconstruct the scalar field θ, only the temporal modes a_i need to be evaluated. Now imagine that the modes φ_i and some of the observations of the field θ are given. The incomplete or gappy observation is denoted by $\tilde{\theta}$, which is related to the full observation θ as

$$\tilde{\theta} = m\theta \tag{4.26}$$

where,

$$m(\mathbf{x}) = \begin{cases} 1; & \text{where information is available} \\ 0; & \text{elsewhere} \end{cases}$$

is a mask function. Then equation 4.26 and 4.2 yield,

$$\widetilde{\theta} = \widetilde{\theta}(\mathbf{x}, t) = m(\mathbf{x})\theta(\mathbf{x}, t) = m(\mathbf{x}) \sum_{i=1}^{N} a_i(t)\varphi_i(\mathbf{x}) \tag{4.27}$$

Let us assume the modes φ_i is available. Then to obtain θ, one needs to approximate a_i and can be found from the minimization problem ([Everson and Sirovich, 1995]),

$$\min_{a_i} E = \min_{a_i} \int_{\widetilde{D}} \left(\widetilde{\theta}(\mathbf{x}, t) - m(\mathbf{x}) \sum_{i=1}^{N} a_i(t)\varphi_i(\mathbf{x}) \right)^2 d\mathbf{x} \tag{4.28}$$

For the minimization,

$$\begin{aligned}
0 =& \frac{\partial E}{\partial \widetilde{a}_k}, \quad \text{for } k = 1, 2, \ldots, N \\
&= 2 \int_D m(\mathbf{x}) \varphi_k(\mathbf{x}) \left(\widetilde{\theta}(\mathbf{x}, t) - m(\mathbf{x}) \sum_{i=1}^{N} a_i(t) \varphi_i(\mathbf{x}) \right) d\mathbf{x} \\
&= 2 \int_D m(\mathbf{x}) \varphi_k(\mathbf{x}) \widetilde{\theta}(\mathbf{x}, t)\, d\mathbf{x} - 2 \sum_{i=1}^{N} a_i(t) \int_{\widetilde{D}} m(\mathbf{x}) \varphi_k(\mathbf{x}) m(\mathbf{x}) \varphi_i(\mathbf{x})\, d\mathbf{x} \\
&= 2 \int_D \widetilde{\varphi_k}(\mathbf{x}) \widetilde{\theta}(\mathbf{x}, t)\, d\mathbf{x} - 2 \sum_{i=1}^{N} a_i(t) \int_D \widetilde{\varphi_k}(\mathbf{x}) \widetilde{\varphi}_i(\mathbf{x})\, d\mathbf{x}, \quad \text{for } k = 1, 2, \ldots, N.
\end{aligned}$$

where, $\widetilde{\varphi}_k = m(\mathbf{x})\varphi_k(\mathbf{x})$. Now, denoting $M_{ik} = \int_D \widetilde{\varphi}_k(\mathbf{x})\widetilde{\varphi}_i(\mathbf{x})d\mathbf{x}$, $f_k = \int_D \widetilde{\varphi}_k(\mathbf{x})\widetilde{\theta}(\mathbf{x}, t)d\mathbf{x}$ and $\widetilde{a} = [\widetilde{a}_1 \quad \widetilde{a}_2 \quad \ldots \quad \widetilde{a}_N]^T$, the minimisation problem (4.28) reduces to a system of linear equations [Everson and Sirovich, 1995],

$$M\widetilde{a} = f \tag{4.29}$$

The above system of linear equations can be solved to find $a_i(t)$. Clearly, if a full observation θ is available then M would be an identity matrix and $a = f$. This method is known as gappy POD method and has been proposed by Everson and Sirovich. They applied the POD modes to recover images of human faces when only 10% pixel information were available. They defined a ratio p as

$$p = \frac{\text{Available pixels}}{\text{Total pixels}} \tag{4.30}$$

and reported that for $p > 0.2$ the reconstruction ability is good. They also presented a case with $p = 0.05$, where the reconstruction procedure diverges for $N > 50$ and the resulted image was a poor approximation of the real image.

4.3.1 Application to gappy KS problem

To form a gappy problem with the KS equation, we assume that out of 2048 grid points, information is available only at 64 equidistant points. We consider 128 degrees of freedom

corresponding to non-zero frequencies from the spectrum (figure 4.3). Although we have 2048 grid points, we consider the number of non-zero frequencies to compute the ratio p. Thus the ratio, $p = 64/128 = 0.5$.. This is the same problem discussed in section 4.2.3, except with missing information – a gappy problem. The POD modes obtained in section 4.2.3 are the Fourier modes due to the homogeneity of the problem. Using the modes, we evaluate the matrix M and f of the equation 4.29. The system is then solved for the temporal coefficients a_i and the field u is reconstructed as u_r. Plotted in figure 4.10 is the reconstructed field u_r using 62 POD modes with the actual field u. Visual inspection confirms a good reconstruction is achieved.

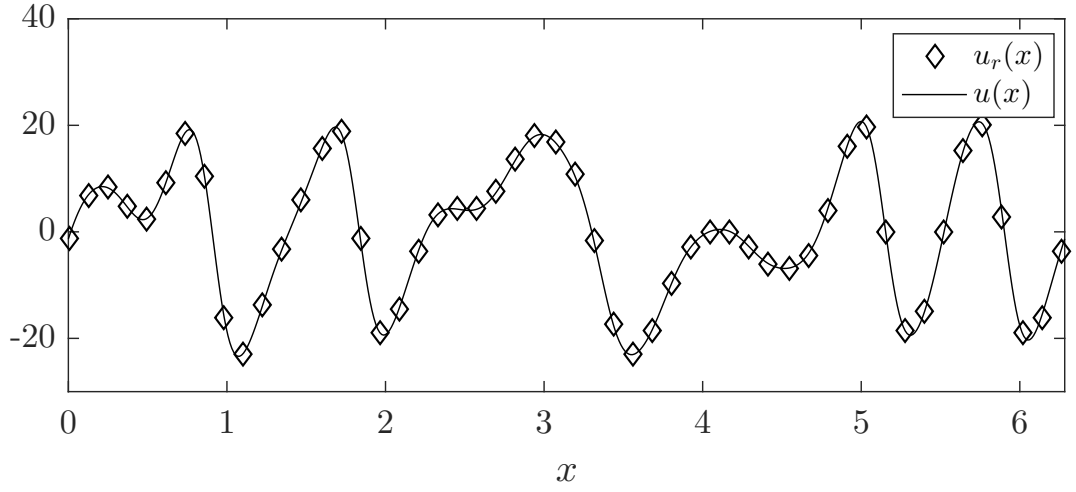

Figure 4.10: Reconstruction of the sample snapshot using 62 POD modes with $p = 0.5$.

As discussed in section 4.2.3, for the KS dynamical equation, the first 40 POD modes can reproduce a snapshot with relative error less than 10% and thus the gappy field is reconstructed well even for the small value of the ratio. In this case, with $p = 0.5$, temporal coefficients for 62 modes are approximated. Depending on the available information, the relative error to approximate the sample snapshot is shown in the figure 4.11. It is also clear that, for each p, the relative error is similar to the case $p = 1$, before they diverge. That is, with missing information, a reconstruction for this problem up to a certain number of modes is always possible. Thus, the performance of the reconstruction depends on how much these certain number of modes are able to recapture the dynamics.

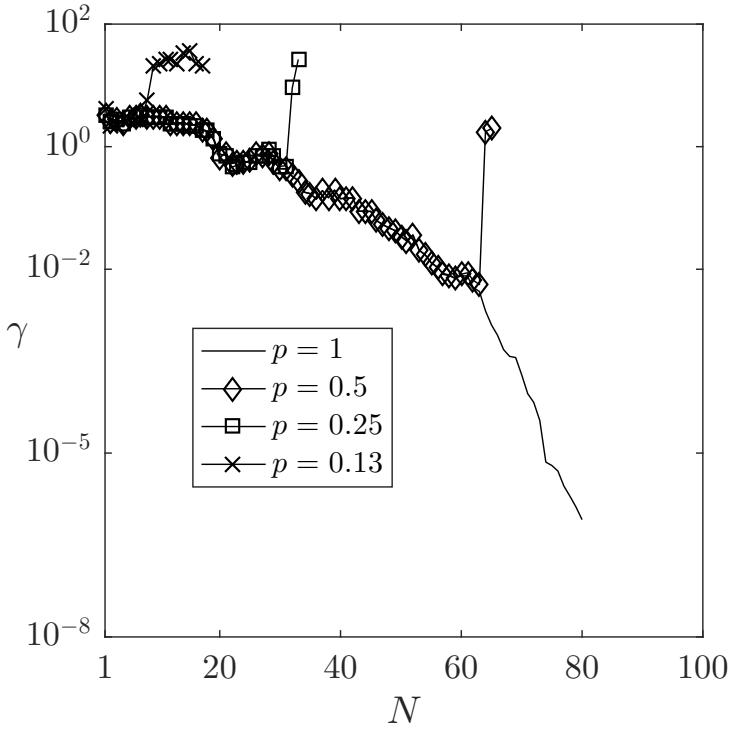

Figure 4.11: The measure of performance γ of the reconstructed KS snapshots using POD modes for different $p = 1$, 0.5, 0.25 and 0.13.

4.3.2 Application to gappy plane Couette flow

A gappy field is considered by sampling the snapshot (figure 4.9(a), yz-plane) in the z (wall normal) direction. From the actual resolution of the sample snapshot 432×432, 25 equidistant z-locations are sampled and all grid points in the y (spanwise) direction are used. Therefore, the ratio of the available resolution to the total resolution is $p \approx 0.046$.

We will use the POD modes to reconstruct the sample snapshot. As the modes are known, the temporal coefficients can be computed using (4.29). Comparing the figures 5.11(a-b), the reconstruction from the partial information (here only 4.6%) is sufficiently good.

If the total information were known, that is, for $p = 1$, the matrix M would be an identity matrix. For a gappy field, $\| M \|$ deviates from unity. From the spectrum (figure 4.7) of the POD modes, there are 4642 modes corresponding to nonzero eigenvalues ($\geq 10^{-3}$). Comparing to the first eigenvalue corresponding to the mean mode, other eigenvalues are relatively small and the tail of the spectrum does not vanish within the first few modes. That is, $\| M^{-1} \|$ will

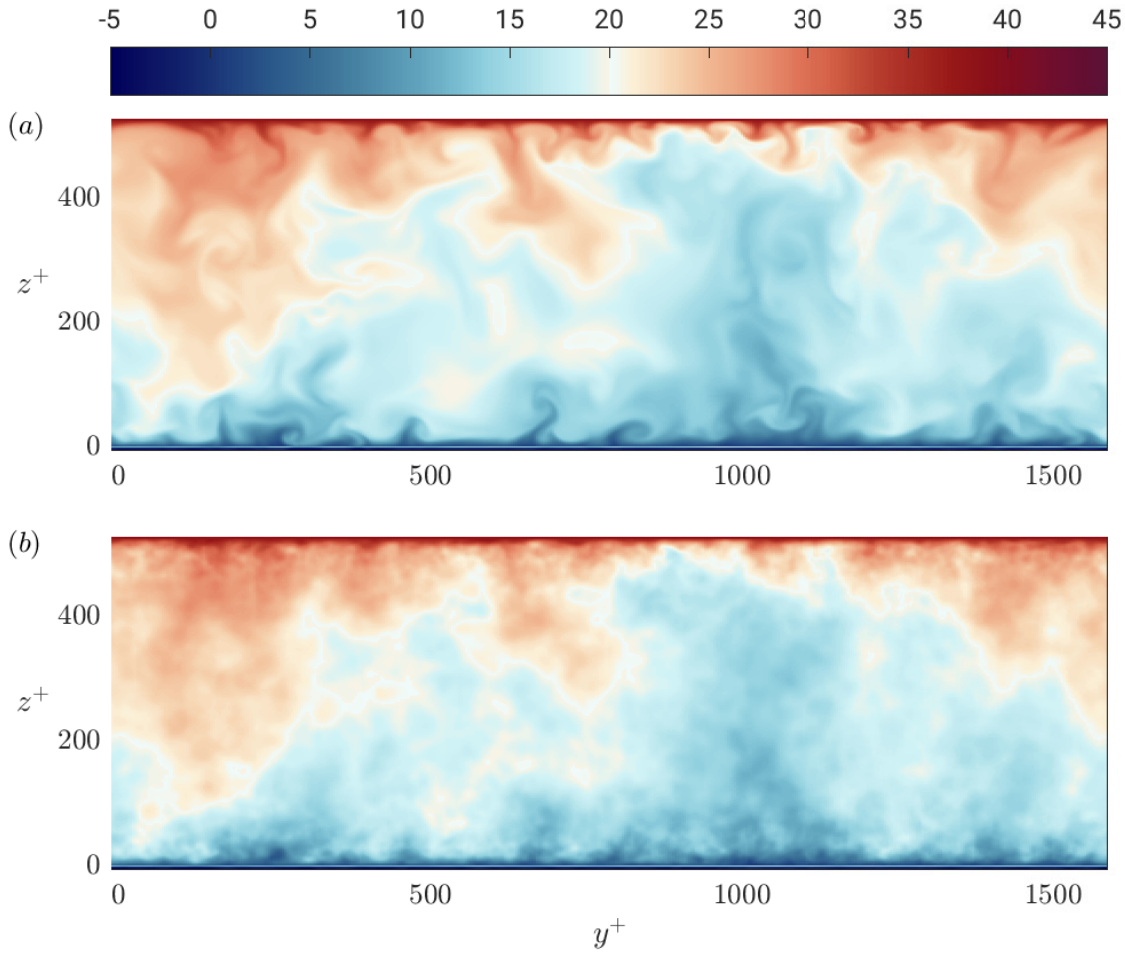

Figure 4.12: The streamwise velocity u^+ at $x^+ = 526$ (a) and the reconstructed field using 4.6% of total information and 500 POD modes.

be the dominant factor for the convergence of the reconstruction process [Everson and Sirovich, 1995]. In the present gappy field, however, 4.6% pixel information is enough to capture the sample snapshot and the reconstructed field is shown in the figure 4.12.

Another important observation is that, similar to the KS problem, the cases with $p \leq 0.086$ follow the convergence path of the case $p = 1$ up to some N and then diverge. The case $p = 0.002$ corresponds the problem, where only θ_w is available and figure 4.13 shows that the reconstruction of the state variable $\mathbf{s} = (u, \theta_w)^T$ diverges for $N > 5$. It is obvious that with only 5 modes, the reconstructed field will be a poor approximation of the actual field. This limiting case of only having wall data will be discussed in next section — where we will analyse the reason of the divergence and will modify the strategy to get a good reconstruction.

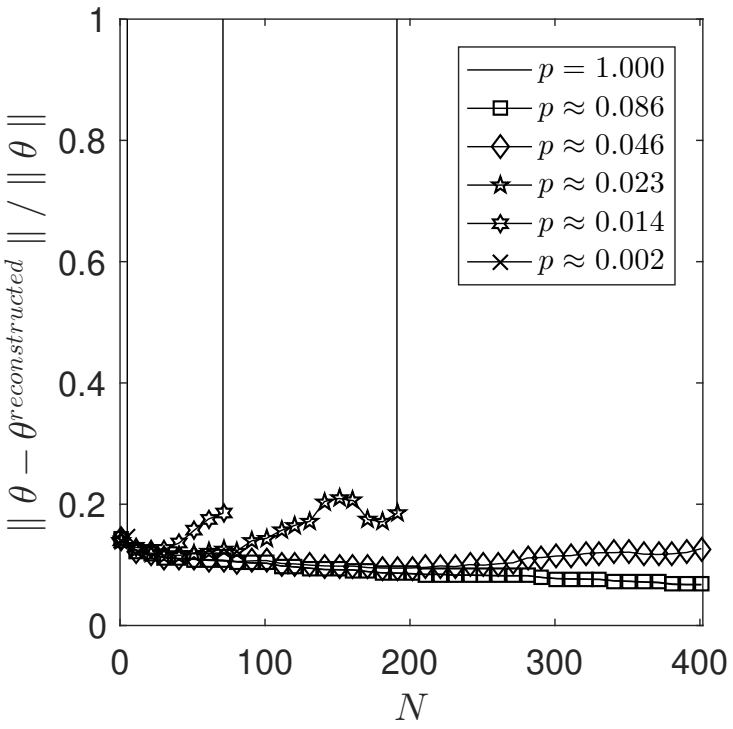

Figure 4.13: The relative error in the reconstruction using the POD modes for different values of p.

4.4 Extrapolation from the wall temperature

In this section, we will focus on the key application — reconstructing streamwise velocity component from wall temperature. To do so, a gappy problem is formed by assuming that all the information except the observations at the bottom boundary (wall temperature, shown as filled black circles in figure 4.14) are missing. This can be viewed as a limiting case of the example described in section 4.3.2 with $p = 0.002$. It is to be noted that, p is grid dependent and the value of p could sometimes be misleading. For example, one can be biased to consider a large number of measurement points on the wall ($z = 0$) compare to other vertical positions along the channel height and p could be near unity. To avoid this measurement bias, we consider the same number of grid points on the wall as the other vertical positions.

First, the POD modes are used to reconstruct the sample snapshot. Since only 5 modes can used in this limiting case (subsection 4.3.2), the reconstruction of the sample snapshot is poor. The restriction on the use of such a few number modes arise from the the ratio p. Since $p \approx 0.002$

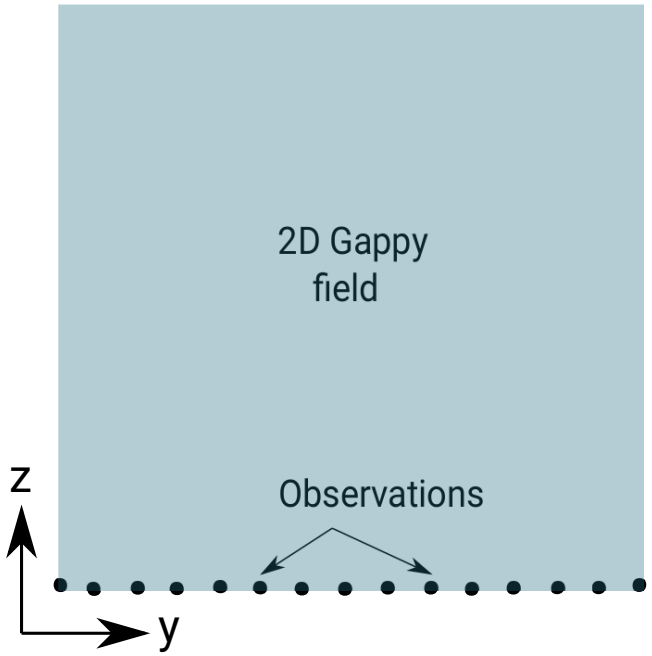

Figure 4.14: A typical $2D$ gappy field (limiting case) is shown. The only available information are the measurements (wall temperature) at the bottom wall.

is very small and the first 5 modes are not enough to describe the dynamics, $\parallel M^{-1} \parallel$ becomes very large. An alternative description is also possible by using the condition number of the matrix M, which is defined as, $\parallel M \parallel\parallel M^{-1} \parallel$. As long as the matrix M is well conditioned, a good reconstruction is possible. The condition number and the relative error for the different number of modes used for the reconstruction (using the POD modes) are plotted in the figure 4.15a and 4.15b.

It is clear that, $\parallel M \parallel\parallel M^{-1} \parallel \gg 1$ for $N > 5$ and thus the reconstruction with more than 5 modes diverges. The reconstructed sample snapshot with 5 modes is presented in figure 4.16. It can be seen from the figure that the reconstructed snapshot produces large scale structures only but does not capture dynamically important coherent structures near the bottom wall. Since the reconstruction procedure restricted to the mean mode (first mode) and only four dominant modes corresponds to the fluctuations, the POD modes fails for the limiting case considered in this example. How a snapshot can be reconstructed using only wall temperature via regularisation will be described in the next section.

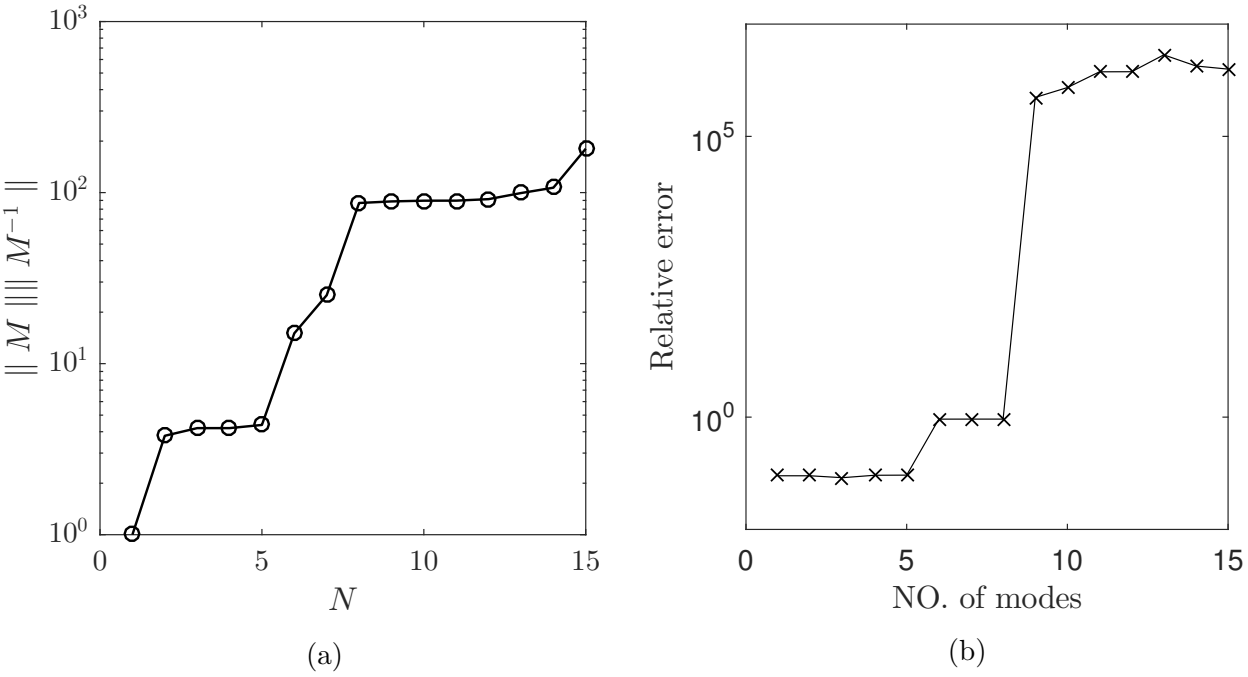

Figure 4.15: Condition number of M (a), relative error in the reconstruction using the POD modes (b). Here, the ratio parameter $p = 0.002$.

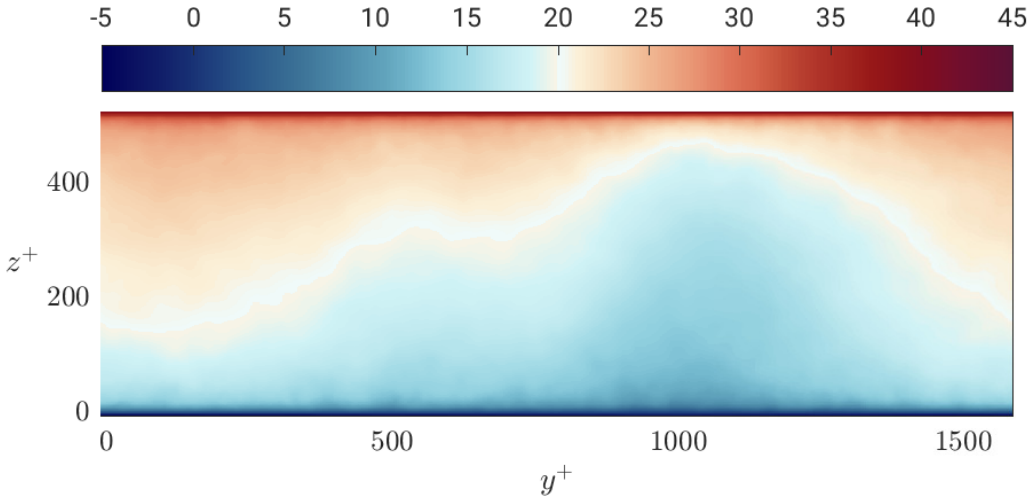

Figure 4.16: The reconstructed field with 5 POD modes.

4.4.1 Regularisation

When reconstructing a gappy snapshot, it is required to solve a system of linear equations (4.29). A parallel statement of solving such a system of equations is to search for a minimum

(in least squares sense) of the following optimisation problem

$$\min_{\tilde{a}} \parallel f - M\tilde{a} \parallel_2^2 \tag{4.31}$$

where, $\parallel . \parallel_p$ is the ℓ^p- norm.

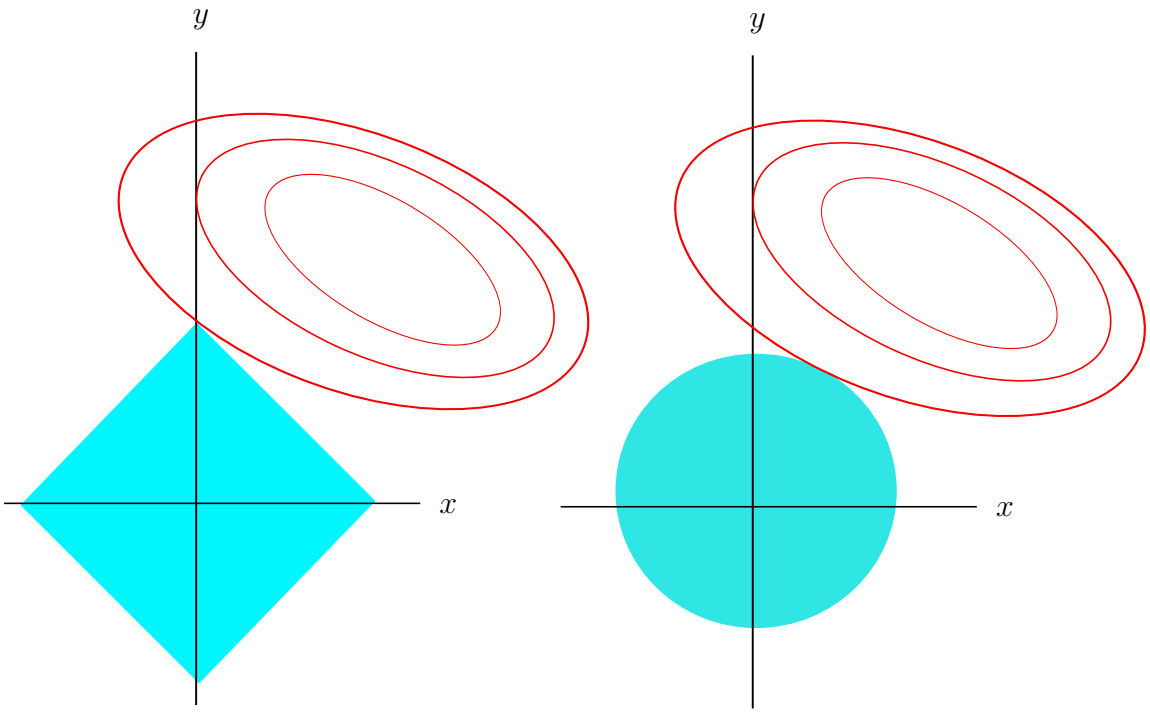

Figure 4.17: Illustration of the LASSO (left) and Tikhonov (right) regularisations. The family of ellipses represents solution space. The LASSO regularisation penalise a system by introducing a constraint $|x+y| < \alpha$ (square region,left figure), whereas the Tikhonov regularisation introduces a constraint $x^2 + y^2 < \alpha$ (circular region right figure).

By considering M to be the system matrix corresponding to an under-determined system of linear equations, we prompt to regularise the system. A regularisation of the above problem can be achieved by penalising the coefficient vector a_i as

$$\min_{\tilde{a}} \left(\parallel f - M\tilde{a} \parallel_2^2 + \alpha \parallel \tilde{a} \parallel_p \right) \tag{4.32}$$

where, α is a regularisation parameter. For $p = 1$ and $p = 2$, the regularisation methods are known as LASSO (Least Absolute Shrinkage and Selection Operator) and Tikhonov regularisation, respectively. Let us illustrate these two regularisations in xy-plane as in figure 4.17. The first norm in (4.32) presents an infinite family of quadratic functions and the second norm forms

a square and circular restrictions for LASSO and Tikhonov regularisation, respectively. The parameter α then can be chosen to select a constrained solution of the optimisation problem 4.32 (thus regularising the problem). The difference between LASSO and Tikhonov regularisation is that LASSO heavily penalises a subset of the components of a_i, whereas Tikhonov regularisation penalizes all the components uniformly.

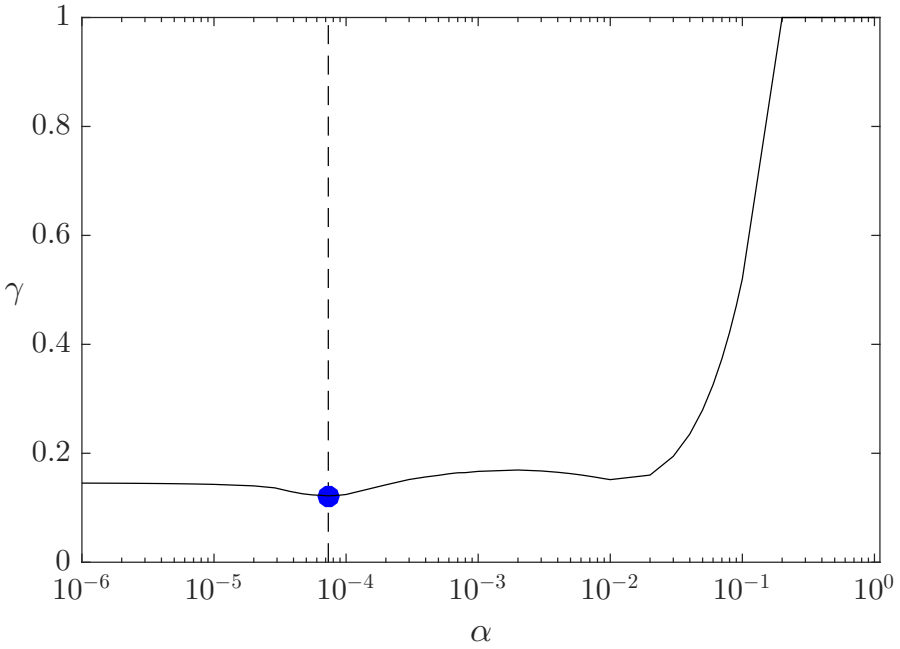

Figure 4.18: The measure γ of reconstruction against regularising parameter α. The blue circle indicates the minimum relative norm which correspond to $\alpha = 7.33 \times 10^{-5}$.

In the example of reconstruction using only thermal wall patterns, the problem becomes ill-conditioned as some of the columns of M matrix become linearly dependent. Recall that the columns of M matrix represents interaction between two POD modes. Since information is available only at the bottom wall, the mask variable m becomes sparse. Due to the large sparsity, some of the columns of matrix M become linearly dependent. Here, LASSO is a better choice, since it can select and penalise modes corresponding to such linearly dependent columns and, the remaining columns can be used for reconstruction.

To choose the value for α, 200 DNS snapshots were chosen and reconstructed using the POD modes with LASSO for a series of α values and the minimum relative norm was found as 9.11×10^{-5} (figure 4.18). This value was then used to reconstruct other snapshots.

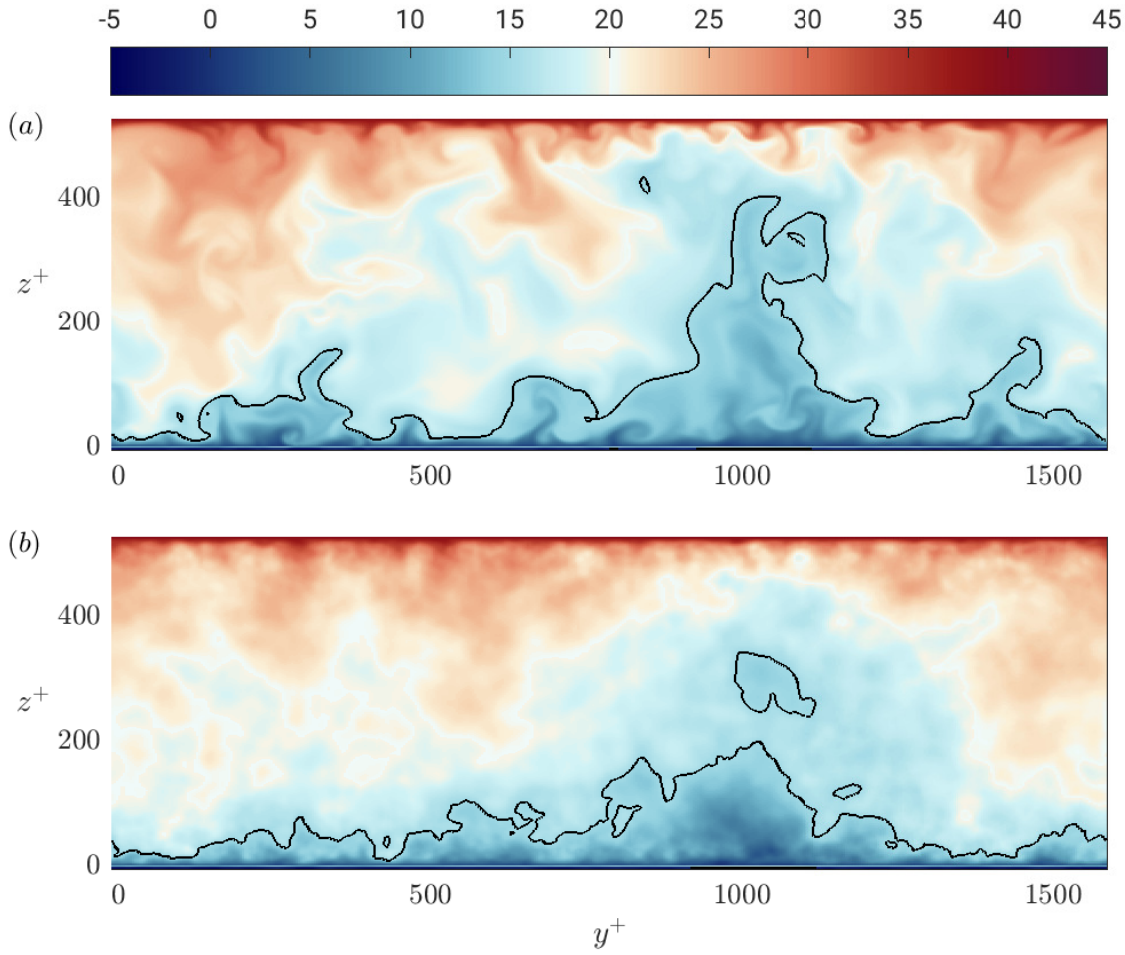

Figure 4.19: The streamwise velocity field u^+ at $x^+ = 526$ (a), the reconstructed streamwise velocity field using POD method with regularisation (b). The contour $u^+ = 15$ is shown explicitly in figures (a-b) to visualize a global flow structure and the reconstruction, respectively.

The reconstructed velocity field is shown along with the actual field in the figure 4.19. Visual inspection of the figures show that, LASSO regularisation leads to a satisfactory reconstruction. The contour $u^+ = 15$ on the figure 4.19(a) captures a large structure of the velocity field and the reconstruction of that structure using LASSO on the figure 4.19(b) is a good approximation. The measure γ of the reconstruction is 0.24.

4.5 Conclusions

We estimated POD modes of 1D Kuramoto-Sivashinsky solution with $\nu = 0.01$ and plane Couette flow at $Re_\tau = 263$. The POD method provides the most (in ℓ_2-norm) efficient way to represent a complex flow as a linear combination of modes. Indeed, POD is a linear process [Holmes et al., 2012]. The optimality of POD modes are referred only with respect to other linear representations.

To reconstruct streamwise flow velocity from wall temperature, we set up test cases/examples with increasing complexity. The objective was to test the performance of POD modes for a range of values of p (p is the ratio of available pixels to total pixels). The first set of examples were cases with $p = 1$. Here, we reconstructed the 1D KS solution and the streamwise component u of plane Couette flow on a 2D yz-plane. In both cases, we got good reconstructions with the measure of performance $\gamma = 10^{-7}$ and $\gamma = 0.03$, respectively. For the plane Couette flow, we reconstructed the streamwise velocity component u on a yz plane using 500 POD modes. The reconstruction produced the flow structures close to the actual DNS except possibly at the peaks due to the truncation of modes $N > 500$.

The second set of examples were set to test the performance of POD modes for gappy fields. We found that 4.6% pixels are sufficient to reproduce KS dynamics whereas for the reconstruction of plane Couette flow with 6.3% pixels, $\gamma = 10^{-7}$. For all p, the γ versus N curves collapsed to one curve until they diverged at a certain N. That is, the quality of reconstructions for all p are same up-to a certain number of mode N.

Finally, we proceeded to our key problem — reconstruct streamwise flow velocity from wall temperature only. This is a limiting case of the second set of problems with $p = 0.002$. With little information at hand, the reconstruction diverged for $N > 5$. For $p = 1$, the system matrix is an identity matrix. For smaller p, the columns of M increasingly became linearly dependent to each other. Recall that, the columns of M are the interactions between modes within subspace consisting of available pixels only. We applied LASSO regularisation to select and omit modes corresponding to linearly dependent columns of M. Unlike ℓ_2-regularisation,

LASSO penalises certain coefficients heavily compared to other coefficients. The characteristics of automatic detection and selective penalisation of LASSO make it a suitable choice for the problem at hand. The measure of performance γ of the resulted reconstructions with LASSO was found to be 0.24.

The idea of using POD method to reconstruct flow velocity was motivated by the optimality (in energy norm) of the POD modes. The reconstruction using the POD method captured the flow structures which are only energetically significant. For example, the reconstruction in the section 4.2.4 is missing peaks due to the truncation of modes. Similarly in many other cases, the dynamically significant flow structures may not be energetically significant [Schmid, 2010]. For examples, flows around a corner [Podvin et al., 2006, Xiao, 2016] and boundary layer flows [Pirozzoli et al., 2014, Kasagi et al., 1992]. In these flow problems, local flow structures evolve differently compared to the rest of the flow [Tsukahara et al., 2006]. Since these flow structures are local in space, it is convenient to divide the physical domain and consider the local flow within a smaller subdomain. If the POD method is now applied within a subdomain then the optimality (in energy norm) of these new modes may better represent the dynamically important local flows. We will explore this idea of dividing a domain in the next chapter to develop a decomposition method — the subdomain POD method.

Chapter 5

Estimating flow from thermal wall patterns using subdomain POD method

In this chapter, we propose a new decomposition method, termed as subdomain POD method. In this method, we first divide a domain into several smaller subdomains and standard POD method is then applied to each subdomain—resulting subdomain POD modes. The subdomain POD method is motivated from the limitation of standard/global POD method to reconstruct the flow structures associates with higher order modes — which are usually truncated. Since the POD method is applied within each subdomain, the resulting subdomain POD modes are locally optimal (in energy norm). These locally optimal modes can produce better reconstruction of the local flows within each subdomain compared to the standard POD modes. To test and apply subdomain POD modes to extract velocity from wall temperature, we use the same sets of problems as chapter 4, namely the KS equation with $\nu = 0.01$ and the DNS of plane Couette flow at $Re_\tau = 263$. We also formulate gappy problems for both cases and test the performance of subdomain POD modes. In all cases, the performance of subdomain POD modes are compared with standard POD modes. Finally, we apply subdomain POD modes to the key problem where only wall temperature is known (large gappiness) and the velocity is reconstructed.

5.1 Subdomain POD method

In the POD method, a flow field is represented as a linear combination of modes [Holmes et al., 2012, Sirovich, 1987, Everson and Sirovich, 1995]. POD modes can be arranged in an ascending order based on kinetic energy [Holmes et al., 2012]. To reconstruct local flows associated with relatively lower energy scales, a large number of modes are required [Gal Berkooz et al., 1993, Deane and Sirovich, 1991, Sirovich and Deane, 1991]. This is due to the fact that POD modes are optimised in ℓ_2-norm over entire domain. For the objective to reconstruct a flow locally, we propose to use locally optimised modes — subdomain POD modes. In this novel subdomain POD method, a complex flow topology with large degrees of freedom is divided into a set of smaller subdomains, reducing the degrees of freedom significantly. Subdomain POD modes are also suitable for boundary layer flows that have layered characteristics such as the coherent structures in near wall region. Xiao et al. applied such local modes along with radial basis functions to a flow past a cylinder [Xiao et al., 2017, Xiao, 2016] and 2D urban street canyons [Xiao et al., 2017]. They selected suitable topology for subdomains to capture certain flow aspects, such as the flow past a building in the urban street canyon case.

The Novel subdomain POD method is closely related to the finite element method [Gouri Dhatt et al., 2012] and the spectral method [Gentian Zavalani, 2014, Sieber et al., 2016]. In the finite element method, a function is approximated as a combination of the nth order polynomials (standard basis functions) whereas the spectral method represents the function as a combination of known functions, for example, Chebyshev polynomials [Canuto, 1986]. The spectral method is also applied to multi-domain problems [Quarteroni, 1987] to approximate a function locally, using collocation points to ensure the continuity at the subdomain boundaries. Compared to these methods, the subdomain POD method uses data-driven basis functions (modes), obtained from a set of observations of an unknown function. In the spectral method, the choice of the known functions greatly influence the accuracy of the approximation and the best choices are, in fact, the subdomain POD modes (in an ℓ_2 sense).

We recall the standard POD method that provides a set of orthonormal modes. If $\varphi_1, \varphi_2, \ldots, \varphi_N$ such that

$$\theta(x,t) = \sum_{i=1}^{N} a_i(t)\varphi_i(x) \tag{5.1}$$

where a_i are the temporal modes.

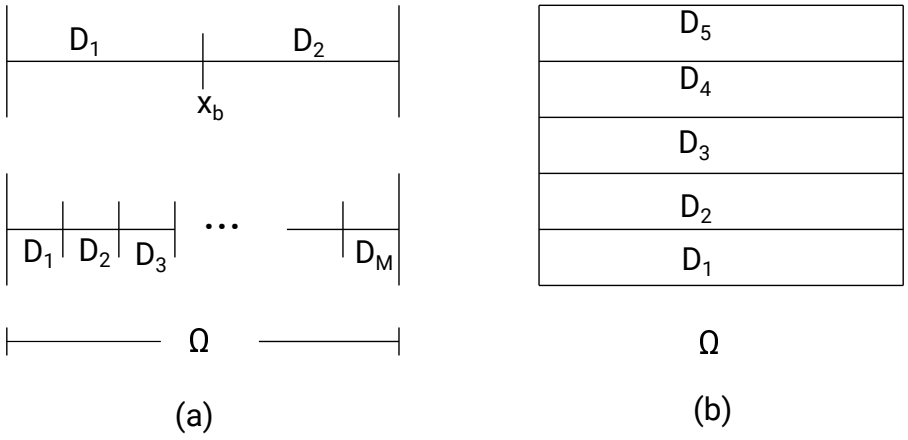

Figure 5.1: Typical domain decomposition for 1D domain(a), 2D domain (b).

For the subdomain POD method, the physical domain D will be divided into N_d subdomains such that $D = D_1 \cup D_2 \cup D_3 \cup \ldots D_{N_d}$ (figures 5.1(a,b)). We apply the standard POD within each subdomain. The POD modes for each subdomain D_j ψ_i^j, are the continuous functions defined on D_j such that $\left\langle \| \theta_j(x,t) - \sum_{i=1}^{N} b_i(t)\psi_i^j(x) \|^2 \right\rangle$ is minimum locally within and on D_j. The temporal coefficients, in this case, are obtained by projecting the modes $\psi_i^j(x)$ over the scalar field θ locally, that is,

$$b_i^j(t) = \Big(\theta(x,t), \psi_i^j(x)\Big)_{D_j} = \int_{D_j} \theta(x,t)\psi_i^j(x)dx \tag{5.2}$$

for $i = 1, 2, \ldots, N$ and $j = 1, 2, \ldots, N_d$. Within each subdomain D_j, the scalar field has the decomposition of the form

$$\theta(x,t) = \sum_{i=1}^{N} b_i^j(t)\psi_i^j(x) \tag{5.3}$$

The POD modes ψ_i^j obtained within each subdomain D_j may be termed as subdomain POD modes. These subdomain POD modes are different from standard POD modes φ_i. Standard POD modes are the global optimum functions over the physical domain that represent the

scalar field θ, whereas subdomain POD modes are only locally optimum functions within and on each subdomain.

5.1.1 Properties of the subdomain POD modes

The computational cost of the subdomain POD modes increases with the number of subdomains. Since the computational cost of computing eigenvectors (the method of snapshots) depends only on the number of snapshots, the computational cost for the subdomain method increased by a factor equal to the number of subdomains. On the other hand, the subdomain method does not need include the whole domain for reconstructions of a local flow that significantly reduces the degrees of freedom.

The subdomain POD modes inherits orthogonality from the POD method. The subdomain POD modes obtained in each subdomain are orthogonal within the corresponding subdomain.

The continuity at the subdomain boundaries does not follow automatically for the subdomain POD method. In the current analysis, a transformation consisting of a spatially dependent background field is used to ensure continuity. The details of the transformation for a $1D$ domain decomposition is presented in the next section 5.1.2.

5.1.2 Background field

The representation of a field as a combination of subdomain POD modes ensures optimality only in the ℓ_2-sense in each subdomain and the reconstructed field from subdomain POD modes is not necessarily continuous at the subdomain boundaries. To address this problem, we introduce a background field. Let us assume θ be a scalar defined in a 1D domain and the domain is subdivided into subdomains $[x_1 \quad x_2]$, $[x_2 \quad x_3]$, $[x_3 \quad x_4] \ldots [x_{n-1} \quad x_n]$. Let us assume θ is known at the subdomain boundaries. We define a background field as

$$\theta_b^j(x,t) = \Big(\frac{x - x_j}{l_j}\Big)\theta^j(x_{j+1},t) + \Big(\frac{x_{j+1} - x}{l_j}\Big)\theta^j(x_j,t) \tag{5.4}$$

Here, θ^j is θ within $[x_j \quad x_{j+1}]$, θ_b^j is the background field in $[x_j \quad x_{j+1}]$, x_j are the boundaries of the subdomains and $l_j = x_{j+1} - x_j$ are the lengths of the intervals. This background field is required boundary information at prior. Now, a transformation is defined as

$$\Theta_b^j(x,t) = \theta^j(x,t) - \theta_b^j(x,t) \tag{5.5}$$

The transformed field Θ^j vanishes at the boundaries. Now, let us recall that a scalar can be expressed as a linear combination of its subdomain POD modes within a subdomain. That is, at the boundary $x = x_j$,

$$0 = \Theta^j(x_j,t) = \sum_{i=1}^{N} b_i^j(t)\psi_i^j(x_j,t) \tag{5.6}$$

The modes ψ_i^j are orthogonal to each other and thus form a linearly independent set of functions. Then, from elementary linear algebra,

$$\psi_i^j(x_i,t) = 0 \tag{5.7}$$

That is, all the subdomain POD modes of Θ^j vanishes at the boundary and the reconstructed Θ^j obtained from a combination of the subdomain POD modes will also satisfy vanishing boundary conditions. Thus the continuity at subdomain boundaries will be satisfied trivially.

Since θ_b^j is a spatially distributed function and the correlation functions of the Θ^j and θ^j fields are different, the subdomain POD modes of θ^j are different from that of the Θ^j field. But, once the Θ^j field is reconstructed from the subdomain POD modes of Θ^j, this reconstructed Θ^j field can be transformed back to the θ^j field using the background field θ_b^j as

$$\theta^j(x) = \Theta^j(x) + \theta_b^j(x) \tag{5.8}$$

It is to be noted that, to use background field the scalar at the boundaries $\theta^j(x_i,t)$ must be available *a priori*.

5.1.3 Subdomain decomposition for a gappy field

We consider, a domain D partitioned into M subdomains $D_1, D_2, \ldots, D_{N_m}$. As in the standard gappy case, mask functions are defined for $j = 1, 2, \ldots, N_M$ as

$$m(x) = \begin{cases} 1 & \text{if information is available} \\ 0 & \text{elsewhere} \end{cases}$$

As for the standard POD technique (section 4.3) within each subdomain D_j, we need to solve a linear system of equations,

$$M^j \widetilde{b^j} = f^j \tag{5.9}$$

for $j = 1, 2, \ldots, N_M$. Here, $\widetilde{\psi}_k^j = m(x)\psi_k^j(x)$, $M_{ik}^j = \int_{D_j} \widetilde{\psi}_k^j(x)\widetilde{\psi}_i^j(x)\,dx$, $f_k^j = \int_{D_j} \widetilde{\psi}_k^j(x)\widetilde{\theta}(x,t)\,dx$. After solving N_M systems of linear equations in 5.9, the entire field can be obtained using the equations 5.3 .

5.2 Application to the KS equation

We will now evaluate and apply the subdomain POD modes to reconstruct the KS dynamics. Recall that, the one dimensional Kuramoto-Sivashinsky (KS) equation can be presented in normalized form as [Papageorgiou, 1991],

$$\frac{\partial u}{\partial t} + u\frac{\partial u}{\partial x} + \frac{\partial^2 u}{\partial x^2} + \nu\frac{\partial^4 u}{\partial x^4} = 0 \tag{5.10}$$

with $u(x,0) = -\sin(x)$ and $u(x+2\pi,t) = u(x,t)$. The parameter ν is the viscosity. To start with the subdomain POD method, a domain decomposition strategy consists of two subdomains is considered. As shown in the figure 5.2a, these two subdomains are $D_1 : x \in [0,\pi]$ and $D_2 : x \in [\pi, 2\pi]$ respectively. Within each subdomain, u is no longer periodic and thus subdomain POD modes are not necessarily the Fourier modes.

To satisfy continuity at subdomain boundaries, a background field is introduced such that

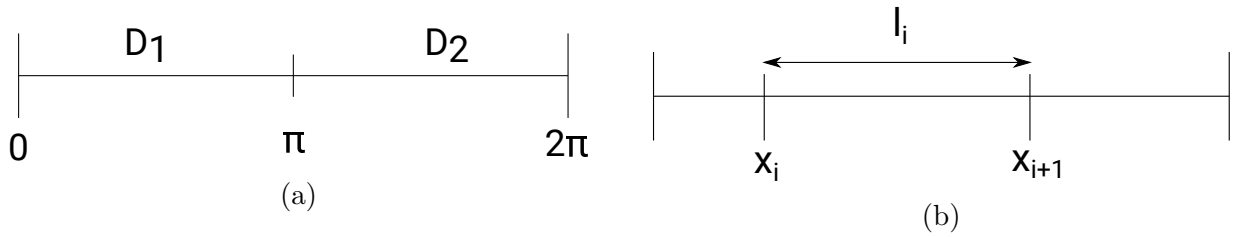

Figure 5.2: Domain decomposition strategy with two subdomain (a), transformation of the u field; assuming u is known at the boundaries x_i (b).

$$u_b(x) = \Big(\frac{x - x_i}{l_i}\Big)u(x_{i+1}) + \Big(\frac{x_{i+1} - x}{l_i}\Big)u(x_i) \tag{5.11}$$

where, x_i and x_{i+1} be the boundaries of a subdomain and since, the subdomains are chosen to be of equal length, so $l_i = \pi$ is the length of the subdomain for all i (figure 5.2b). We note that u is known a priory at the boundary points $x = 0$, π and 2π. Now, we define a transformation as

$$U_b(x) = u(x) - u_b(x) \tag{5.12}$$

From the above definition of u_b, U_b vanishes on the both boundaries. Once each snapshots are transformed as the equation 5.12, the subdomain POD modes are evaluated and the resulted modes also satisfy the vanishing boundary conditions. Once the U_b field is reconstructed from the subdomain POD modes of U, this reconstructed U_b field can be transformed back to the u field using the background field u_b as

$$u(x) = U(x) + u_b(x) \tag{5.13}$$

From the eigenvalue spectrum (figure 5.3a) of the subdomain POD modes of U (within each subdomain), the number of the subdomain POD modes is 48, corresponding to nonzero eigenvalues (eigenvalues $< 10^{-6}$ are ignored). Then, the subdomain POD modes are computed from the 800 snapshots and denoted as $\left(\psi_i^j\right)^{800}$ for $j = 1, 2$. Next, 200 more snapshots are added to the previous 800 snapshots and subdomain POD modes are computed again as $\left(\psi_i^j\right)^{1000}$. If the both

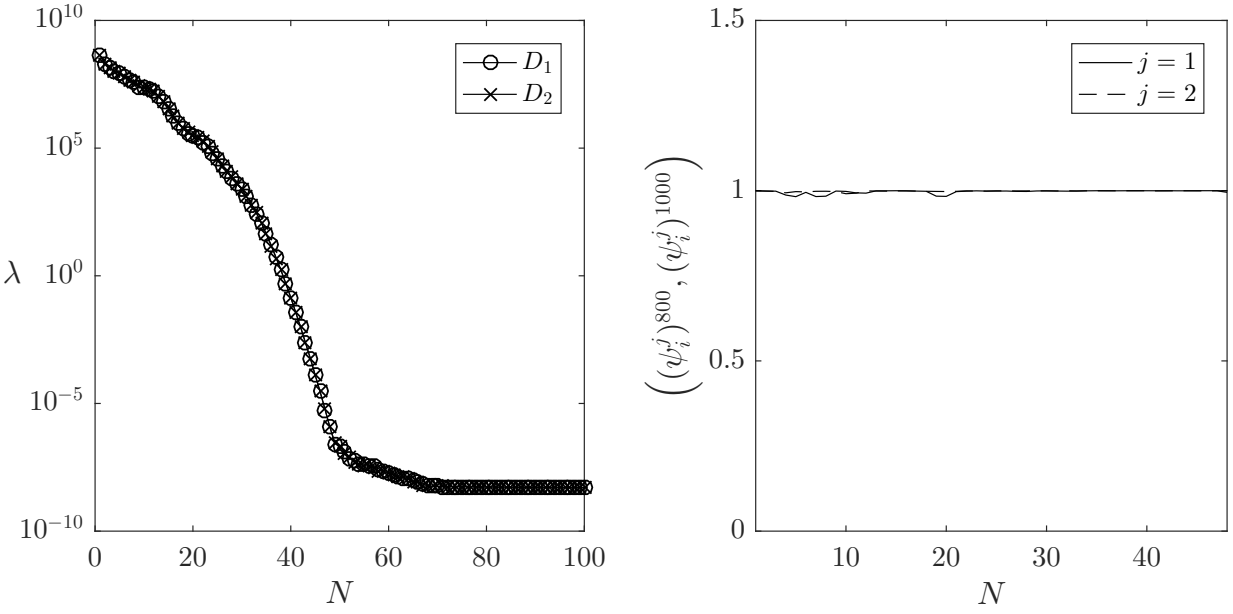

(a) (b)

Figure 5.3: (a) Eigenvalue spectrum of the subdomain POD modes for 2 subdomains D_1 and D_2, (b) orthogonality of $\left(\psi_i^j\right)^{800}$ and $\left(\psi_i^j\right)^{1000}$ implying that a data-set of 800 snapshots are sufficient to extract the POD modes.

sets of modes are same then from the orthonormality of the modes, $\left(\left(\psi_i^j\right)^{800}, \left(\psi_i\right)^{1000}\right) = 1$, which is satisfied as shown in the figure 5.3b. That is, these 800 snapshots are sufficient to obtain the convergence. The temporal modes $b_i^j(t)$ are then computed from the converged modes using the equation 5.2. The resulting U field, obtained as the combination of subdomain POD modes, is transformed to the u field using the equation 5.13. The reconstructed u field and the sample snapshot is shown in the figure 5.4. Here, the measure of performance γ of the reconstructed field is of 10^{-8}. Recall that, the measure of performance γ is defined as

$$\gamma = \sqrt{\int_0^{2\pi} \int_0^T (u - u_r)^2 \, dt \, dx} \Big/ \sqrt{\int_0^{2\pi} \int_0^T u^2 \, dt \, dx} \tag{5.14}$$

where, u_r is the reconstructed u using standard or subdomain POD method.

We will now consider the gappy problem discussed in the previous chapter (section 4.3.1). We suppose for each subdomains, there are 33 equidistant grid points where information are available. Thus the ratio $p = 0.5$, is same as the standard POD case (p is defined as equation

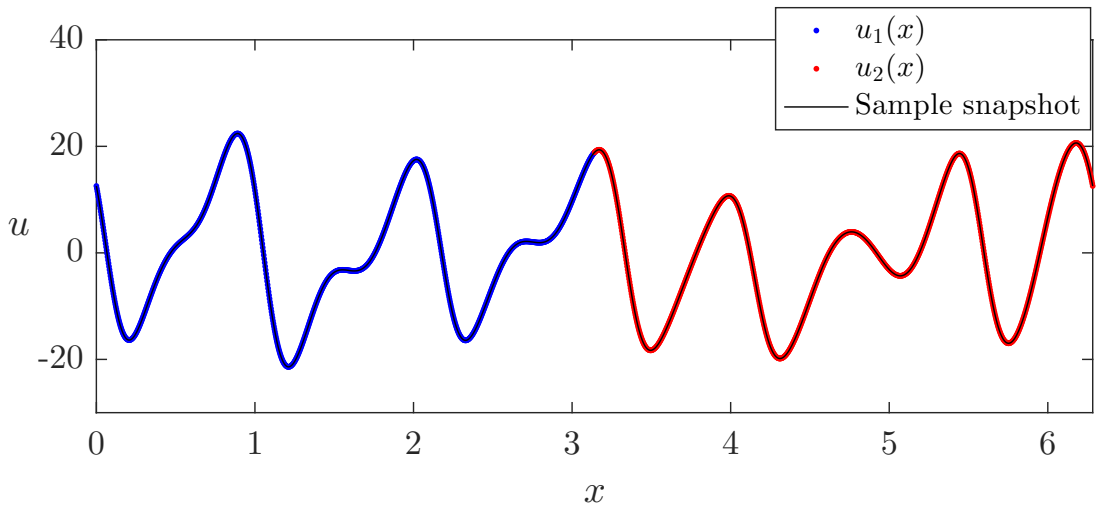

Figure 5.4: Reconstruction of the sample snapshot using $2 \times 48 = 96$ subdomain POD modes. The reconstruction is carried out using two subdomains as in figure 5.2a.

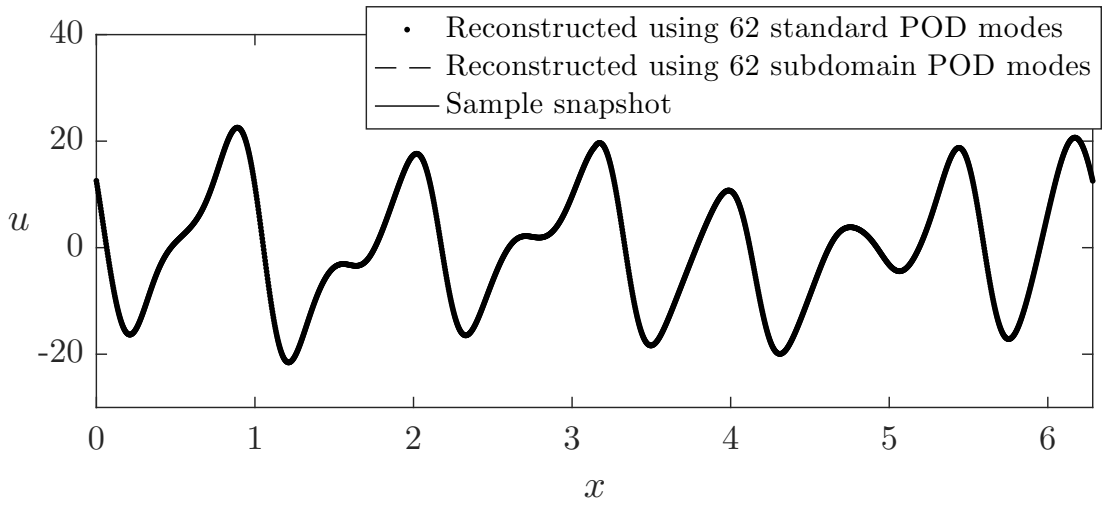

Figure 5.5: Comparison of the reconstructed snapshot using the standard POD method and the subdomain POD method (using 2 subdomains) of the sample snapshot.

4.30).

The subdomain POD modes, obtained earlier, are then used to compute the temporal coefficients $b_i^j(t)$ using the equation 5.9 and finally, the solution is reconstructed using equation 5.3. The reconstructed fields for the both cases are shown with the actual sample snapshot in figure 5.5. Also, the reconstruction using 2 subdomains in xt- plane is shown in figure 5.6.

Figure 5.7 shows the performance parameter γ of both standard POD and subdomain POD with 2 subdomains for different values of p. It is clear from 5.7(a,b) that, for a certain p, the trends of γ for both methods are similar and γ diverges around the same values of N, where N

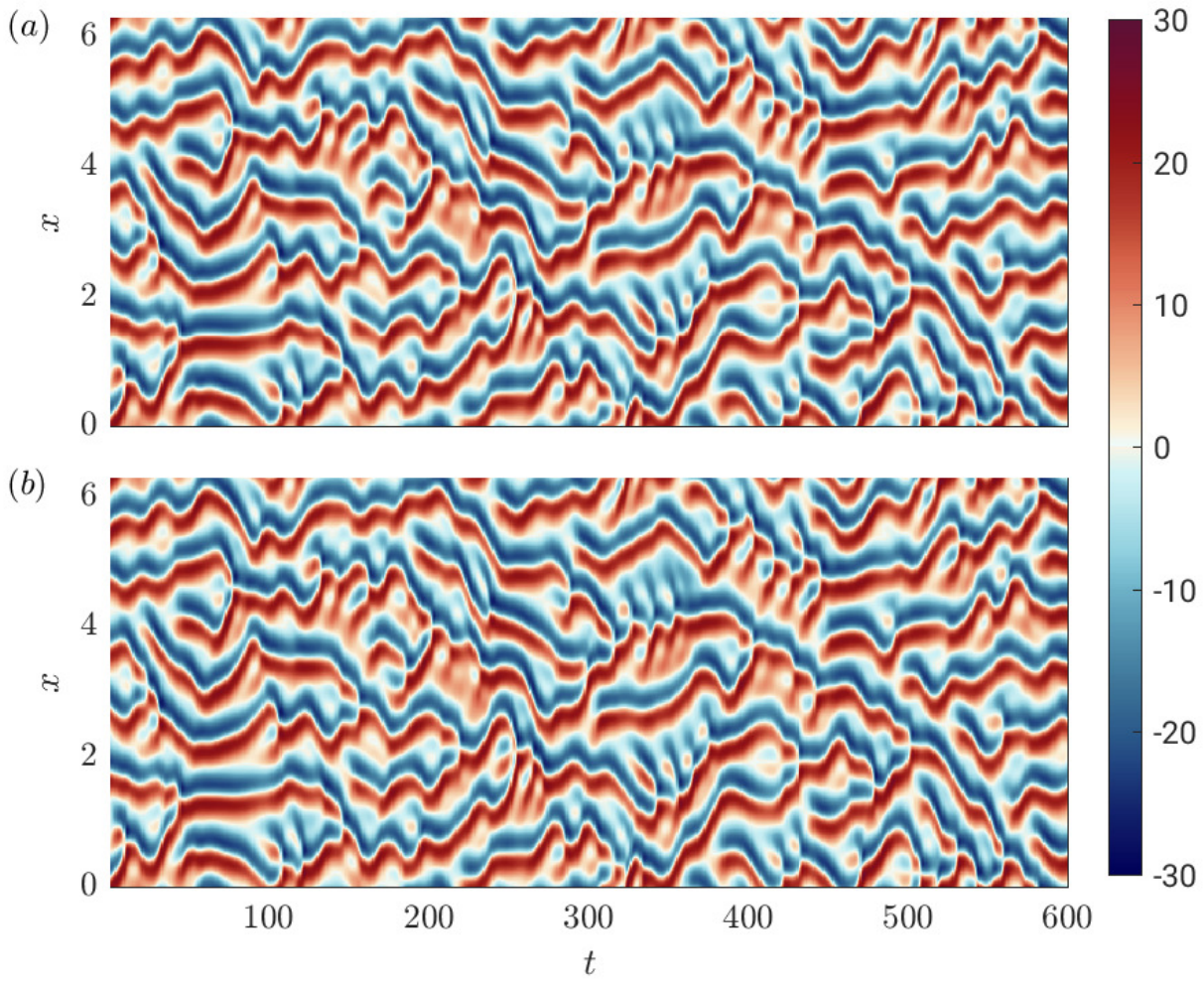

Figure 5.6: (a) KS solution in x-t plane and (b) reconstruction of KS solution using $2 \times 31 = 62$ subdomain POD modes. Here, the parameters are $\nu = 0.01$ and $p = 0.0317$.

represents the number of the modes used for reconstruction. That is, the reconstructions using standard POD and subdomain POD are comparable.

We computed γ for the background fields for both subdomains as 1.28 and 1.31, respectively. This implies, the introduction of background fields does not bias the reconstruction.

5.3 Application to plane Couette flow

In this section, We will apply subdomain POD method to reconstruct the streamwise component u of plane Couette flow. We will also analyse the performance of subdomain POD modes for different values of p and consequently compare with standard POD modes. As in the case

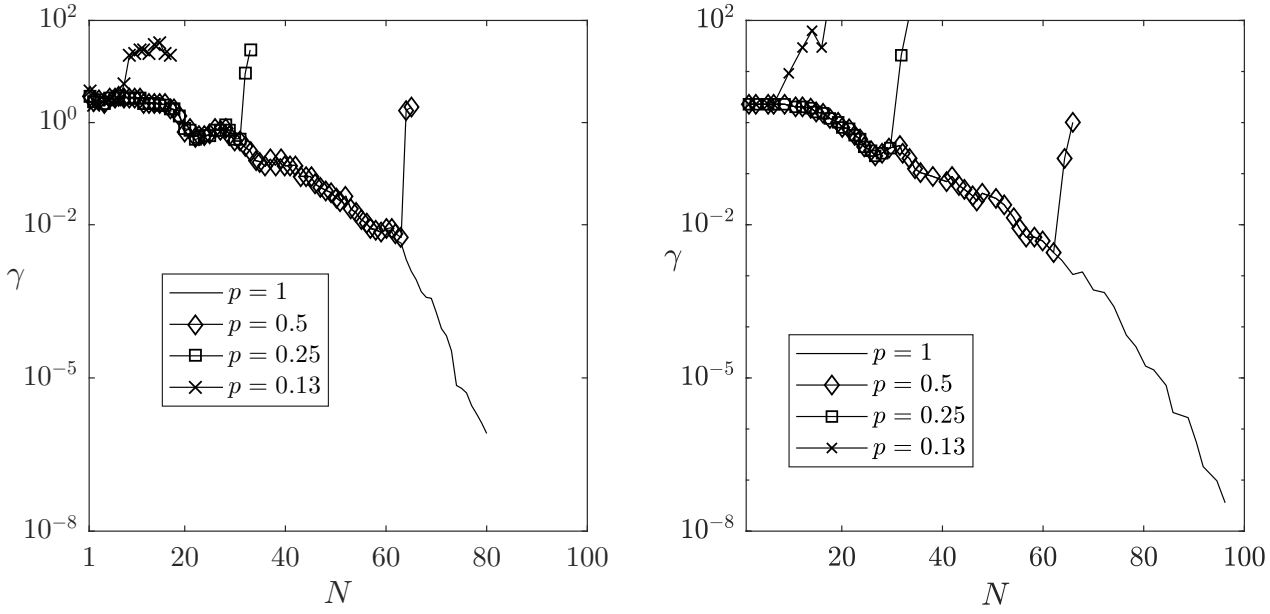

Figure 5.7: (a) Relative error of the reconstructed snapshots for $p = 1$, 0.5, 0.25 and $p = 0.13$ using the standard POD modes and (b) the subdomain POD modes.

of standard POD method (section 4.2.4), we will restrict reconstruction to the yz-plane only, where y and z are the spanwise and the wall normal direction respectively. Here, the $2D$ domain is decomposed into 2 subdomains, sliced horizontally (as in the figure 5.1(b)).

Similar to the POD method, the state variable in the yz-plane can be expressed as the linear combination of the POD modes for $j = 1$ and 2, [Moehlis et al., 2002]

$$\mathbf{s^j}(\mathbf{x}, t) = \sum_{n} \sum_{n_y=-N_y}^{N_y} a^j_{nn_y}(t) \hat{\boldsymbol{\psi}}^j_{nn_y}(\mathbf{x}) \exp\left(i \frac{2\pi n_y y}{L_y}\right) \tag{5.15}$$

Here, $\mathbf{x} = (y, z)^T$ is the coordinates, $\mathbf{s^j} = (u, \theta_w)^T$ is the state variable within domain D_j, u is the streamwise velocity component and θ_w is the wall temperature, n_y is the spanwise wavenumber, $a^j_{nn_y}$ and $\hat{\boldsymbol{\psi}}^j_{nn_y}$ are the temporal coefficients and the subdomain POD modes in wall normal direction respectively, L_y is the length in the spanwise direction. Since, $\mathbf{s^j}$ is vector-valued, $\hat{\boldsymbol{\psi}}^j_{nn_y}$ are also vector-valued with components $\hat{\psi}^j_{nn_y,\theta_w}$ and $\hat{\psi}^j_{nn_y,u}$, corresponding to θ_w and u, respectively. $\hat{\boldsymbol{\psi}}^j_{nn_y}$ is the n-th POD mode in subdomain j corresponding to wavenumber n_y.

The continuity along the boundaries of the subdomain is prescribed through the background method, as introduced in the reconstruction of the KS equation solution. The background field for the $2D$ plane is defined as

$$\mathbf{s^j}_b(x,z) = \Big(\frac{z-z_i}{h_i}\Big)\mathbf{s^j}(x,z_{i+1}) + \Big(\frac{z_{i+1}-z}{h_i}\Big)\mathbf{s^j}(x,z_i) \tag{5.16}$$

where, $h_i = z_{i+1} - z_i$ is height of the subdomain, measured in the wall normal direction and let $h_i = H$ for all i. Similar to the KS solution case, a transformation is defined as

$$\mathbf{S}^j = \mathbf{s^j} - \mathbf{s^j}_b \tag{5.17}$$

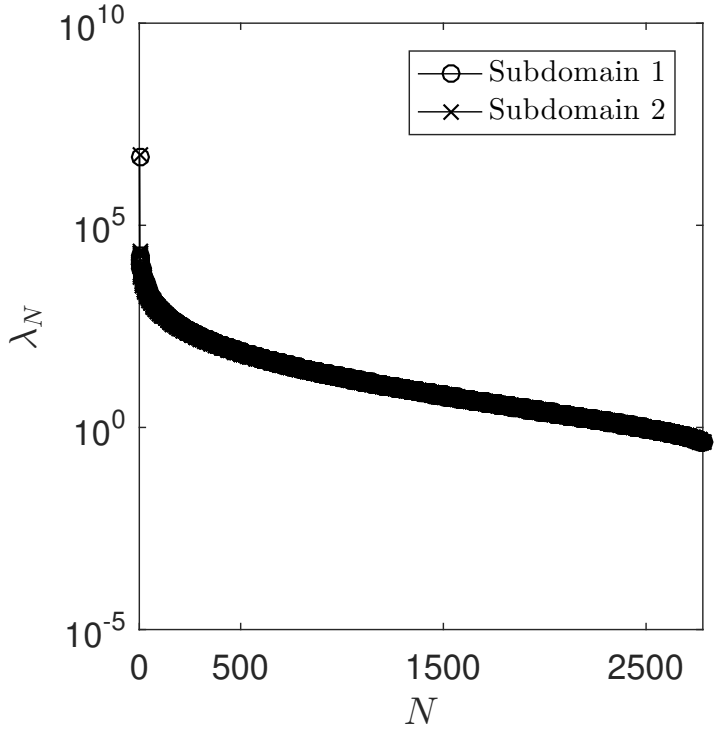

Figure 5.8: The eigenvalue spectrum the subdomain POD modes.

To evaluate subdomain POD modes we obtain an ensemble of total 5600 DNS snapshots 2 of the state variable $\mathbf{s^j} = (u, \theta_w)^T$ on the yz–plane at $x^+ = 526$. We apply the method of snapshots at each subdomain to evaluate the modes of S^j and plotted in figure 5.8 is the eigenvalue spectrum of the modes and the spectrum of the modes for both subdomains coincide. Since the mean and second order statistics are symmetric about the channel mid-height, the eigenvalue spectrum

of two subdomains should coincide. Similar to the POD modes, the spectrum of subdomain modes does not vanish for large N ($N < 2500$).

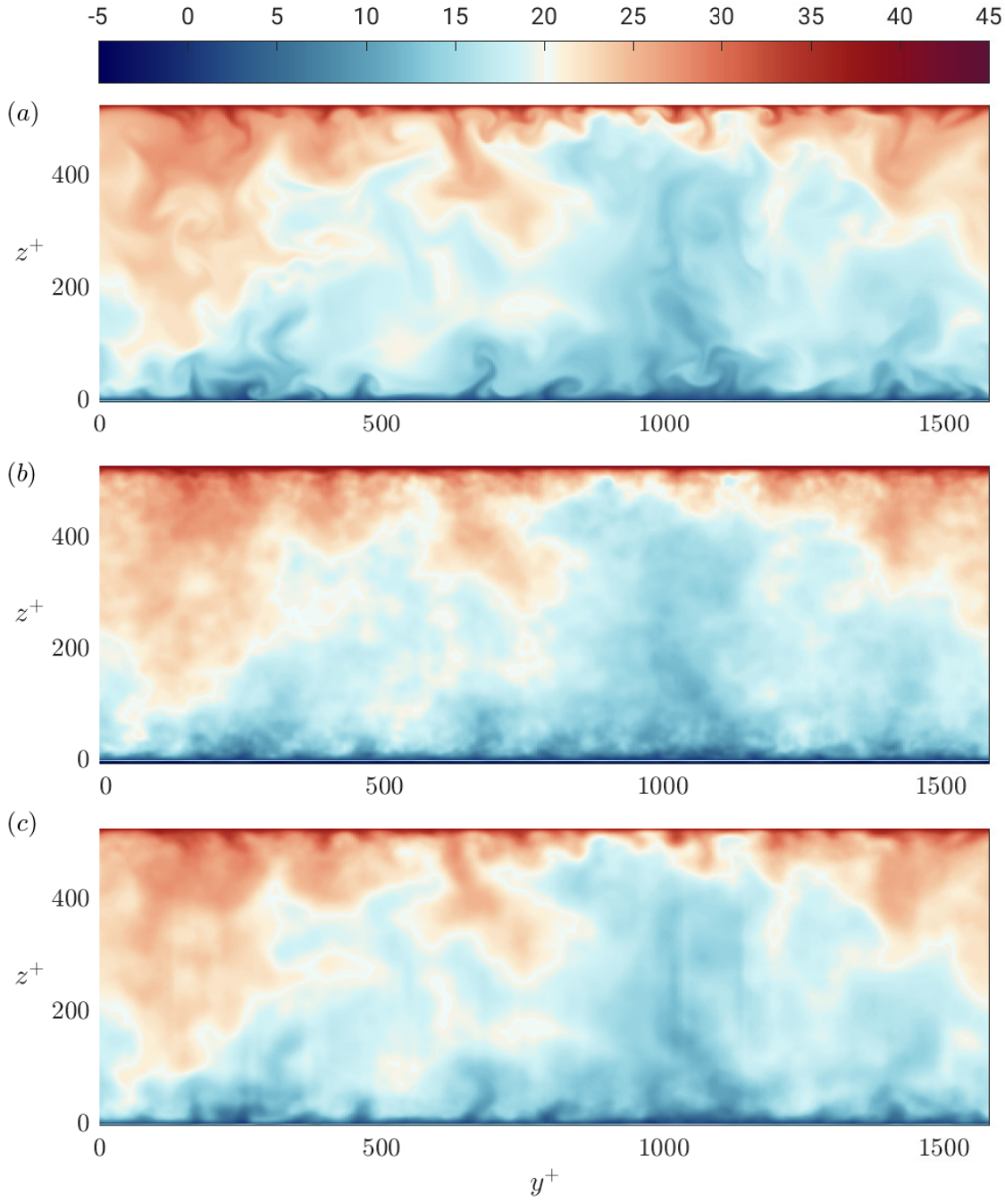

Figure 5.9: A sample snapshot of streamwise velocity component u field obtained from DNS (a), reconstructed field using 500 POD modes (b) and $2 \times 250 = 500$ subdomain POD modes (c). Here, the ratio $p = 1$.

Once the actual snapshot has been translated by the background field, the translated snapshot

is reconstructed using the subdomain POD modes. The background field is then added to the reconstructed translated snapshot to obtain the reconstruction for the actual snapshot. The reconstructed sample snapshot using $2 \times 250 = 500$ modes are shown in the figure 5.9. For comparison purposes, we also reproduce the reconstructed snapshot using 500 standard POD modes. Visual inspection of figures 5.9(a-c) confirms that both the methods yields good reconstruction of the actual snapshot. The measure of performance for both cases are almost same as $\gamma = 0.03$. As for the flow structures, the reconstruction using the subdomain POD modes is a better fit compare to the POD modes. The locally optimised subdomain POD modes reconstruct the peaks better which the standard POD modes fail to reproduce.

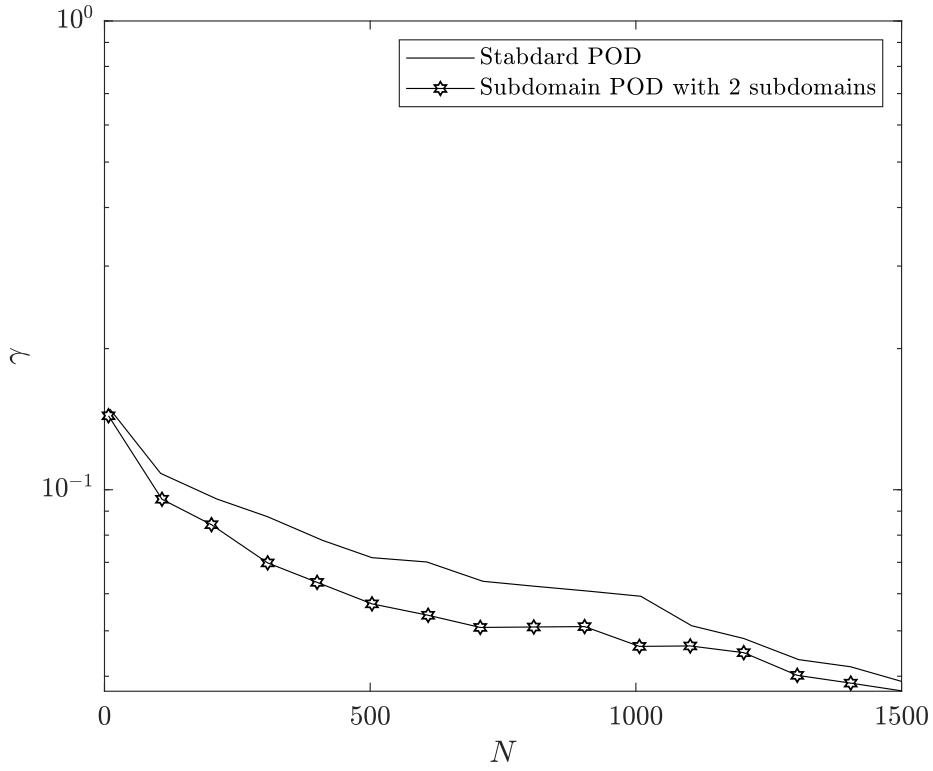

Figure 5.10: The comparison of the relative norm using the standard and the subdomain POD modes (using the background field approach).

The measure γ of the reconstruction using the standard and the subdomain POD modes are shown in the figure 5.10. As seen in the KS equation case; in the plane Couette flow, the performance of the subdomain POD modes are found to be similar to the standard POD modes.

Next, a gappy field is considered by sampling the sample snapshot 5.9(a) in the z (wall normal)

direction. From the actual resolution of the sample snapshot 432×432, only the resolution 432×25 is assumed to be known; the rest of the pixels are to be reconstructed. The sampled z planes, starting from the plane $z = 0$ (the bottom wall) and moving upwards, are chosen equidistant to each other and there is no sampling considered in the y (spanwise) direction. Therefore, the ratio of the available information to the total resolution, $p \approx 0.046$.

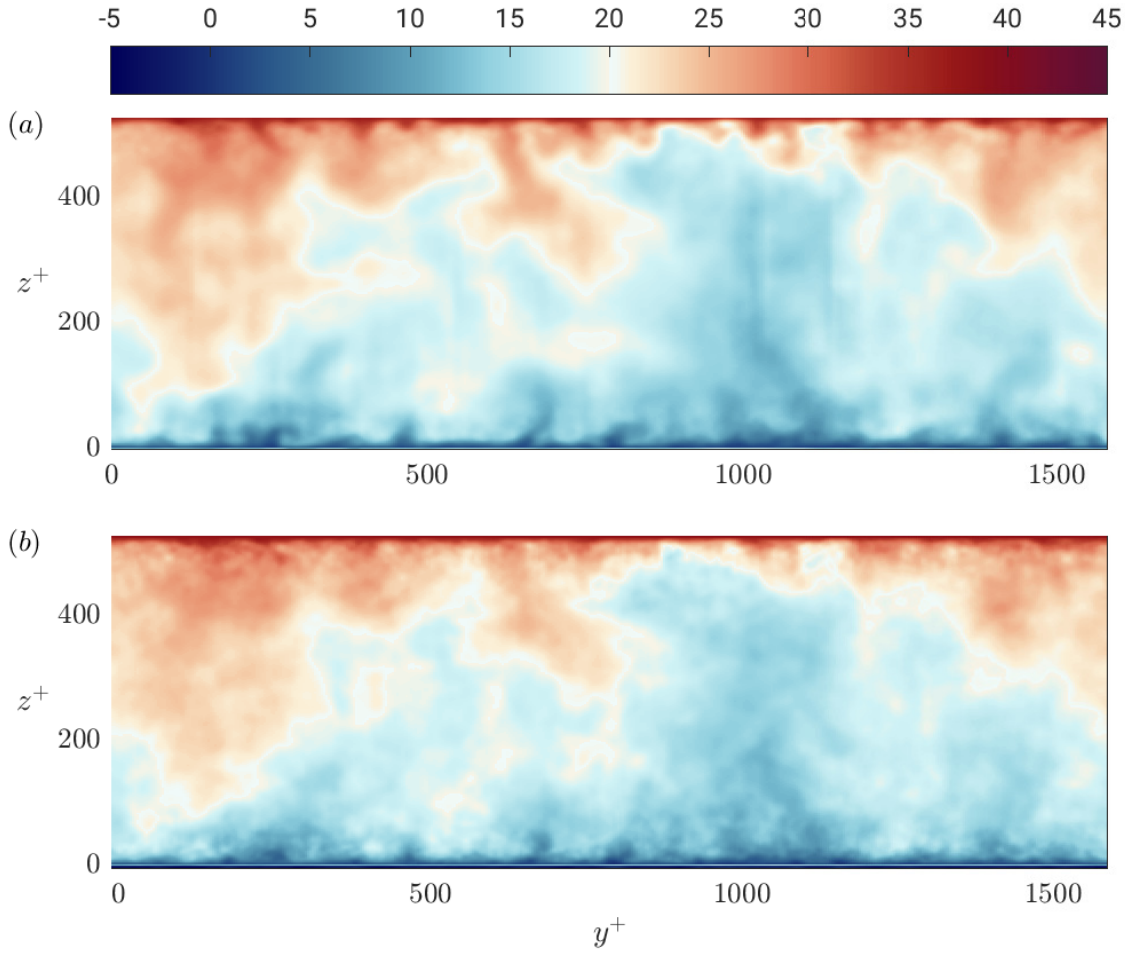

Figure 5.11: Reconstructed streamwise velocity component u with $2 \times 250 = 500$ subdomain POD modes (a), and 500 standard POD modes (b). In both cases only 4.6% pixel information are used, that is $p = 0.046$.

The reconstructed field using $2 \times 250 = 500$ subdomain POD modes is computed using equations (5.9) and (5.3), and presented in the figure 5.11(b) along with the reconstructed snapshot using 500 standard POD modes. Comparing the figures 5.11(a,b) the reconstruction ability from the partial information (here is only 4.6%) are sufficiently good by using both the standard and

the subdomain POD modes. The larger flow structures in both reconstructions are close to the actual DNS 5.9(a) whereas the subdomain POD method reconstruct the small scale flow structures better than the standard POD method. The peaks are more visible in figure 5.11(a) compared to figure figure 5.11(b).

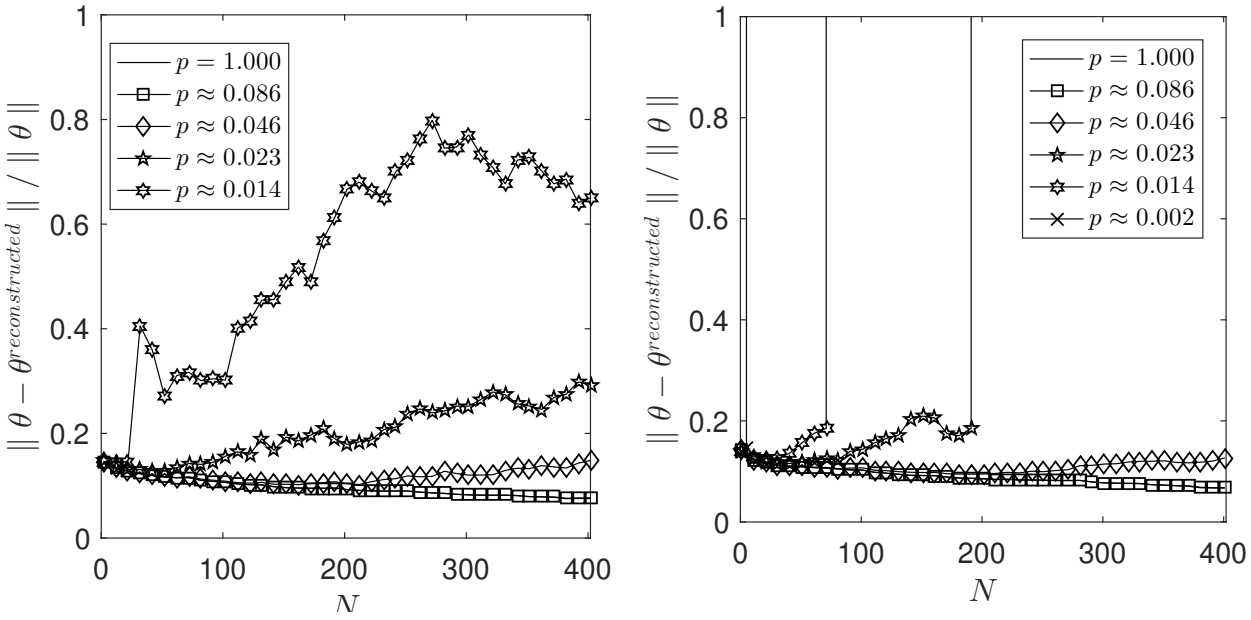

(a) (b)

Figure 5.12: The measure γ in the reconstructions of the streamwise velocity component using (a) the subdomain POD modes, (b) the standard POD modes. In figure (b), there is an extra curve corresponding to $p = 0.002$ that diverges for $N > 5$.

The final comparison of the two methods are presented as the ability to reconstruct the sample snapshot for varying values of the ratio p. While using the subdomain POD modes, the γ-curves for the case $p = 1$ and $p \approx 0.086$ coincide (figure 5.12a). That is, only 8.6% pixel information are enough to reproduce the full snapshot. On the other hand, any reconstruction process diverges for $N > 60$ if $p \leq 0.023$. The behavior of the standard POD γ-curves are found to be similar to that of the subdomain POD except for the fact that the standard POD γ-curves diverge more rapidly (figure 5.12b). The case with $p \approx 0.002$ in figure 5.12b corresponds to the limiting case when only the thermal field measurements are available at the bottom wall and the streamwise velocity component u is missing. In this particular case, the reconstruction process diverges if $N > 5$ and with the first 5 modes, one can only retrieve the mean thermal field along with a few smaller order fluctuations. Most importantly, the boundary layer structures can not

be obtained using the standard POD modes. This limiting case will be considered in the next example, where the subdomain POD modes will be used to extrapolate the streamwise velocity component u away from the bottom wall.

5.4 Extrapolation from the wall thermal imprints

In this section, the reconstruction ability of the subdomain POD modes will be assessed for $p = 0.002$, in a similar way as the standard POD case. This is the case where only wall temperature θ_w is available to reconstruct streamwise velocity component u. Since, no information about the velocity component u is available, we no longer can use the background field method. Recall that the background field was adopted to ensure continuity at the boundaries of the subdomains. Instead, we will adopt a strategy where the yz-plane will be subdivided horizontally into subdomains and the velocity within the first subdomain will be approximated from wall temperature. Since the second subdomain shares a common boundary with the first subdomain, the velocity at the bottom boundary of the second subdomain is available now and will be used to approximate the velocity within the second subdomain. This procedure of approximation will continue until the velocity within the last (top) subdomain is approximated.

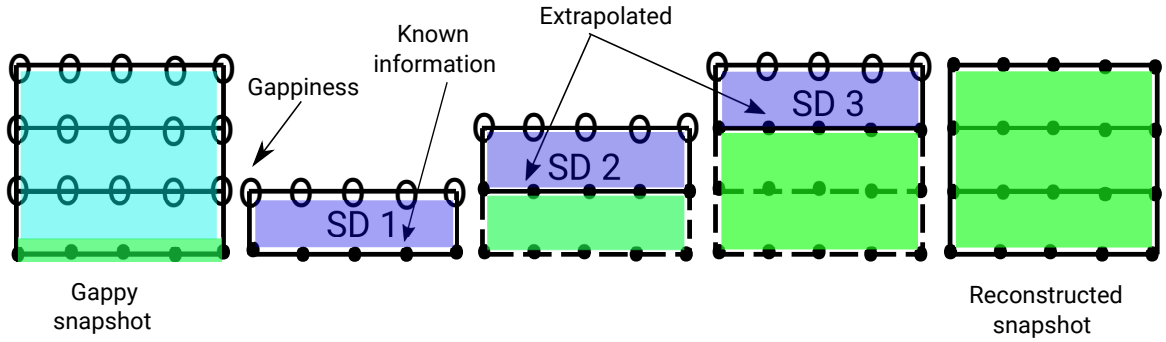

Figure 5.13: The reconstruction strategy using the subdomain POD modes for $j = 3$. The open circles represent the gappiness and the filled circles represent available/approximated quantity.

The domain decomposition and the repeated extrapolation procedure is shown in the figure 5.13 for $j = 3$. The above procedure is equivalent to the repeated application of any standard extrapolation method, except for the use of the subdomain POD modes as the extrapolating polynomials. The choice of this topology is also suitable from the fact that, the characteristics

of the turbulent eddies at any location are expected to be similar in the near vicinity. Also, in a boundary layer flow, the behaviour of the flow within boundary layer and outer layer are different.The procedure is described below in detail.

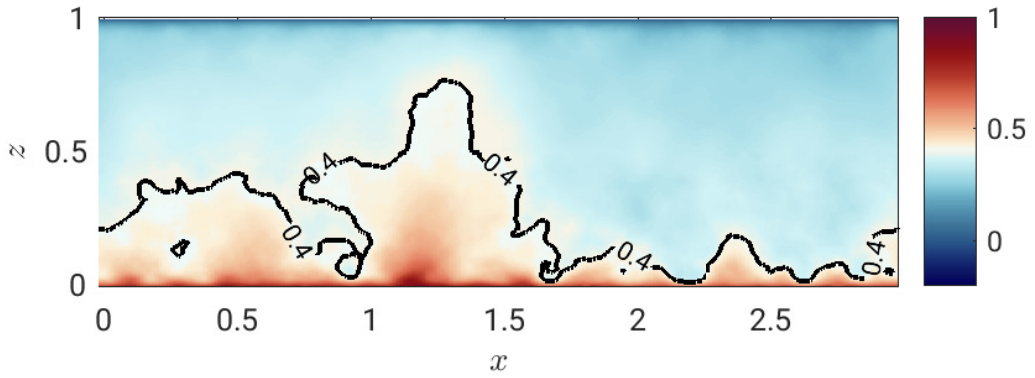

Figure 5.14: The reconstructed snapshot using the subdomain POD modes for $j = 2$.

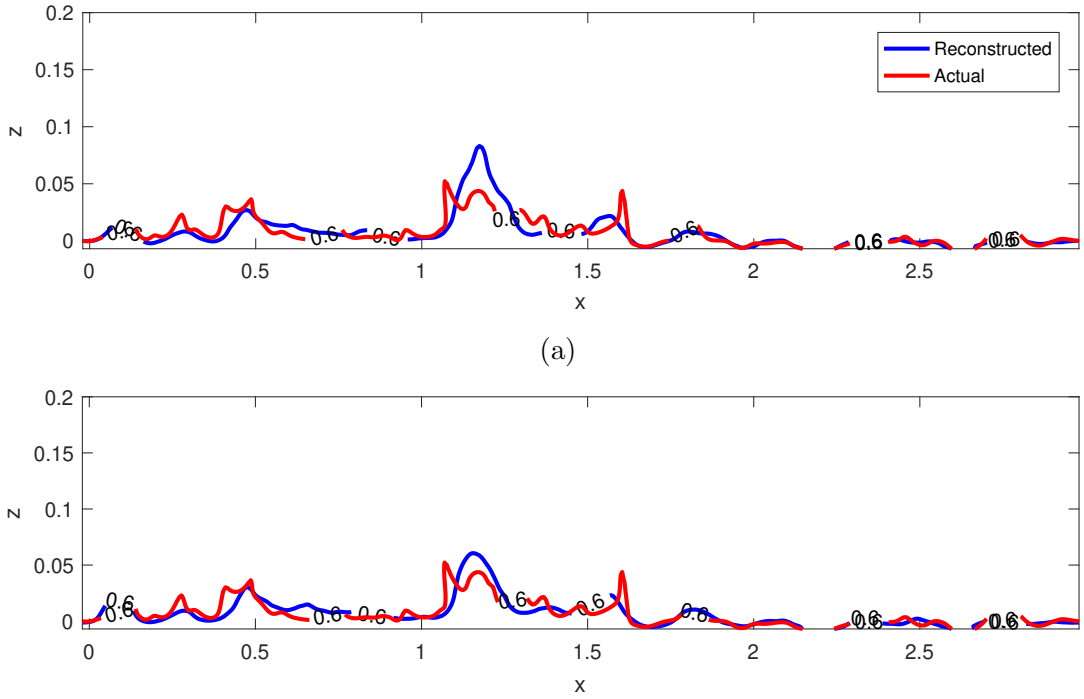

Figure 5.15: The reconstruction of the local structure using POD method (a) and subdomain POD method (b). The figure shows the contour $u = 0.6$ line that captures the near wall boundary layer structure.

First, a topology of the subdomain is chosen similar to the $2D$ example in figure 5.1(b), sliced horizontally. Since, the only available information are the observations at the bottom wall, the first subdomain is considered to be consists of the bottom wall. The subsequent procedures are

described as below

1. Divide the 2D domain into j subdomains.
2. Within the first subdomain, the known observations are the information (wall temperature) at the grid points of the bottom wall and the information at anywhere else is to be reconstructed using gappy POD method.
3. Since consecutive subdomains share a common boundary, the information at the bottom boundary of the second subdomain is available. The information at other grid points are to be reconstructed, as in step 2.
4. Repeat the procedure until the top wall of the 2D domain is reached.

The procedure described above is carried out with LASSO regularisation ($\lambda = 10^{-5}$) for two subdomains and the resulting snapshot is shown in figure 5.14. The measure γ of reconstructed snapshots is 0.245 which is comparable to the standard POD method. The reconstructed local structure using the subdomain POD is better than that of using the standard POD modes, as shown in the figure 5.15a and 5.15b. Since, subdomain modes are locally optimised modes, these modes can describe the local structures better than the reconstruction using standard POD modes.

5.5 Conclusions

We proposed a new decomposition — the subdomain POD method, where a physical domain is divided into subdomains and the POD method is applied within each subdomain separately. Subdomain POD modes inherit properties form POD modes such as boundary conditions, homogeneity and orthogonality within a subdomain. The subdomain POD modes obtained from each subdomain are orthogonal within the corresponding subdomain.

We used the same dynamical problems as in chapter 4 to test the performance of subdomain POD modes. These examples also allow us to compare the performance of subdomain POD

modes and standard POD modes. In first set of examples, 1D KS solutions were reconstructed for a range p values. We used a background field to ensure continuity at subdomain boundaries. background fields were chosen to obtain vanishing boundary conditions and the orthogonality of modes ensures the continuity at subdomain boundaries. We found the reconstructions using subdomain POD modes are as good as the reconstructions using POD modes for all p.

The second set of examples were reconstructions of the streamwise velocity components of plane Couette flow for a range of values of p. Once again, we found similar performances using subdomain and standard POD modes. For smaller p, reconstructions diverged around same values of N for both methods, where N is the number of modes used.

The tests using two sets of examples, namely 1D KS solution and plane Couette flow confirm that subdomain POD modes produce good reconstructions and comparable to those of standard POD modes.

We applied subdomain POD to reconstruction of streamwise velocity component of plane Couette flow using wall temperature only. We proposed a subdomain strategy (horizontally sliced) to pose the reconstruction problem as an extrapolation problem. Wall temperature at the bottom boundary were used to extrapolate velocity within and on the first (bottom) subdomain. Since, the consecutive subdomains share boundaries, we used the estimated velocity at the top boundary of the first subdomain to extrapolate velocity within and on second (top) subdomain. The measure of performance γ for reconstructions was found 0.245. Recall that, we applied standard POD for this reconstruction in chapter 4 with $\gamma = 0.24$. Another important feature of the reconstructions using subdomain POD is that of the reconstruction of local structures. This is due to the fact that subdomain POD modes are locally optimised.

The idea of subdomain POD was motivated by the characteristics of boundary layer flows where the flow at the boundary layer are different from the rest of the flow. Such local characteristics can also found elsewhere, such as flow with obstacles [Podvin et al., 2006, Xiao, 2016]. In such cases, the flow at corners are dynamically important but energetically insignificant [Schmid, 2010]. The Subdomain POD method is suitable for reconstructing such local flows for two reasons. First, subdomain POD modes are locally optimised. We can choose subdomains care-

fully around the local flow of interest. Second, we can reduce degrees of freedom significantly by choosing suitable subdomain topology within the global domain. Future work should incorporate appropriate boundary conditions for truncated domains of interest and an optimal strategy to find the topology of subdomains.

Chapter 6

Estimating flow using linear estimation theory

In this chapter, we will apply linear estimation theory to estimate flow velocity from wall temperature. In previous chapters, we used data-driven modal decomposition methods which do not need to consider the physics of the flow explicitly, although the resulting modes inherit the physics within. Thus an inclusion of a dynamical model enables us to impose a physical constraint and allows to assimilate wall temperature as input - which is still a data-driven approach. We will use the Orr-Sommerfeld-Squire system [Illingworth et al., 2018] and the non-linear terms in fluctuations will be considered as a time-dependent random forcing with zero mean and finite variance. We tested numerical routines for the operators used in Orr-Sommerfeld-Squire system with suitable examples and eigenvalue spectrum. We also deduce a transport equation for scalar fluctuation θ'' in the Fourier space which along with Orr-Sommerfeld-Squire system will form the dynamical model. In this model, the wall temperature is the input which will be used to tune the model parameters and to estimate the flow velocity. we design a problem with random disturbances to test the model and then finally proceed to estimate flow velocity using the DNS wall temperature.

6.1 State-space description

The state-space description of a dynamical system can be represented as,

$$\frac{d\mathbf{x}(t)}{dt} = A\mathbf{x}(t) + B\mathbf{d}(t) + F\mathbf{r}(t) \tag{6.1a}$$

$$\mathbf{y}(t) = C_y\mathbf{x}(t) + \mathbf{v}(t) \tag{6.1b}$$

where, A is the system matrix, B is the forcing matrix, F is the input matrix, $\mathbf{x}(t)$ is the state vector, $\mathbf{d}(t)$ model uncertainty and $\mathbf{r}(t)$ is due to physical controls (actuators). If there is no actuator to control the system then $\mathbf{r}(t) = \mathbf{0}$. similarly, for a perfect model without any uncertainty, $\mathbf{d}(t) = \mathbf{0}$.

The equation (6.1b) represents the measurements from the sensors. The operator C_y projects the physical domain into the measurement space. If the measurements are available for the whole domain then $C_y = I$, where, I is the identity matrix. The vector $\mathbf{v}(t)$ is the measurement noise, assumed to be a Gaussian white noise with zero mean and finite variance.

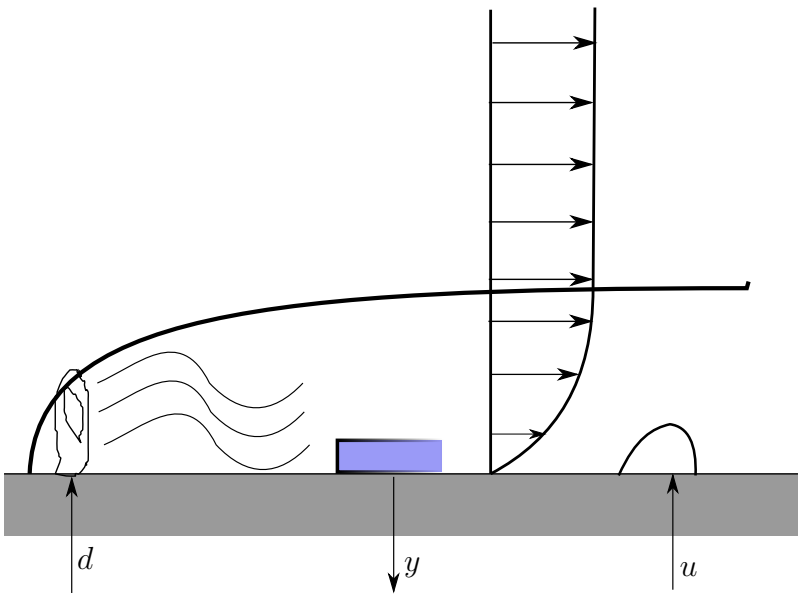

Figure 6.1: A schematic diagram of a boundary layer over a flat plate [Hoepffner, 2006].

An example of such model is a boundary layer flow (Figure: 6.1) with two types of inputs: $\mathbf{d}(t)$ be a upstream volume force which generate waves that propagate and grow along the stream

and $\mathbf{r}(t)$ is a distribution of blowing/suction on the wall [Hoepffner, 2006]. Here, the input $\mathbf{r}(t)$ is an actuator for control whereas $\mathbf{d}(t)$ is a generic flow characteristic (non-linear perturbation feedback). The measurements $\mathbf{y}(t)$ can be the wall shear stress.

6.2 Estimation problem

The estimation problem deals with the estimation of the state $\mathbf{x}$ from the partial sensor measurements. To build up a framework for the estimation problem, the dynamics of the estimated state are described as [Trentelman et al., 2002, Murray, 2006]

$$\frac{d\mathbf{x}_e(t)}{dt} = A\mathbf{x}_e(t) + B\mathbf{d}(t) + F\mathbf{r}(\mathbf{t}) - K(\mathbf{y} - C_y\mathbf{x}_e) \tag{6.2}$$

That is, $\mathbf{x}_e$ follows the same dynamical laws (6.1), except for the the last term $-K(\mathbf{y} - C_y\mathbf{x}_e)$, where K is the observer gain. Starting from an arbitrary initial state, this last term drives the estimated state $\mathbf{x}_e$ to the state of the system, $\mathbf{x}$. Now, if $\tilde{\mathbf{x}} = \mathbf{x} - \mathbf{x}_e$ denotes the error in the estimation, then the dynamics of $\tilde{\mathbf{x}}$ can be evaluated from (6.1a) and (6.2), and assuming $\mathbf{v} = \mathbf{0}$,

$$\begin{aligned} \frac{d\tilde{\mathbf{x}}(t)}{dt} &= A\tilde{x} + K(\mathbf{y} - C_y\mathbf{x}_e) \\ &= A\tilde{x} + K(C_y\mathbf{x} - C_y\mathbf{x}_e) \\ &= (A + KC_y)\tilde{\mathbf{x}} \end{aligned} \tag{6.3}$$

Thus the optimal choice for K will stabilise the error $\tilde{\mathbf{x}}$, which, in turn ensures $\mathbf{x}_e$ to be a good estimate for the actual state $\mathbf{x}$. The optimal K, is therefore, minimize the cost,

$$J_E(\mathbf{x}_e) = \int_0^\infty \| \mathbf{y} - C_y\mathbf{x}_e \|_2 \, dt \tag{6.4}$$

where, $\| \, . \, \|_2$ represents the ℓ_2 norm.

Let us assume that P be the covariance matrix of the estimation error $\tilde{\mathbf{x}}$. It can be shown that P is a solution of the Lyapunov equation Kim2007

$$(A + KC)P + P(A + KC)^* + KQ_vK^* + BQ_dB^* = 0 \tag{6.5}$$

To obtain optimal K, we set a minimisation problem to minimise the variance of the estimation error. That is

$$J = \mathrm{Tr}(PQ) \tag{6.6}$$

Here, Q is a weight matrix. We want to minimise the objective function J subject to the constraint 6.5. We define the Lagrangian as

$$\mathcal{L} = \mathrm{Tr}(PQ) + \mathrm{Tr}\left[\Lambda\left((A + KC)P + P(A + KC)^* + KQ_vK^* + BQ_dB^*\right)\right] \tag{6.7}$$

where Λ is a matrix Lagrange multiplier. At an extremum, the gradient of $\mathcal{L}$ with respect to Λ, P and K must vanishes. The gradient with respect to Λ gives back the Lyapunov equation

$$\nabla_\Lambda \mathcal{L} = (A + KC)P + P(A + KC)^* + KQ_vK^* + BQ_dB^* = 0 \tag{6.8}$$

Considering the gradient with respect to P, we get

$$\nabla_P \mathcal{L} = 0 = Q + A^*\Lambda^* + C^*K^*\Lambda^* + \Lambda^*A + \Lambda^*KC$$

or,

$$(A + KC)^*\Lambda + \Lambda^*(A + KC) + Q = 0 \tag{6.9}$$

The equation 6.9 is a Lyapunov equation in terms of Q, where Q is self-adjoint and (A+KC) is stable. Now considering the gradient of $\mathcal{L}$ with respect to K we get,

$$\nabla_K \mathcal{L} = 0 = \Lambda^*PC^* + \Lambda PC^* + \Lambda^*KQ_v + \Lambda KQ_v$$

or,

$$2\Lambda(PC^* + KQ_v) = 0$$

That is,

$$K = -PC^*Q_v^{-1} \tag{6.10}$$

Now using 6.10 in equation 6.8. we find

$$AP - PC^*Q_v^{-1}CP + PA^* - PC^*Q_v^{-1}CP^* + PC^*Q_v^{-1}CP^* + BQ_dB^* = 0$$

or,

$$AP + PA^* - PC^*Q_v^{-1}CP + BQ_dB^* = 0 \tag{6.11}$$

Which is the algebraic Riccati equation. The algebraic Riccati equation is widely used for linear quadratic control and estimation problems with infinite time horizon [Doyle et al., 1989]. The solution of equation 6.11 are used to update Kalman gain for stabilisation of a system using equation 6.10. The algebraic Riccati equation is time-independent and resulting a steady Kalman gain. For systems with finite horizon, the algebraic Riccati equation is not suitable and differential Riccati equation is required to compute time-dependent Kalman gain [Högberg, 2001, Lewis, 2012].

The weighting operators Q_v and Q_d are the variances of $\mathbf{v}$ and $\mathbf{d}$ respectively. These weighting operators Q_v and Q_d are assumed to be finite and can be considered as the model parameters.

6.3 Estimation in pendulum-cart system

As a simple demonstration of the method, let us consider a pendulum-cart system [Murray, 2006] as in Figure: 6.2. The pendulum is attached to the cart and the cart can move in X-direction. The pendulum can spin freely about its fixed point (colored red).

The states of the problem are the position x and the velocity dx/dt, the angle θ and its rate of

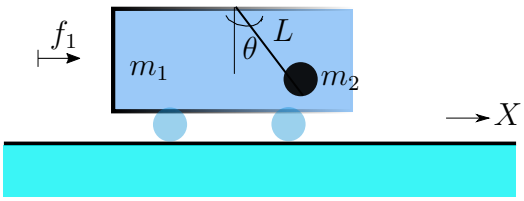

Figure 6.2: A schematic diagram of a inverted pendulum-cart system. Here, L is the length of the pendulum, f_1 is the force acting on the system and, m_1 and m_2 are being the mass of the cart and the pendulum respectively. The only direction in which the cart can move is denoted as the X-axis. The position $\mathbf{x}$ is being measured.

change $d\theta/dt$. The model describing the pendulum-cart system is given by,

$$\begin{aligned} \frac{d\mathbf{x}}{dt} &= A\mathbf{x} + B\mathbf{d} \\ \mathbf{y} &= C_y\mathbf{x} \end{aligned} \tag{6.12}$$

where, $\mathbf{x} = (x, dx/dt, \theta, d\theta/dt)^T$ is the state variable. The definition of A, B and C_y are given as follows [Murray, 2006],

$$A = \begin{bmatrix} 0 & 0 & 1 & 0 \\ 0 & -d/m_1 & -m_2 g/m_1 & 0 \\ 0 & 0 & 0 & 1 \\ 0 & -sd/(m_1 L) & -s(m_2+m_1)/(m_2 L) & 0 \end{bmatrix}$$

$$B = \begin{bmatrix} 1 & 0 & 0 & 0 \\ 0 & 1 & 0 & 0 \\ 0 & 0 & 1 & 0 \\ 0 & 0 & 0 & 1 \end{bmatrix} \tag{6.13}$$

$$C_y = \begin{bmatrix} 1 & 0 & 0 & 0 \end{bmatrix}$$

The model is valid only for small fluctuations about the fixed position $\theta = 0$. We first build up a data-set using the model (6.12) with chosen $\mathbf{d}$. We choose the components of $\mathbf{d}$ as a Gaussian white noise in time with variance 1. Now, an estimation problem can be formed as follows:

among the four variables of the system, x, dx/dt, θ and $d\theta/dt$, only one variable, x is available from the data-set. What would be the other state variables?

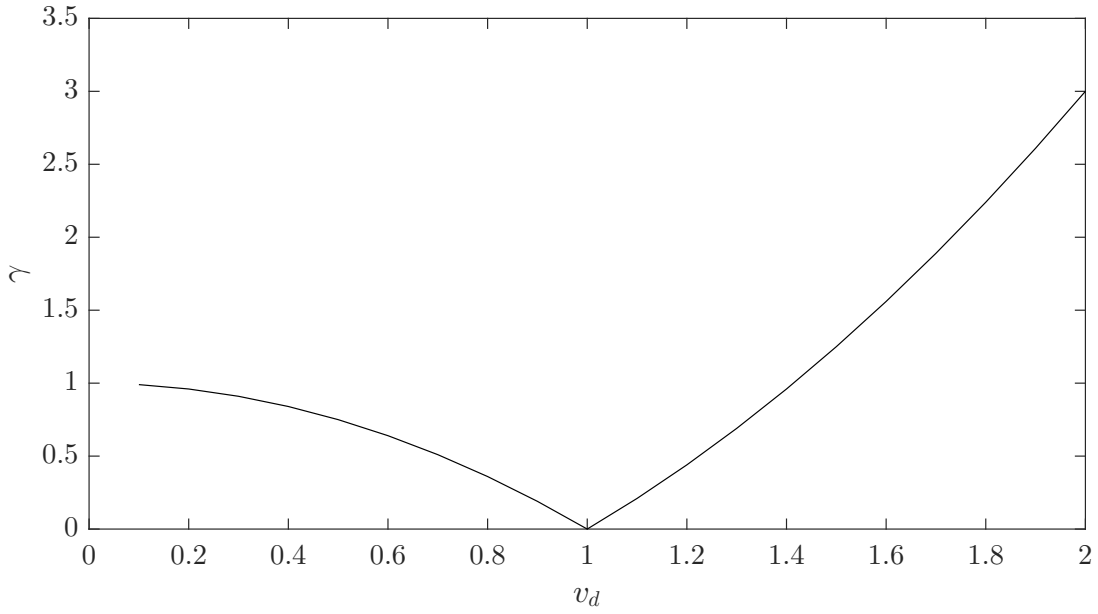

Figure 6.3: Estimation of the optimal v_d that corresponds to the minimum γ. Here, the optimal v_d is equal to 1.

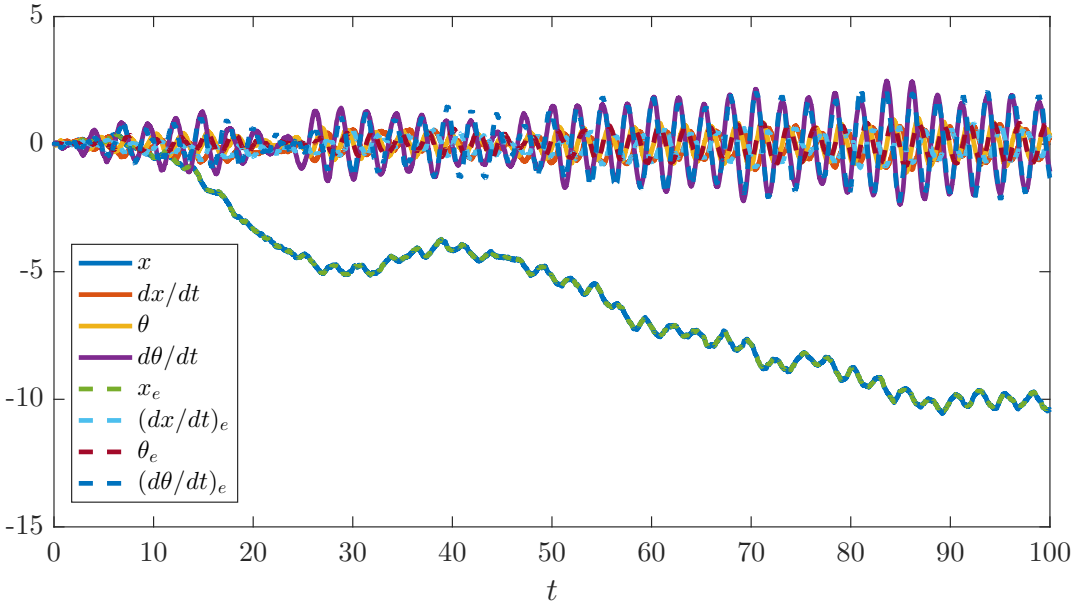

Figure 6.4: Estimation of the states of a pendulum-cart system. The solid lines are the true states and the dashed lines are the estimates.

The model 6.12 does not include any measurement noise. However, to get a finite Kalman gain using equation (**??**) a non-zero variance of the measurement noise Q_v, is required. In this

pendulum-cart problem, the Kalman gain was computed using $Q_v = 10^{-10}$. This choice of Q_v allows us to get a finite Kalman gain whereas the measurement noise is kept low.

The Kalman gain equation (**??**) uses the solution of the algebraic Riccati equation (**??**) which requires Q_d and Q_v, the variance of the disturbance and measurement noise, respectively. Since for the current problem we choose a fixed non-zero Q_v, the Kalman gain K depends only on Q_d. We assume $Q_d = v_d[1 \quad 1 \quad 1 \quad 1]$, where v_d is a constant that needs to be evaluated. Let us consider x_e is a estimation of the position x. Since the estimate x_e is dependent only on v_d, we want to find v_d that minimises

$$\gamma = \sqrt{\int_0^T (x - x_e)^2 \, dt} \Big/ \sqrt{\int_0^T x^2 dt} \tag{6.14}$$

where, T is the time period considered in the estimation problem. To find the optimal v_d, we estimate x_e for the values of v_d ranges from 0.1 to 2 with increments 0.1 and choose the v_d corresponding to the minimum γ. Figure 6.7 shows the minimum γ is achieved for $v_d = 1$.

The Kalman filter assumes the disturbance of a model as a Gaussian white noise. Also the data-set was built assuming the components of $\mathbf{d}$ as the Gaussian white noise with variance 1. Thus the estimated optimal v_d should be the same as the data-set. Indeed, we find the minimum γ is corresponding to $v_d = 1$. The estimated state variables $\mathbf{x}_e$ are shown along with the actual or true states in the figure 6.4. The agreements are reasonably good with relative estimation error is less than 25% for all the states.

6.4 Model for plane Couette flow

In this section, we will develop a model for plane Couette flow. The streamwise, spanwise and wall normal directions are along the x, y and z-axis, and the corresponding components of the velocity $\mathbf{u}$ are u, v and w respectively. The flow quantities are non-dimensionalised using wall units such as friction velocity u_τ, kinematic viscosity ν and half of the channel height h. The pressure $\tilde{p}$ and the time are non-dimensionalised by ρu_τ^2 and $0.5h/u_\tau$ respectively. Then the

momentum equation in non-dimensional form is given by

$$\frac{\partial \mathbf{u}^+}{\partial t} = -(\mathbf{u}^+ \cdot \nabla)\mathbf{u}^+ - \nabla p + Re_\tau^{-1}\nabla^2\mathbf{u}^+ \tag{6.15}$$

For convenience, we drop the superscript + for the rest of the section and write

$$\frac{\partial \mathbf{u}}{\partial t} = -(\mathbf{u} \cdot \nabla)\mathbf{u} - \nabla p + Re_\tau^{-1}\nabla^2\mathbf{u} \tag{6.16}$$

We perform a Reynolds decomposition of the velocity field $\mathbf{u}$ as

$$\mathbf{u} = \langle \mathbf{u} \rangle + \mathbf{u}'' \tag{6.17}$$

where $\langle \mathbf{u} \rangle$ is the temporal average of the velocity and $\mathbf{u}''$ is the fluctuation. Averaging (6.16) over time, we get

$$\frac{\partial \langle \mathbf{u} \rangle}{\partial t} = -\left(\langle \mathbf{u} \rangle \cdot \nabla\right) \langle \mathbf{u} \rangle - \langle (\mathbf{u} \cdot \nabla)\mathbf{u} \rangle - \nabla \langle P \rangle + Re_\tau^{-1}\nabla^2\langle \mathbf{u} \rangle \tag{6.18}$$

Subtracting (6.18) from (6.16),

$$\frac{\partial \mathbf{u}''}{\partial t} = -(\langle \mathbf{u} \rangle \cdot \nabla)\mathbf{u}'' - (\mathbf{u}'' \cdot \nabla)\langle \mathbf{u} \rangle - \nabla p'' + Re_\tau^{-1}\nabla^2\mathbf{u}'' + \langle (\mathbf{u}'' \cdot \nabla)\mathbf{u}'' \rangle - (\mathbf{u}'' \cdot \nabla)\mathbf{u}'' \tag{6.19}$$

Let us denote $\mathbf{d} = \langle (\mathbf{u}'' \cdot \nabla)\mathbf{u}'' \rangle - (\mathbf{u}'' \cdot \nabla)\mathbf{u}''$, such that

$$\frac{\partial \mathbf{u}''}{\partial t} = -(\langle \mathbf{u} \rangle \cdot \nabla)\mathbf{u}'' - (\mathbf{u}'' \cdot \nabla)\langle \mathbf{u} \rangle - \nabla p'' + Re_\tau^{-1}\nabla^2\mathbf{u}'' + \mathbf{d} \tag{6.20}$$

To get a linear model, we should truncate [Kim and Bewley, 2007] the non-linear forcing $\mathbf{d}$ from the equation (6.20). Instead we keep the forcing $\mathbf{d}$ in the model while assuming $\mathbf{d}$ is a

disturbance (white noise) to the model (i.e. does not depend on $\mathbf{u}$). Then the variance of $\mathbf{d}$ is a model parameter which need to be estimated from measurements/sensors. Let us project the model in the Fourier space. For each wavenumber pair (k_x, k_y) the state-space form is as [Illingworth et al., 2018],

$$\frac{\partial}{\partial t}\begin{bmatrix}\hat{w}''\\ \hat{\eta}''\end{bmatrix} = \begin{bmatrix}\Delta^{-1}\mathcal{L}_{OS} & \mathbf{0}\\ \mathcal{L}_C & \mathcal{L}_{SQ}\end{bmatrix}\begin{bmatrix}\hat{w}''\\ \hat{\eta}''\end{bmatrix} + \begin{bmatrix}-ik_x\Delta^{-1}\mathcal{D} & -ik_y\Delta^{-1}\mathcal{D} & -k^2\Delta^{-1}\\ ik_x & -ik_y & \mathbf{0}\end{bmatrix}\begin{bmatrix}\hat{d}_x\\ \hat{d}_y\\ \hat{d}_z\end{bmatrix} \tag{6.21}$$

$$\begin{bmatrix}\hat{u}''\\ \hat{v}''\\ \hat{w}''\end{bmatrix} = \frac{1}{k^2}\begin{bmatrix}ik_x\mathcal{D} & -ik_y\\ ik_y\mathcal{D} & ik_x\\ k^2 & \mathbf{0}\end{bmatrix}\begin{bmatrix}\hat{w}''\\ \hat{\eta}''\end{bmatrix} \tag{6.22}$$

where, $\hat{u}''$, $\hat{v}''$, $\hat{w}''$ and $\hat{\eta}''$ are the Fourier transform of the streamwise, spanwise and wall normal velocity components' fluctuations, and the wall normal component fluctuation of vorticity, respectively. The boundary conditions are $\hat{w}''(0,t) = \partial_z w''(0,t) = \hat{\eta}''(0,t) = \hat{w}''(h,t) = \partial_z w''(h,t) = \hat{\eta}''(h,t) = 0$, where, h is the height of the channel. We recall that the model (6.21)-(6.22) is for the perturbed quantities and the perturbation of all the three velocity components vanishes at the wall. Equation 6.16 is the well-known Orr-Sommerfeld equation which involves the wall normal component of velocity fluctuation and the vorticity fluctuation, respectively. We use equation 6.17 to evaluate the streamwise and spanwise components of the velocity fluctuation from the wall normal component of velocity fluctuation and the vorticity fluctuation.

Here, $(\hat{d}_x, \hat{d}_y, \hat{d}_z)^T$ are the Fourier transform of the components of $\mathbf{d}$, $\mathcal{L}_{OS} = -ik_x\langle u\rangle\Delta + ik_x\dfrac{d^2\langle u\rangle}{dz^2} + Re_\tau^{-1}\Delta^2$, $\mathcal{L}_C = -ik_y\dfrac{d\langle u\rangle}{dz}$ and $\mathcal{L}_{SQ} = -ik_x\langle u\rangle + Re_\tau^{-1}\Delta$. The operators $D = \dfrac{\partial}{\partial z}$, $k^2 = k_x^2 + k_y^2$ and $\Delta = D^2 - k^2$ are the Laplacian operator. In this description, both $\hat{w}''$ and $\hat{\eta}''$ are functions of time t and wall normal coordinate z. We note that, the model (6.21)-(6.22) is a linear model where the non-linear interactions of the fluctuation $\mathbf{u}$ are grouped as the disturbance/forcing $\mathbf{d}$.

6.4.1 Testing the numerical operators

We design four problems to test the numerical routines used to evaluate the operators D, D^2, D^4 and Δ^2 of the model (6.21)-(6.22) as shown in table 6.1. Problem (d) in table 6.1 is a special case of the Orr-Sommerfeld equation (with forcing) where $k_x = 0$, $k_y = 1$ and $Re_\tau = 10$. The numerical routines transform the domain into $[-1 \quad 1]$ and the operators are evaluated at Chebychev collocation points. For clamped boundary conditions in problem (c-d) (table 6.1), we use the algorithm from [S. C. Reddy et al., 1998]. This algorithm implements two important strategies. The first strategy is the use of trigonometric identity to avoid direct computation of the differences between Chebychev points $x(k) - x(j)$ and the second strategy is to flip the order of modes as $\sin t$ can be computed with with relatively higher precision compared to $\sin(\pi - t)$.

Problem List		
No.	Problem	Exact solution
(a)	$Dw = -2z$, $z \in [-1 \quad 1]$ $w(-1) = w(1) = 0$	$w(z) = 1 - z^2$
(b)	$D^2w = -2$, $z \in [-1 \quad 1]$ $w(-1) = w(1) = 0$	$w(z) = 1 - z^2$
(c)	$D^4w = -1$, $z \in [-1 \quad 1]$ $w(-1) = w'(-1) = w(1) = w'(1) = 0$	$w(z) = \frac{1}{24}(-z^4 + 2z^2 - 1)$
(d)	$\Delta^2 w = 10$, $k = 1$, $z \in [-1 \quad 1]$ $w(-1) = w'(-1) = w(1) = w'(1) = 0$	$w(z) = 10 - (4.831 - 2.089y)e^y - (4.831 + 2.089y)e^{-y}$

Table 6.1: List of problems designed to test numerical routines for operators. The performance of the numerical routines are shown in the figure 6.5(a-d).

Figure 6.5(a-d) show the numerical results estimated from the routines that produces good estimation of the exact solution. We also apply the numerical routines to evaluate the eigenvalues of Orr-Sommerfeld operator for plane Poiseuille flow [Schmid and Henningson, 2001] at $Re = 10^4$ and wave number $\alpha = 1$. We use 300 collocation points for simulation. The obtained eigenvalues are compared with published result and found good agreement. The comparisons in this section was performed to validate the numerical routines which will be used to dynamical models discussed later.

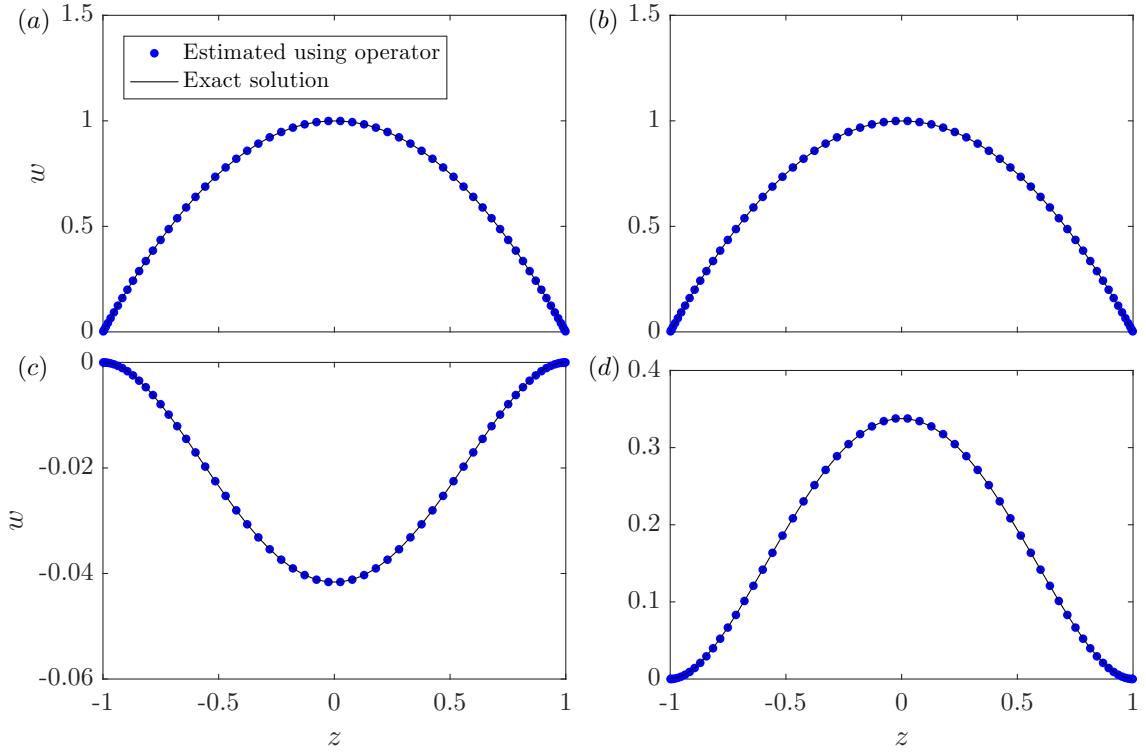

Figure 6.5: Validation of the operators with numerical examples, (a) D, (b) D^2, (c) D^4 and (d) $\Delta^2 = (D^2 - k^2)$ with $k = 1$. Solid lines are the exact results and the blue dots are the estimated results using operators. The designed problems and the exact solutions are presented in table 6.1.

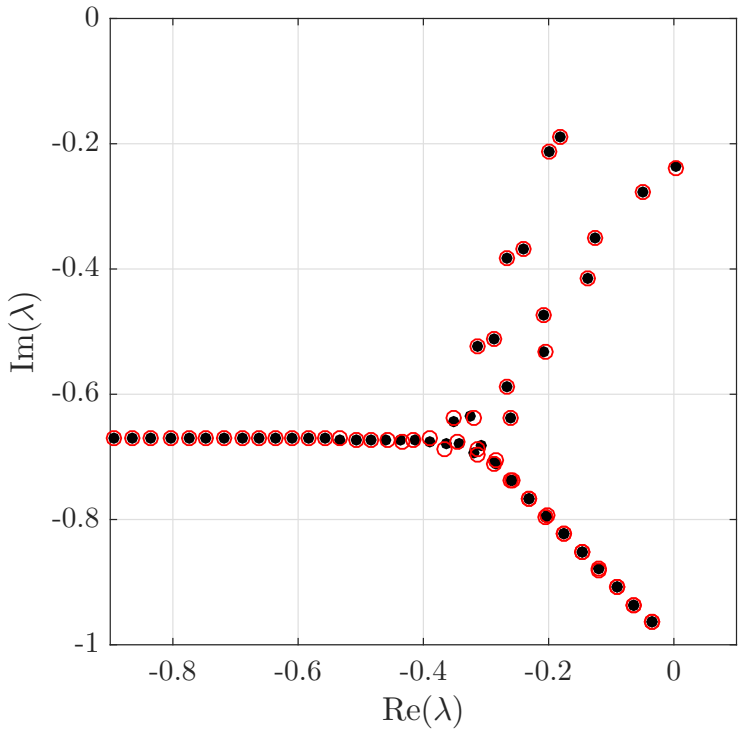

Figure 6.6: Eigenvalue spectra of the Orr-Sommerfeld operator for plane Poiseuille flow with velocity component $u = 1 - z^2$ at $Re = 10^4$ and wave number $\alpha = 1$.

6.5 Linear model for scalar transport

The scalar transport equation is presented in chapter 2 as

$$\frac{\partial \theta}{\partial t} = -(\mathbf{u} \cdot \nabla)\theta + \kappa \nabla^2 \theta \tag{6.23}$$

Here, θ is a scalar and κ is the coefficient of thermal conductivity. We use $\theta^+ = \left(\overline{\theta_w} - \theta\right)/\theta_\tau$ with $\theta_\tau = q_w/u_\tau$, where θ_w is the wall temperature and q_w is the wall heat flux, to non-dimensionalise equation (6.23) as,

$$\frac{u_\tau \theta_\tau}{h}\frac{\partial \theta^+}{\partial t^+} = -\frac{u_\tau \theta_\tau}{h}(\mathbf{u}^+ \cdot \nabla^+)\theta^+ + \kappa \frac{\theta_\tau}{h^2}\nabla^{*2}\theta^+ \tag{6.24}$$

Dividing throughout by $(u_\tau \theta_\tau)/h$ and dropping superscript $^+$,

$$\frac{\partial \theta}{\partial t} = -(\mathbf{u} \cdot \nabla)\theta + \frac{Pr}{Re_\tau}\nabla^2 \theta \tag{6.25}$$

Now applying Reynolds decomposition on the scalar θ as,

$$\theta(\mathbf{x}, t) = \Theta(\mathbf{x}) + \theta''(\mathbf{x}, t) \tag{6.26}$$

where, $\Theta = \frac{1}{T}\langle\theta\rangle = \frac{1}{T}\int_0^T \theta \, dt$, T is the time period and θ'' is the fluctuation about the time averaged Θ. Now applying (6.17) and (6.26) to (6.25),

$$\frac{\partial \theta''}{\partial t} = -\langle\mathbf{u}\rangle \cdot \nabla\Theta - \langle\mathbf{u}\rangle \cdot \nabla\theta'' - \mathbf{u}'' \cdot \nabla\Theta - \mathbf{u}'' \cdot \nabla\theta'' + \frac{Pr}{Re_\tau}\nabla^2\left(\Theta + \theta''\right) \tag{6.27}$$

Taking time average,

$$0 = -\langle\mathbf{u}\rangle \cdot \nabla\Theta - \langle\mathbf{u}'' \cdot \nabla\theta''\rangle + \frac{Pr}{Re_\tau}\nabla^2\Theta \tag{6.28}$$

Subtracting (6.28) from (6.27),

$$\frac{\partial \theta''}{\partial t} = -\langle \mathbf{u} \rangle \cdot \nabla \theta'' - \mathbf{u}'' \cdot \nabla \Theta + \frac{Pr}{Re_\tau} \nabla^2 \theta'' - \mathbf{u}'' \cdot \nabla \theta'' + \langle \mathbf{u}'' \cdot \nabla \theta'' \rangle \tag{6.29}$$

Since $\langle \mathbf{u} \rangle = (\langle u \rangle, 0, 0)$ and assuming non-linear terms in u_j'' and θ'' as $d_\theta = -\mathbf{u}'' \cdot \nabla \theta'' + \langle \mathbf{u}'' \cdot \nabla \theta'' \rangle$, equation (6.29)

$$\frac{\partial \theta''}{\partial t} = \left(-\langle u \rangle \frac{\partial}{\partial x} + \frac{Pr}{Re_\tau} \nabla^2 \right) \theta'' - w'' \frac{d\Theta}{dz} - d_\theta \tag{6.30}$$

We recall that the variables are in plus unit throughout this section and equation (6.30) is an equation for the perturbation θ''. Thus the boundary conditions for the scalar equation are $\dfrac{\partial \theta''}{\partial z} = 0$ and $\theta'' = 0$ at the bottom and top wall, respectively.

Finally, taking the Fourier transform,

$$\frac{\partial \hat{\theta}''}{\partial t} = \left(-ik_x \langle u \rangle + \frac{Pr}{Re_\tau} (D^2 - k^2) \right) \hat{\theta}'' - \hat{w}'' \frac{d\Theta}{dz} - \hat{d}_\theta \tag{6.31}$$

Now using (6.31) along with (6.21), for each wavenumber pair (k_x, k_y) the state-space model is given by

$$\frac{\partial}{\partial t} \begin{bmatrix} \hat{w}'' \\ \hat{\eta}'' \\ \hat{\theta}'' \end{bmatrix} = \begin{bmatrix} \Delta^{-1}\mathcal{L}_{OS} & \mathbf{0} & \mathbf{0} \\ \mathcal{L}_C & \mathcal{L}_{SQ} & \mathbf{0} \\ \mathcal{L}_D & \mathbf{0} & \mathcal{L}_\theta \end{bmatrix} \begin{bmatrix} \hat{w}'' \\ \hat{\eta}'' \\ \hat{\theta}'' \end{bmatrix} + \begin{bmatrix} -ik_x\Delta^{-1}\mathcal{D} & -ik_y\Delta^{-1}\mathcal{D} & -k^2\Delta^{-1} & \mathbf{0} \\ ik_x & -ik_y & \mathbf{0} & \mathbf{0} \\ \mathbf{0} & \mathbf{0} & \mathbf{0} & \mathbf{I} \end{bmatrix} \begin{bmatrix} \hat{d}_u \\ \hat{d}_v \\ \hat{d}_w \\ \hat{d}_\theta \end{bmatrix} \tag{6.32}$$

$$\begin{bmatrix} \hat{u}'' \\ \hat{v}'' \\ \hat{w}'' \end{bmatrix} = \frac{1}{k^2} \begin{bmatrix} ik_x\mathcal{D} & -ik_y \\ ik_y\mathcal{D} & ik_x \\ k^2 & \mathbf{0} \end{bmatrix} \begin{bmatrix} \hat{w}'' \\ \hat{\eta}'' \end{bmatrix} \tag{6.33}$$

where, $\hat{w}''$, $\hat{\theta}''$ and $\hat{\eta}''$ are the Fourier transform of the wall normal velocity component fluctuation, scalar fluctuation and the wall normal components' fluctuation of vorticity, respectively. The boundary conditions $\hat{w}''(0,t) = \partial_z\hat{w}''(0,t) = \hat{\eta}''(0,t) = \hat{w}''(h,t) = \partial_z\hat{w}''(h,t) = \hat{\eta}''(h,t) = 0$. For scalar, the boundary equations are $\dfrac{\partial\hat{\theta}''}{\partial z}(0,t) = 0$ and $\hat{\theta}''(h,t) = 0$. Equation (6.22) is presented again as equation (6.33) to describe the model (6.32)-(6.33) in a compact form.

Here, $(\hat{d}_x, \hat{d}_y, \hat{d}_z, \hat{d}_\theta)^T$ are the Fourier transform of the components of $\mathbf{d}_\theta = (d_x, d_y, d_z, d_\theta)^T$, $\mathcal{L}_\theta = -ik_x\langle u\rangle + PrRe_\tau^{-1}\Delta$ and $\mathcal{L}_D = -\dfrac{d\Theta}{dz}$. The operators $\mathcal{L}_{OS}$, $\mathcal{L}_C$ and $\mathcal{L}_{SQ}$ are defined elsewhere. The operator $D = \frac{\partial}{\partial z}$, $k^2 = k_x^2 + k_y^2$ and $\Delta = D^2 - k^2$ are the Laplacian operator. The model consisting of (6.32) and (6.33) is a linear model for which the non-linear interactions of u'' and θ'' are assumed as a disturbance $\mathbf{d}_\theta$ of the model. We assume that the disturbance is a white noise [Illingworth et al., 2018] with zero mean and finite variance. We will use this model (6.32)-(6.33) to estimate flow velocity from wall temperature.

6.6 Estimation of flow velocity with random disturbances

Before using the DNS data-set we design a problem to estimate the flow velocity from the wall temperature using the model (6.32)-(6.33) with random disturbances. We first evaluate the model for known disturbances to build the data-set which we consider as measurements. The disturbance $\mathbf{d}_\theta$ is assumed to be white in time and space. To build the data-set, we consider the parameters, such as length, width and height of the $3D$ domain, Prandtl number Pr and Re_τ of the plane Couette flow in chapter 2. Again, we recall that the DNS data-set will not be used for estimation and we will only use the case setup as in chapter 2. We consider 150 collocation points to simulate the model for the wavenumber pair $(\pi/6, \pi/3)$ by considering the components of $\mathbf{d}$ are Gaussian white noises with variances equal to 10^{-3}. The simulated results are considered as the data-set.

The next step is to use the Kalman filter to estimate the flow velocity form the wall temperature. Here, we consider the flow velocity is unknown. We recall that, to get a finite Kalman gain it is required to consider a non-zero measurement variance and we set $Q_v = 10^{-10}$ which is same

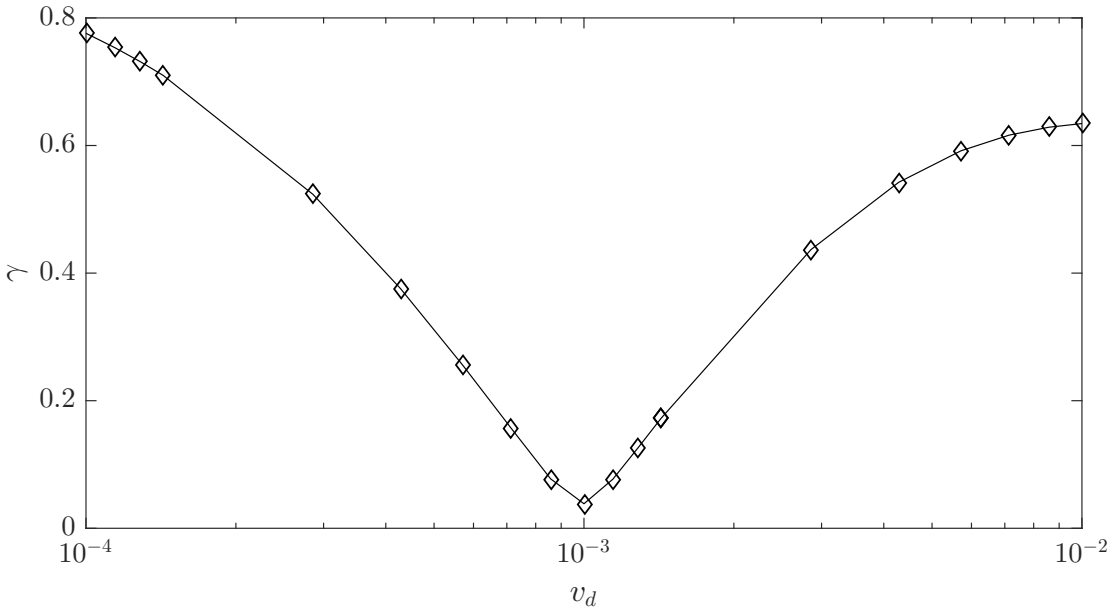

Figure 6.7: Estimating the optimal v_d for the reconstruction of the flow with random forcing.

as the pendulum-cart system. To evaluate the Kalman gain using equations (**??**) and (**??**), we only need to estimate is Q_d. We consider Q_d is of following form

$$Q_d = v_d \begin{bmatrix} \mathbf{I} & \mathbf{I} & \mathbf{I} & \mathbf{I} \end{bmatrix} \tag{6.34}$$

Here, v_d is a constant. Since the streamwise component of velocity is strongly correlated with the wall temperature, we consider the same variance v_d for all the components of Q_d. To estimate the optimal v_d, we minimise the following

$$\gamma = \sqrt{\int_0^T \left(\hat{\theta}''_w - \hat{\chi}''_w\right)\left(\hat{\theta}''_w - \hat{\chi}''_w\right)^* dt} \Bigg/ \sqrt{\int_0^T \hat{\theta}''_w \hat{\theta}''^*_w dt} \tag{6.35}$$

where, χ''_w is the estimated wall temperature from the model that depends on v_d. The value of v_d for which γ of (6.35) is minimum is the optimal v_d for the estimation. Figure 6.7 shows γ for the values of v_d ranges from 10^{-4} to 10^{-2}. The minimum γ is found for $v_d = 10^{-3}$ which is the same as the variance considered to build the data-set .

The reconstructed velocity components for a wavenumber pair $(\pi/6, \pi/3)$ are presented in figure 6.8(a-c). For all the cases, we achieve a good reconstruction with exception at some of the peaks

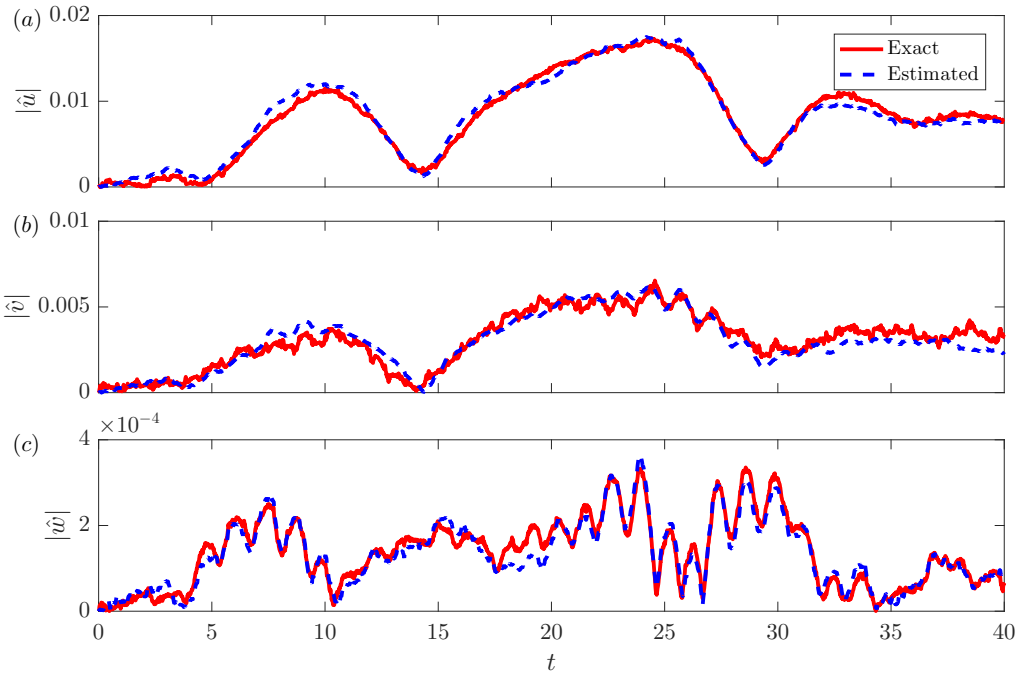

Figure 6.8: Estimation of the modulus of the velocity components (a) $\hat{u}$, (b) $\hat{v}$ and (c) $\hat{w}$, at $z^+ = 35$, $k_x = \pi/6$ and $k_y = \pi/3$, using wall temperature. The velocity components are the response of the model excited with random forcing. The red solid line and the blue dashed line are the exact and estimated quantities respectively.

in the time series.

The model successfully estimates the flow velocity when the disturbances are random white signal in space and time. In next section, we will use the wall temperature from the DNS data-set while we still assume the disturbances are random.

6.7 Estimation of flow velocity using wall temperature

In this section, we will use the model (6.32)-(6.33) to estimate flow velocity from the DNS wall temperature. We acquire the wall temperature and the flow velocity at a temporal resolution of $\Delta t^+ = 0.0021$, which corresponds to approximately 10 DNS time steps. We consider 130 consecutive snapshots; within this time period, the top wall moves approximately 1.5 channel lengths ($2TU = 1.534L_x$) in the streamwise direction. To reconstruct velocity at $z^+ = 35$, we consider 17 streamwise and 64 spanwise wavenumbers. This choice is motivated from the joint PDF (figure 3.3) analysis in chapter 3.

For the estimation in the Fourier space, we choose $q_v = 10^{-10}$. This small value of Q_v was used in previous examples to evaluate a finite Kalman gain while the measurement noise was kept low. We use equations (**??**) and (**??**) to evaluate the Kalman gains for the different values of v_d, where v_d is defined in equation (6.34).

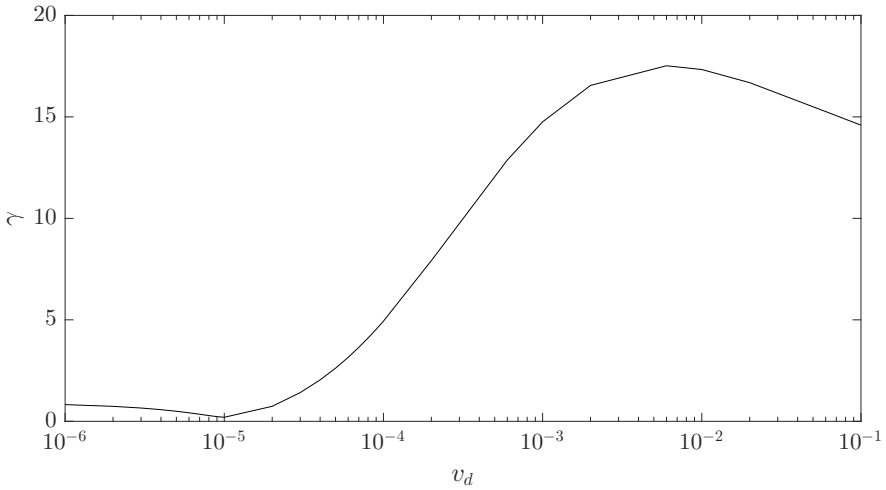

Figure 6.9: Estimating the optimal v_d for the wavenumber pair $(\pi/3, \pi/6)$.

For each wavenumber pair, we estimate $\hat{\chi}''_w$, where $\hat{\chi}''_w$ is the estimated wall temperature, for the values of v_d ranges from 10^{-6} to 10^{-1}. The optimal v_d is the value of v_d that minimises γ of equation (6.35). Then the flow velocity is estimated using the optimal v_d in the Fourier space. For example, figure 6.9 presents the γ versus v_d curve for the wavenumber pair $(\pi/3, \pi/6)$ and the minimum γ can be observed at $v_d = 1 \times 10^{-5}$.

Figure 6.10 shows the reconstruction of the velocity component and the wall temperature with the optimal v_d. Since the DNS wall temperature is used for flow estimation, the variance of the disturbances are not known *a priori*. The reconstructed wall temperature $\hat{\chi}''_w$ is found to be a good fit for the DNS wall temperature $\hat{\theta}''_w$. This fit confirms that the estimated variance of the disturbance corresponding to the wall temperature $\hat{d}_\theta$, is a good estimation.

The model yields a reasonably good estimation for the streamwise component $\hat{u}''$ for $25 \leq t^+ \leq 50$, but under-estimate the peaks in the first half of the time series containing relatively higher peaks. The estimations of other two velocity components are not particularly good which is expected as the correlation of these components with the wall temperature are not as strong as the streamwise component.

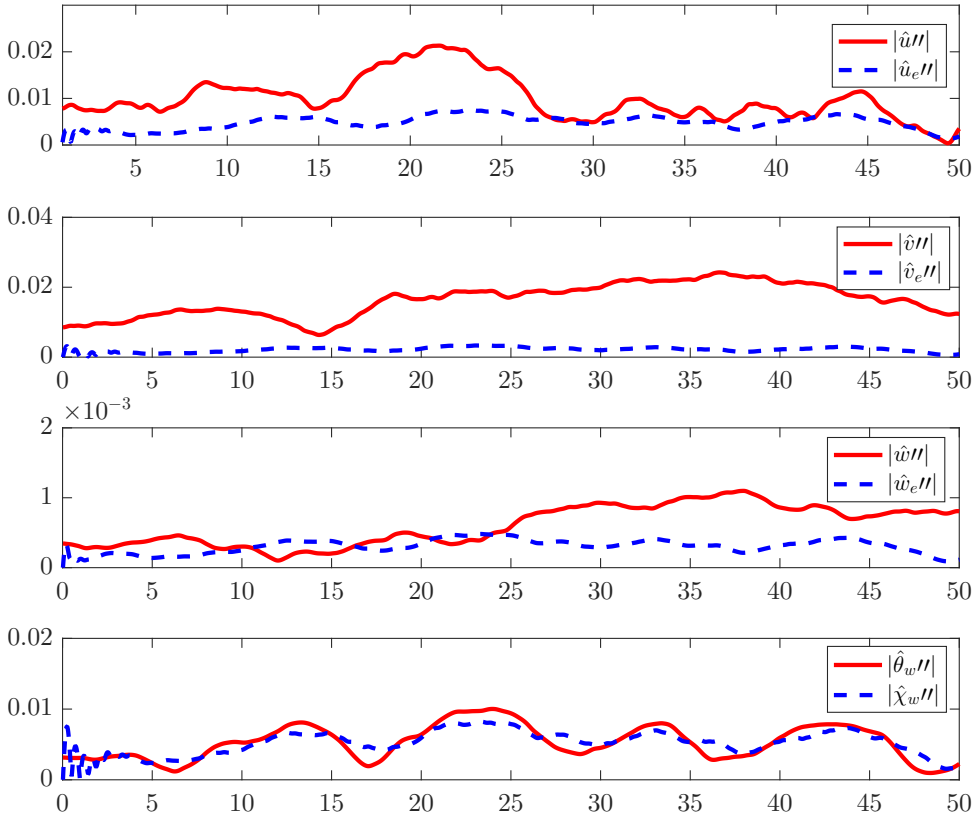

Figure 6.10: Reconstructing the fluctuation of the velocity component $\hat{u}''$, $\hat{v}''$, $\hat{w}''$ and the wall temperature $\hat{\theta}''$ in the Fourier space for $k_x = \pi/3$ and $k_y = \pi/6$. The red line is the time series obtained from the DNS and the blue dashed line is the modeled quantity. Here, $\hat{\chi}_w''$ is the estimated wall temperature obtained using the optimal $v_d = 10^{-5}$.

The estimated flow velocity in the Fourier series are transformed to the physical space using the inverse Fourier transform. The exact DNS streamwise velocity component along with the reconstructed snapshot is presented in figure 6.11(a-b), respectively. It is clear that the reconstructed snapshot resembles the exact DNS snapshot except possibly the peaks which is both due to wavenumber truncation and the limitation observed in the wavenumber space (figure 6.10). The relative error for the reconstructions over considered time interval T is 0.27. In the estimated snapshot 6.11(b), the structures that are long in the streamwise direction and thin in the spanwise direction are reconstructed more accurately. Here, we estimate flow at $z^+ = 35$ which is still close to wall. It will be interesting to investigate how the model performs further away from the wall and is a scope for future work.

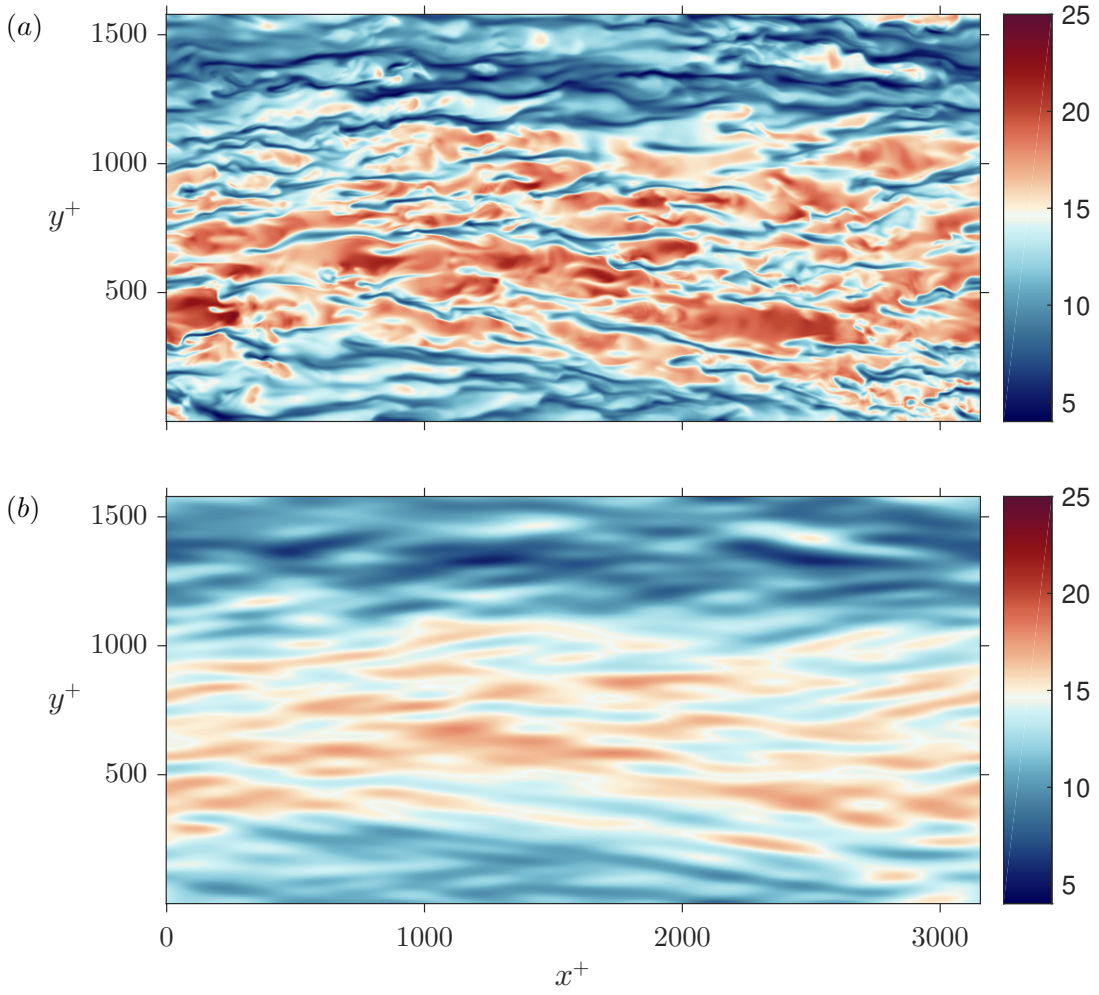

Figure 6.11: Estimation of the streamwise velocity component u (a) obtained from the DNS, (b) the reconstructed snapshot using the model, at $z^+ = 35$,

6.8 Conclusions

We tested the numerical routines to approximate the operators used in the Orr-Sommerfeld-Squire system using Chebychev collocation method. The routines were tested using suitable examples in table 6.1 and the eigenvalue spectrum of the plane Poiseuille flow at $Re = 10^4$. All the numerical routines were found to yield good approximations of system operators and reproduced the eigenvalue spectrum.

We presented a model for scalar transport – which along with Orr-Sommerfeld-Squire system form a complete dynamical system. In this system, any non-linear terms of $\mathbf{u}''$ and θ'' are grouped and are treated as disturbances. This implies that the resulting model is linear in $\mathbf{u}''$ and θ''.

To test the performance of the model, we designed two problems. The first problem is a pendulum-cart system driven by a random forcing. We successfully reproduced the variance of the random forcing using the Kalman filter. The relative error for the reconstructed system variables was found 0.25.

The second problem was designed such that the measurements were obtained from the response of the model using random forcing $\mathbf{d}_\theta$. We found the optimal variance Q_d by minimising the difference between the modeled and measured wall temperature. The reconstructed velocity components are obtained as the model outputs and found to be a good fit of the measured wall temperature.

Finally we move to our key problem - reconstruction of the flow velocity from the wall temperature. We undertook the same procedure as the problem with the random disturbances. Indeed, we used the DNS wall temperature as measurements and found the optimal variance Q_d for wavenumber pairs to reconstruct flow velocity. The reconstructed streamwise component of the velocity resembles the exact DNS snapshot except the picks with $\gamma = 0.27$. The model was particularly good to reconstruct the structures that are long in the streamwise direction and thin in the spanwise direction, but failed to reconstruct other two velocity components.

We were motivated to use a dynamical model as it provides a physical constraint within the data-driven framework. We succeeded to reconstruct some of the flow structures at $z^+ = 35$. To improve the quality of the reconstruction, a closure model, such as eddy viscosity model [Illingworth et al., 2018] can be included in the model. Future works should also include the reconstructions of the flow velocity further away from the wall and reconstructions with non-homogeneous surfaces.

Chapter 7

Conclusions

In this thesis, we reconstructed flow velocity form wall temperature using different flow reconstruction methods. Detailed conclusions were presented in each chapters. Some of the key findings and the contribution of the thesis are presented here.

7.1 Summary

We created a data-set for flow reconstructions using direct numerical simulation of heated plane Couette flow with a passive scalar. By imposing a fixed flux condition on the bottom boundary, the wall temperature is free and wall patterns were developed. We considered temperature as a passive scalar [Kasagi et al., 1992, Debusschere and Rutland, 2004] by assuming Richardson number Ri is zero in limiting sense. That is, the role of gravity was not considered in the simulation.

The turbulence statistics obtained from the DNS were compared with previously published results. The mean velocity, the mean temperature, the RMS of the three components of the velocity and stress profiles were found to be in good agreement with the published results. The maximum RMS temperature was found near the bottom wall at $z^+ = 10.34$. The total heat flux matches the theoretical constant value closely, with a relative error in the ℓ^2-norm that is less than 1%.

In chapter 3, we used the strong correlation between the wall temperature θ_w and the wall shear stress τ_w to develop a spectral model. The first three streamwise wavenumbers were found to constitute about 90% of the total variance and the higher wavenumbers showed a asymptotic behaviour in the weighted (energy) wavenumber space. We parameterised the complex model parameter C by its modulus and phase independently. This parameterisation reduced the degrees of freedom significantly. The reconstruction with 17×65 modes yields wall shear stress with relative ℓ_2 error 0.25. The reconstruction under-estimates the wall shear stress at local peaks due to truncation of wavenumbers.

We extensively analysed the POD method by suitably chosen examples - especially with gappy fields in chapter 4. The ratio p which is defined as the ratio of available information to the total information plays an important role in flow reconstructions. For all p, the γ versus N curves collapsed to one curve until they diverged at a certain N. That is, the quality of reconstructions for all p are same up-to a certain number of mode N. To reconstruct flow velocity from wall temperature only, that is a field with large gappiness, we applied LASSO regularisation and it appeared that the LASSO regularisation is more suitable to regularise the resulting under-determined system. The estimated snapshots produced good reconstructions of the key flow structures. The measure of performance γ for the reconstructed snapshot was found as 0.24.

The subdomain POD method divides a physical domain into a number of subdomains and apply the POD method in each subdomain separately. In chapter 5, we tested the same two sets of problems as in chapter 4 to analyse the subdomain POD modes and the reconstructions using the subdomain POD method. We evaluated the subdomain POD modes for the KS equation and the plane Couette flow. In both cases, the reconstructed snapshots were good fits for the actual snapshots. From the second set of problems, we found the reconstruction ability for different p are similar to that were reconstructed using the POD method. To reconstruct flow velocity only from wall temperature, we designed an extrapolation framework and found good reconstructions with $\gamma = 0.245$.

In chapter 6, we developed a model using Orr-Sommerfeld-Squire system and the scalar transport equation. We tested the model using a pendulum-cart system and estimated the model

parameter accurately. We used the Kalman filter and wall temperature to approximate the streamwise component of the flow velocity. In the estimated velocity component u, structures that are long in the streamwise direction and thin in the spanwise direction were successfully reconstructed. The measure of performance for the reconstructed snapshots was found to be 0.27.

7.2 Concluding remarks

In this thesis, we reconstructed flow velocity/shear stress from wall temperature using different flow decomposition methods and dynamical models. We started this thesis to estimate airflow structures in urban environment as the airflow structures play important roles on almost every aspects of city dwellers including public health, energy consumption, real estates, pollution, economy and social interactions. There are many factors that regulates the airflow structures in cities, such as shear, buoyancy, radiation, humidity, rainfall and other forms of precipitations etc. In this thesis, we only focus on the shear-driven flows for which plane Couette flow is a canonical flow. The flow was generated by moving the top wall which drives the scalar θ and the temperature structures develop. Without the loss of generality, we can thus assume the wall temperature θ_w depend only on the velocity $\mathbf{u}$. That is,

$$\theta_w = f(\mathbf{u}) \tag{7.1}$$

where, f is a operator that maps $\mathbf{u}$ to θ_w. Clearly, there are other factors, such as pressure and humidity, that contribute to the wall temperature. These factors are ignored in this discussion as we want to reconstruct the flow velocity from the wall temperature only. Now from (7.1), we get the inverse problem as

$$\mathbf{u} = f^{-1}(\theta_w) \tag{7.2}$$

Here, f^{-1} is the inverse of the operator f. Since the velocity $\mathbf{u}$ is a vector with three components whereas θ_w is only a scalar, approximation of f^{-1} is a under-determined problem. Throughout the thesis, we developed several methods to approximate the inverse operator f^{-1}. In chapter

3, we developed a spectral linear regression model which uses the strong correlation between wall temperature θ_w and wall shear stress $\tau_{\mathbf{w}}$ (and therefore $\mathbf{u}$) and is described as

$$\hat{\tau}''_w = C\hat{\theta}''_w \tag{7.3}$$

where, C is the model parameter. If g is the operator that maps $\hat{\tau}''_w$ into $\hat{\theta}''_w$ then the inverse operator g^{-1} is approximated as

$$g^{-1}\left(\hat{\theta}''_w\right) = \hat{\tau}''_w = C\hat{\theta}''_w \tag{7.4}$$

Since C is complex, the inverse operator g^{-1} can be described as a combination of contraction/magnification operator and rotation operator in the Fourier space.

In chapter 4 and 5, we used flow decomposition methods to approximate the inverse f^{-1}. Both the POD and subdomain POD modes of the state variable $\mathbf{s} = (\mathbf{u}, \theta_w)^T$ represent f^{-1} in the modal space. The wall temperature from the DNS were used as the observations to find the temporal evolution of the inverse operator f^{-1}.

In chapter 6, we assimilated wall temperature to a dynamical model to extract flow velocity. In this case, the operators A and B of the dynamical model provides a link between θ_w and $\mathbf{u}$. If we consider θ_w as the input and $\mathbf{u}$ as the output of the model, then the model operators can be described as an approximation for the inverse operator f^{-1}.

The main contribution of this thesis is the development of different data-driven methods to approximate the inverse operator f^{-1}. Throughout the thesis, we analysed and discussed the pros and cons of each method. Some of the important pros and cons are highlighted in table 7.1. The reconstruction of wall shear stress from wall temperature using the spectral model is attractive for two reasons. First, the use of wall temperature as a proxy is a non-intrusive reconstruction method for wall shear stress. Second, the spectral model can reconstruct distributed wall shear stress. Compared to the conventional data fitting in the physical space, the degrees of freedom of the spectral model were reduced 13 times by our proposed parameteri-

Method	Pros	Cons
Spectral model	1. Has non-intrusive applications. 2. Produces distributed fields. 3. The proposed parametrisation reduces degrees of freedom significantly.	1. The parameterisation prioritise higher energy modes at the expense of the modes containing lower energy. 2. Deals with wall quantities only. 3. Limited ability to produce the local maxima.
POD method	1. The modes are optimal with respect to other linear representation. 2. Reconstruction ability for gappy fields are reasonably good. 3. The method can reconstruct high dimensional sparse fields.	1. The evaluation of the modes requires high computational cost. 2. Limited capability to reproduce structures associated with lower energy.
Subdomain POD method	1. The modes are locally optimised. 2. The modes inherit properties from the POD modes. 3. Does not need to include the whole domain. 4. Produces reconstructions as good as the POD method.	1. Computational cost increases by a factor equal to the number of subdomains. 2. Needs extra attention to ensure the continuity. 3. The background fields require information, at the boundary of the subdomains.
Dynamical model	1. Computationally cheaper compared to the flow decomposition methods as no modes are required *a priori*. 2. Uses dynamical equations. 3. The linear estimation theory is applicable. 4. Estimations in the Fourier space require to fit only one parameter per wavenumber pair. 5. Long streamwise structures are reproduced more accurately.	1. The model is linear. 2. The estimation of the model parameters requires several estimations of the model outputs. 3. Under-estimates the flow velocity at peaks.

Table 7.1: Pros and cons of the spectral method, the POD method, the subdomain method and the dynamical model.

sation. A minor disadvantage of the parameterisation is that it uses a weighted norm which prioritise higher energy modes at the expense of modes containing lower energy. Consequently, the model was unable to reproduce some of the local maxima. We also stress that the spectral model was used only for wall quantities.

Flow reconstructions using the POD method dates back early 70's. The feature of the optimality of the POD modes with respect to other linear representations make the POD method an attractive tool for flow analysis. One of our key findings of the POD modes is the reconstruction ability of gappy fields. In the gappy plane Couette flow example, only 4.6% information was enough to get a reasonably good reconstruction using 400 modes. Our main contribution to the POD method is the development of a regularisation framework for high dimensional sparse fields. For the reconstructions of the flow velocity using only the wall temperature, we reproduced snapshots with $\gamma = 0.24$ when only 0.2% information was available. Although we emphasise the good quality of the reconstructions using the POD method, the evaluation of the POD modes require high computational cost. The POD method, like the spectral method, have limited capability to reproduce structures that are associated with lower energy.

We develop the subdomain method that evaluates modes within a subdomain. The most attractive feature of the subdomain modes are that they are locally optimised. These modes inherits all the properties of the POD modes. Since the computational costs for computing eigenvectors depends only on the number of snapshots, the computational costs for the subdomain POD method increase with the number of subdomains. On the other hand, the subdomain POD method does not need to be applied on the whole domain. Thus careful design of the subdomain topology is required to reduce the degrees of freedom. The continuity on the boundary of the subdomain is a challenging issue for the subdomain method. We used background fields to ensure the continuity. The disadvantage of background fields is that they require information at the boundaries of the subdomains.

The use of Dynamical models is perhaps the most elegant approach for flow reconstructions. There is no need to evaluate modes *a priori*, which is advantageous compared to the flow decomposition methods. Dynamical models provide physical constraints that emerges from the

governing equations whereas the decomposition methods are completely data-driven approach. The dynamical model developed here is a linear model- which is a drawback since the perturbed quantities are highly non-linear and chaotic. In contrast, the linear estimation theory is readily applicable to a linear model. Our model is a one-parametric model in the Fourier space. Thus the computational cost is comparatively low. However, the estimation of this model parameter required several estimations of the model outputs. The model accurately produced the long streamwise structures but was unable to reproduce the local peaks.

7.3 Future work

With this thesis, multiple opportunities have been open up. Some of the important possibilities are discussed below.

7.3.1 Reconstructing flows over non-homogeneous surfaces

Throughout the thesis, we considered flows over a homogeneous surface without any obstacles. Due to homogeneity, we were able to apply the Fourier transform in the streamwise and spanwise directions which eases the computational costs/difficulties. This would not be the case for a non-homogeneous surface, such as flow over a building [Xiao, 2016, Xiao et al., 2017, Podvin et al., 2006]. If modified, the methods we analysed in this thesis are applicable to flows with obstacles. It will be particularly interesting to investigate how flow decomposition methods can be utilised in this case to reconstruct flows from partial observations?

7.3.2 Optimal strategies for subdomain topology

One of the important conclusion in chapter 5 is the trade off between the computational costs and the reduction of the degrees of freedoms for the subdomain POD method. To reduce the degrees of freedom a suitable subdomain topology is required. In this thesis we used a topology for the 3D domain that works reasonably good, but did not emphasise on the optimal choice

for the topology. More insight is needed on how the topology should be chosen and how many modes are required in each subdomain - which is an interesting scope for future work.

7.3.3 Closure models for perturbed quantities

In chapter 6, we used a dynamical model which was linear under the assumption that the non-linear terms in $\mathbf{u}''$ and θ are random disturbances. This assumption can be improved by imposing a closure model for the terms quadratic in $\mathbf{u}''$ and θ. The closure model represents some imposed structures for the perturbed quantities. The eddy viscosity model was used by Illingworth and others along with a triple decomposition in channel flows [Illingworth et al., 2018] for the Orr-Sommerfeld-Squire system. It will be interesting to apply a closure to the dynamical model presented in this thesis using the Orr-Sommerfeld-Squire system and the scalar transport equation.

7.3.4 Application to other canonical flows

In this thesis, we investigated flow reconstruction methods only for shear-driven flow, namely plane Couette flow. It is therefore natural to consider other canonical flows, such as Rayleigh-Bénard convection [Ahlers et al., 2009, Grossmann and Lohse, 2000, van Reeuwijk et al., 2008]. In Rayleigh-Bénard, the important velocity component is the wall normal component as it is strongly correlated with the temperature distribution. It is also interesting to investigate flows due to pressure differences [Pirozzoli et al., 2016] as the pressure-velocity interactions play an important role in fluid dynamics.

Bibliography

[Ahlers et al., 2009] Ahlers, G., Grossmann, S., and Lohse, D. (2009). Heat transfer and large scale dynamics in turbulent Rayleigh-Bénard convection. *Reviews of Modern Physics*, 81(2):503–537.

[Antonia et al., 1988] Antonia, R. A., Krishnamoorthy, L. V., and Fulachier, L. (1988). Correlation between the longitudinal velocity fluctuation and temperature fluctuation in the near-wall region of a turbulent boundary layer. *International Journal of Heat and Mass Transfer*, 31(4):723–730.

[Barlow and Coceal, 2009] Barlow, J. F. and Coceal, O. (2009). A review of urban roughness sublayer turbulence. *Report*, (527):1–69.

[Bergin et al., 2005] Bergin, M. S., West, J. J., Keating, T. J., and Russell, A. G. (2005). Regional atmospheric pollution and transboundary air quality management. *Annual Review of Environment and Resources*, 30(1).

[Blocken et al., 2008] Blocken, B., Stathopoulos, T., and Carmeliet, J. (2008). Wind Environmental Conditions in Passages between Two Long Narrow Perpendicular Buildings. *Journal of Aerospace Engineering*, 21(4).

[Bui-Thanh et al., 2004] Bui-Thanh, T., Damodaran, M., and Willcox, K. E. (2004). Aerodynamic Data Reconstruction and Inverse Design Using Proper Orthogonal Decomposition. *AIAA Journal*, 42(8):1505–1516.

[Canuto, 1986] Canuto, C. (1986). Boundary Conditions in Chebyshev and Legendre Methods. *SIAM Journal on Numerical Analysis*, 23(4):815–831.

[Chapman, 1979] Chapman, D. R. (1979). Computational Aerodynamics Development and Outlook. *AIAA Journal*, 17(12).

[Colonius et al., 2002] Colonius, T., Rowley, C. W., Freund, J. B., and Murray, R. M. (2002). On the Choice of Norm for Modeling Compressible Flow Dynamics at Reduced-Order using the POD. In *IEEE Conference on Decision and Control*, Las Vegas, NV.

[Craske and Van Reeuwijk, 2015] Craske, J. and Van Reeuwijk, M. (2015). Energy dispersion in turbulent jets. Part 1. Direct simulation of steady and unsteady jets. *Journal of Fluid Mechanics*, 763:500–537.

[Deane and Sirovich, 1991] Deane, A. E. and Sirovich, L. (1991). A computational study of Rayleigh–Bénard convection. Part 1. Rayleigh-number scaling. *Journal of Fluid Mechanics*, 222:231–250.

[Debusschere and Rutland, 2004] Debusschere, B. and Rutland, C. J. (2004). Turbulent scalar transport mechanisms in plane channel and Couette flows. *International Journal of Heat and Mass Transfer*, 47(8-9):1771–1781.

[Douvi et al., 2015] Douvi, E., Douvi, E. C., and Margaris, D. P. (2015). Reducing the shear stress between the ship's hull and seawater by means of air cavity lubrication system. In *6th IC-EpsMsO*.

[Doyle et al., 1989] Doyle, J. C., Glover, K., Khargonekar, P. P., and Francis, B. a. (1989). State-space solutions to standard H2 and Hinf control problems. *IEEE Transactions on Automatic Control*, 34(8):831–847.

[Everson and Sirovich, 1995] Everson, R. and Sirovich, L. (1995). Karhunen – Lo ‘ eve procedure for gappy data. *Journal of Optical Society*, 12(8):2–9.

[Gal Berkooz et al., 1993] Gal Berkooz, Philip Holmes, and John L. Lumley (1993). The proper orthogonal decomposition in the analysis of turbulent flows. *Annu. Rev. Fluid Mech.*, 25:539–575.

[Gentian Zavalani, 2014] Gentian Zavalani (2014). Fourier Spectral Methods for Numerical Solving of the Kuramoto-Sivashinsky Equation. *Global Journal of Researches in Engineering*, 14(1):31–42.

[Giles and Pierce, 2000] Giles, M. B. and Pierce, N. A. (2000). An Introduction to the Adjoint Approach to Design. Technical report.

[Gouri Dhatt et al., 2012] Gouri Dhatt, Emmanuel Lefranois, Gilbert Touzot, and Emmanuel Lefrançois (2012). Finite Element Method.

[Grossmann and Lohse, 2000] Grossmann, S. and Lohse, D. (2000). Scaling in thermal convection: A unifying theory. *Journal of Fluid Mechanics*, 407:27–56.

[Haff et al., 2018] Haff, J., Schülein, E., Henning, A., Cochard, S., and Loose, S. (2018). Wall Shear Stress Measurements on a Double-Decker Train. In *New Results in Numerical and Experimental Fluid Mechanics XI*, pages 685–694.

[Haritonidis, 1989] Haritonidis, J. H. (1989). The Measurement of Wall Shear Stress. pages 229–261.

[Hetsroni et al., 2001] Hetsroni, G., Kowalewski, T. A., Hu, B., and Mosyak, A. (2001). Tracking of coherent thermal structures on a heated wall by means of infrared thermography. *Experiments in Fluids*, 30(3):286–294.

[Ho and Tai, 1998] Ho, C.-M. and Tai, Y.-C. (1998). Micro-Electro-Mechanical-Systems (MEMS) and fluid flows. *Annu. Rev. Fluid Mech*, 30:579–612.

[Hoepffner, 2006] Hoepffner, J. (2006). Stability and control of shear flows subject to stochastic excitations. *PhD Thesis*.

[Högberg, 2001] Högberg, M. (2001). *Optimal control of boundary layer transition*. PhD thesis.

[Holmes et al., 2012] Holmes, P., Lumley, J., Berkooz, G., and Rowley, C. (2012). Proper orthogonal decomposition. In *Turbulence, Coherent Structures, Dynamical Systems and Symmetry (Cambridge Monographs on Mechanics)*, pages 68–105. Cambridge: Cambridge University Press.

[Hyman and Nicolaenko, 1986] Hyman, J. M. and Nicolaenko, B. (1986). The Kuramoto-Sivashinsky equation: A bridge between PDE'S and dynamical systems. *Physica D: Nonlinear Phenomena*, 18(1-3).

[Illingworth et al., 2018] Illingworth, S. J., Monty, J. P., and Marusic, I. (2018). Estimating large-scale structures in wall turbulence using linear models. *Journal of Fluid Mechanics*, 842:146–162.

[Inagaki et al., 2013] Inagaki, A., Kanda, M., Onomura, S., and Kumemura, H. (2013). Thermal Image Velocimetry. *Boundary-Layer Meteorology*, 149(1):1–18.

[Johansson and Wikström, 2000] Johansson, A. V. and Wikström, P. M. (2000). DNS and modelling of passive scalar transport in turbulent channel flow with a focus on scalar dissipation rate modelling. *Flow, Turbulence and Combustion*, 63(1):223–245.

[Kasagi et al., 1992] Kasagi, N., Tomita, Y., and Kuroda, A. (1992). Direct numerical simulation of passive scalar field in a turbulent channel flow. *Journal of Heat Transfer*, 114(3):598–606.

[Kim and Bewley, 2007] Kim, J. and Bewley, T. R. (2007). A Linear Systems Approach to Flow Control. *Annual Review of Fluid Mechanics*, 39(1):383–417.

[Kowalewski et al., 2003] Kowalewski, T. A., Mosyak, A., and Hetsroni, G. (2003). Tracking of coherent thermal structures on a heated wall. 2. DNS simulation. *Experiments in Fluids*, 34(3):390–396.

[Lakestani and Dehghan, 2012] Lakestani, M. and Dehghan, M. (2012). Numerical solutions of the generalized Kuramoto–Sivashinsky equation using B-spline functions. *Applied Mathematical Modelling*, 36(2).

[Lateb et al., 2016] Lateb, M., Meroney, R. N., Yataghene, M., Fellouah, H., Saleh, F., and Boufadel, M. C. (2016). On the use of numerical modelling for near-field pollutant dispersion in urban environments - A review. *Environmental Pollution*, 208:271–283.

[Lee et al., 2001] Lee, K. H., Cortelezzi, L., Kim, J., and Speyer, J. (2001). Application of reduced-order controller to turbulent flows for drag reduction. *Physics of Fluids*, 13(5):1321–1330.

[Leu et al., 2016] Leu, T. S., Yu, J. M., Miau, J. J., and Chen, S. J. (2016). MEMS flexible thermal flow sensors for measurement of unsteady flow above a pitching wind turbine blade. *Experimental Thermal and Fluid Science*, 77:167–178.

[Lewis, 2012] Lewis, Frank L., D. V. V. L. S. (2012). *Optimal Control*, volume XXXIII.

[Liepmann and Skinner, 1954] Liepmann, E. W. and Skinner, G. T. (1954). Shearing-stress measurements by use of a heated element. Technical report, Technical Report NACA 3268.

[Liu, 2003] Liu, C. H. (2003). Turbulent plane couette flow and scalar transport at low Reynolds number. *Journal of Heat Transfer*, 125(6):988–998.

[Löfdahl and Gad-el Hak, 1999] Löfdahl, L. and Gad-el Hak, M. (1999). MEMS-based pressure and shear stress sensors for turbulent flows. *Meas. Sci. Technol*, 10:665–686.

[Lumley, 1967] Lumley, J. (1967). The Structure of Inhomogeneous Turbulent Flows. In: Yaglom, A.M. and Tartarsky, V.I., Eds. *Atmospheric Turbulence and Radio Wave Propagation*, pages 166–177.

[Maltby R. L., 1962] Maltby R. L. (1962). Flow Visualization in Wind Tunnels Using Indicators. Technical report.

[Manisalidis et al., 2020] Manisalidis, I., Stavropoulou, E., Stavropoulos, A., and Bezirtzoglou, E. (2020). Environmental and Health Impacts of Air Pollution: A Review. *Frontiers in Public Health*, 8.

[Mayer, 1998] Mayer, R. (1998). Chapter 1-3. In *Orientation on Quantitative IR-thermografy in Wall-shear Stress Measurements*, pages 1–18. Delft University Press.

[Moehlis et al., 2002] Moehlis, J., Smith, T. R., Holmes, P., and Faisst, H. (2002). Models for turbulent plane Couette flow using the proper orthogonal decomposition. *Physics of Fluids*, 14(7):2493–2507.

[Montazeri and Blocken, 2013] Montazeri, H. and Blocken, B. (2013). CFD simulation of wind-induced pressure coefficients on buildings with and without balconies: Validation and sensitivity analysis. *Building and Environment*, 60.

[Murray, 2006] Murray, R. M. (2006). *State estimation.*

[Nagano and Tagawa, 1995] Nagano, Y. and Tagawa, M. (1995). Coherent motions and heat transfer in a wall turbulent shear flow. *Journal of Fluid Mechanics*, 305(-1):127.

[Naqwi, 1993] Naqwi, A. A. (1993). Performance prediction of dual cylindrical wave laser devices for flow measurements. *Experiments in Fluids*, 14:132.

[Naughton and Sheplak, 2002] Naughton, J. W. and Sheplak, M. (2002). Modern developments in shear-stress measurement. *Progress in Aerospace Sciences*, 38(6-7):515–570.

[Oke, 1988] Oke, T. R. (1988). Street design and urban canopy layer climate. *Energy and Buildings*, 11(1-3):103–113.

[Oke et al., 2017] Oke, T. R., Mills, G., Christen, A., and Voogt, J. A. (2017). *Urban Climates.* Cambridge University Press, Cambridge.

[Örlü and Vinuesa, 2020] Örlü, R. and Vinuesa, R. (2020). Instantaneous wall-shear-stress measurements: advances and application to near-wall extreme events. *Measurement Science and Technology*, 31:112001.

[Ouro Barba et al., 2017] Ouro Barba, P., Stoesser, T., and Falconer, R. (2017). Large Eddy Simulation of Tidal Turbines. Technical report.

[Papageorgiou, 1991] Papageorgiou, D. T. (1991). Theoretical and Computational Fluid Dynamics The Route to Chaos for the Kuramoto-Sivashinsky Equation 1. *Theoretical and Computational Fluid Dynamics*, 3:15–42.

[Pirozzoli et al., 2014] Pirozzoli, S., Bernardini, M., and Orlandi, P. (2014). Turbulence statistics in Couette flow at high Reynolds number. *Journal of Fluid Mechanics*, 758(1956):327–343.

[Pirozzoli et al., 2016] Pirozzoli, S., Bernardini, M., and Orlandi, P. (2016). Passive scalars in turbulent channel flow at high Reynolds number. *Journal of Fluid Mechanics*, 788:614–639.

[Podvin et al., 2006] Podvin, B., Fraigneau, Y., Lusseyran, F., and Gougat, P. (2006). A reconstruction method for the flow past an open cavity. *Journal of Fluids Engineering*, 128(3):531.

[Protas et al., 2004] Protas, B., Bewley, T. R., and Hagen, G. (2004). A computational framework for the regularization of adjoint analysis in multiscale PDE systems. *Journal of Computational Physics*, 195(1):49–89.

[Quarteroni, 1987] Quarteroni, A. (1987). Domain decomposition techniques using spectral methods. *CALCOLO*, 24:141–177.

[Reda and Muratore, 1994] Reda, D. C. and Muratore, J. J. (1994). A new technique for the measurement of surface shear stress vectors usingliquid crystal coatings. In *32nd Aerospace Sciences Meeting and Exhibit*.

[S. C. Reddy et al., 1998] S. C. Reddy, J.A.C. Weideman, and G.F. Norris (1998). On a Modified Chebyshev Pseudospectral Method. Technical report.

[Schmid, 2010] Schmid, P. J. (2010). Dynamic mode decomposition of numerical and experimental data. *Journal of Fluid Mechanics*, 656:5–28.

[Schmid and Henningson, 2001] Schmid, P. J. and Henningson, D. S. (2001). *Stability and Transition in Shear Flows*, volume 142. Springer New York, New York, NY.

[Schwertfirm and Manhart, 2007] Schwertfirm, F. and Manhart, M. (2007). DNS of passive scalar transport in turbulent channel flow at high Schmidt numbers. *International Journal of Heat and Fluid Flow*, 28(6):1204–1214.

[Sieber et al., 2016] Sieber, M., Paschereit, C. O., and Oberleithner, K. (2016). Spectral proper orthogonal decomposition. *Journal of Fluid Mechanics*, 792:798–828.

[Sirovich, 1987] Sirovich, L. (1987). Turbulence and the dynamics of coherent structures. II. Symmetries and transformations. *Quarterly of Applied Mathematics*, 45(3):573–582.

[Sirovich, 1989] Sirovich, L. (1989). Chaotic dynamics of coherent structures. *Physica D: Nonlinear Phenomena*, 37(1-3):126–145.

[Sirovich and Deane, 1991] Sirovich, L. and Deane, A. E. (1991). A computational study of Rayleigh–Bénard convection. Part 2. Dimension considerations. *Journal of Fluid Mechanics*, 222:251–265.

[Sirovich et al., 1990] Sirovich, L., Kirby, M., and Winter, M. (1990). An eigenfunction approach to large scale transitional structures in jet flow. *Physics of Fluids A: Fluid Dynamics*, 2(2):127–136.

[Taha, 2004] Taha, H. (2004). Heat Islands and Energy. In *Encyclopedia of Energy*. Elsevier.

[Taira et al., 2017] Taira, K., Brunton, S. L., Dawson, S. T. M., Rowley, C. W., Colonius, T., McKeon, B. J., Schmidt, O. T., Gordeyev, S., Theofilis, V., and Ukeiley, L. S. (2017). Modal Analysis of Fluid Flows: An Overview. *The American Institute of Aeronautics and Astronautics, Inc.*

[Tanner, 1977] Tanner, L. H. (1977). A skin friction meter, using the viscosity balance principle, suitable for use with flat or curved metal surfaces (based on thickness measurement). *Journal of Physics E: Scientific Instruments*, pages 278–284.

[Tanner and Blows, 1976] Tanner, L. H. and Blows, L. G. (1976). A study of the motion of oil films on surfaces in air flow, with application to the measurement of skin friction. *Journal of Physics E: Scientific Instruments*, pages 194–202.

[Trentelman et al., 2002] Trentelman, H. L., Stoorvogel, A. A., and Hautus, M. (2002). Control theory for linear systems. Technical report.

[Tsukahara et al., 2006] Tsukahara, T., Kawamura, H., and Shingai, K. (2006). DNS of turbulent Couette flow with emphasis on the large-scale structure in the core region. *Journal of Turbulence*, 7(June 2015):N19.

[United Nations, 2014] United Nations (2014). World Urbanization Prospects: The 2014 Revision, Highlights.

[United Nations, 2019] United Nations (2019). World Population Prospects 2019 Highlights. Technical report.

[Van Pul et al., 1994] Van Pul, W. A. J., Holtslag, A. A. M., and Swart, D. P. J. (1994). A comparison of ABL heights inferred routinely from lidar and radiosondes at noontime. *Boundary-Layer Meteorology*, 68(1-2):173–191.

[van Reeuwijk et al., 2008] van Reeuwijk, M., Jonker, H. J. J., and Hanjalić, K. (2008). Wind and boundary layers in Rayleigh-Bénard convection. I. Analysis and modeling. *Physical Review E*, 77(3):036311(1).

[Verstappen and Veldman, 2003] Verstappen, R. and Veldman, A. (2003). Symmetry-preserving discretization of turbulent flow. *Journal of Computational Physics*, 187(1).

[Waleffe, 1997] Waleffe, F. (1997). On a self-sustaining process in shear flows. *Physics of Fluids*, 9(June 1996):883.

[Wallace et al., 2006] Wallace, J. M., Brodkey, R. S., and Eckelmann, H. (2006). Pattern-recognized structures in bounded turbulent shear flows. *Journal of Fluid Mechanics*, 83(4):673–693.

[Wang et al., 2012] Wang, Z., Akhtar, I., Borggaard, J., and Iliescu, T. (2012). Proper orthogonal decomposition closure models for turbulent flows: A numerical comparison. *Computer Methods in Applied Mechanics and Engineering*, 237-240:10–26.

[Wiener, 2010] Wiener, N. (2010). PLANCHEREL'S THEOREM. In *The Fourier Integral and Certain of its Applications*, pages 46–71. Cambridge University Press.

[Winter, 1977] Winter, K. G. (1977). An outline of the techniques available for themeasurement of skin-friction in turbulent boundarylayers. *Progress in Aerospace Sciences.*, 18:57.

[World Health Organization, 2016] World Health Organization (2016). Ambient air pollution: A global assessment of exposure and burden of disease. Technical report.

[Xiao, 2016] Xiao, D. (2016). *Non-Intrusive reduced order methods.* PhD thesis, Imperial College London.

[Xiao et al., 2017] Xiao, D., Fang, F., Pain, C. C., and Navon, I. M. (2017). Domain decomposition non-intrusive reduced order modelling of non-linear flow dynamics.

[Yamaleev et al., 2008] Yamaleev, N., Diskin, B., Yamaleev, N. K., Diskin, B., and Nielsen, E. J. (2008). Adjoint-Based Methodology for Time-Dependent Optimization Solver Technology for Turbulent Flows View project Grid Generation for "Solver Technology for Turbulent flows" View project Adjoint-based Methodology for Time-Dependent Optimization.

[Zhao, 2018] Zhao, J. (2018). Measurement of Wall Shear Stress in High Speed Air Flow Using Shear-Sensitive Liquid Crystal Coating. *Sensors (Basel, Switzerland)*, 18(5):–undefined.

Appendix A

Plancherel's theorem for Reynolds-averaged quantities

Plancherel's theorem: If A and B are two real valued square integrable periodic functions with Fourier series [Wiener, 2010]

$$A(x,y) = \sum_{n_x}\sum_{n_y} \hat{a} \exp\left(2\pi i \left(\frac{n_x x}{L_x} + \frac{n_y y}{L_y}\right)\right), \tag{A.1a}$$

$$B(x,y) = \sum_{n_x}\sum_{n_y} \hat{b} \exp\left(2\pi i \left(\frac{n_x x}{L_x} + \frac{n_y y}{L_y}\right)\right) \tag{A.1b}$$

where, L_x, L_y are the periods in x and y dimension respectively. The quantities $\hat{a}$ and $\hat{b}$ are given as

$$\hat{a}(n_x, n_y) = \frac{1}{L_x L_y} \int_0^{L_x}\int_0^{L_y} A \exp\left(-2\pi i \left(\frac{n_x x}{L_x} + \frac{n_y y}{L_y}\right)\right) \mathrm{d}y\,\mathrm{d}x \tag{A.2}$$

and

$$\hat{b}(n_x, n_y) = \frac{1}{L_x L_y} \int_0^{L_x}\int_0^{L_y} B \exp\left(-2\pi i \left(\frac{n_x x}{L_x} + \frac{n_y y}{L_y}\right)\right) \mathrm{d}y\,\mathrm{d}x \tag{A.3}$$

then the Plancherel's theorem states that

$$\int_0^{L_x}\int_0^{L_y} AB\,\mathrm{d}y\,\mathrm{d}x = L_x L_y \sum_{n_x}\sum_{n_y} \hat{a}^* \hat{b} \tag{A.4}$$

Now, we apply the Plancherel's theorem to the distributions of the wall shear stress and the thermal wall patterns. Let us suppose $\hat{\tau}_w\left(n_x, n_y, t\right)$ and $\hat{\theta}_w\left(n_x, n_y, t\right)$ are the Fourier coefficients of the wall shear stress $\tau_w(x, y, t)$ and the thermal wall patterns $\theta_w(x, y, t)$ respectively. Then using the Plancherel's theorem we write as,

$$\int_0^{L_x}\int_0^{L_y} \theta_w \tau_w \,\mathrm{d}y\,\mathrm{d}x = L_x L_y \sum_{n_x}\sum_{n_y} \hat{\theta}_w^* \hat{\tau}_w \tag{A.5}$$

Here, L_x, L_y are the length and width of the wall respectively. Since, the wall shear stress and the thermal wall patterns are functions of space and time, both the spatial average and average over wavenumber space will remain time dependent. Now taking the time average over the equation A.5 and multiplying the factor $1/(L_x L_y)$ on both sides

$$\overline{\theta_w \tau_w} = \frac{1}{T}\int_0^T \sum_{n_x}\sum_{n_y} \hat{\theta}_w^* \hat{\tau}_w \,\mathrm{d}y = \left\langle \sum_{n_x}\sum_{n_y} \hat{\theta}_w^* \hat{\tau}_w \right\rangle = \sum_{n_x}\sum_{n_y} \langle \hat{\theta}_w^* \hat{\tau}_w \rangle$$

That is,

$$\overline{\theta_w \tau_w} = \sum_{n_x}\sum_{n_y} \langle \hat{\theta}_w^* \hat{\tau}_w \rangle \tag{A.6}$$

The left hand side of A.6 can be written as

$$\begin{aligned}
\overline{\theta_w \tau_w} &= \overline{\left(\overline{\theta}_w + \theta'_w\right)\left(\overline{\tau}_w + \tau'_w\right)} \\
&= \overline{\overline{\theta}_w \overline{\tau}_w + \overline{\theta}_w \tau'_w + \theta'_w \overline{\tau}_w + \theta'_w \tau'_w} \\
&= \overline{\overline{\theta}_w \overline{\tau}_w} + \overline{\overline{\theta}_w \tau'_w} + \overline{\theta'_w \overline{\tau}_w} + \overline{\theta'_w \tau'_w} \\
&= \overline{\theta}_w \overline{\tau}_w + \overline{\theta'_w \tau'_w}
\end{aligned}$$

That is,

$$\overline{\theta_w \tau_w} = \overline{\theta}_w \overline{\tau}_w + \overline{\theta'_w \tau'_w} \tag{A.7}$$

Next, we write the expression $\langle\hat{\theta}_w^*\hat{\tau}_w\rangle$ on the right side of the equation A.6 as,

$$\begin{aligned}
\langle\hat{\theta}_w^*\hat{\tau}_w\rangle &= \left\langle\left(\langle\hat{\theta}_w\rangle^* + \hat{\theta}_w''^*\right)\left(\langle\hat{\tau}_w\rangle + \hat{\tau}_w''\right)\right\rangle \\
&= \left\langle\langle\hat{\theta}_w\rangle^*\langle\hat{\tau}_w\rangle + \langle\hat{\theta}_w\rangle^*\hat{\tau}_w'' + \hat{\theta}_w''^*\langle\hat{\tau}_w\rangle + \hat{\theta}_w''^*\hat{\tau}_w''\right\rangle \\
&= \left\langle\langle\hat{\theta}_w^*\rangle\langle\hat{\tau}_w\rangle\right\rangle + \left\langle\langle\hat{\theta}_w^*\rangle\hat{\tau}_w''\right\rangle + \left\langle\hat{\theta}_w''^*\langle\hat{\tau}_w\rangle\right\rangle + \langle\hat{\theta}_w''^*\hat{\tau}_w''\rangle \\
&= \langle\hat{\theta}_w^*\rangle\langle\hat{\tau}_w\rangle + \langle\hat{\theta}_w^*\rangle\langle\hat{\tau}_w''\rangle + \langle\hat{\theta}_w''^*\rangle\langle\hat{\tau}_w\rangle + \langle\hat{\theta}_w''^*\hat{\tau}_w''\rangle \\
&= \langle\hat{\theta}_w^*\rangle\langle\hat{\tau}_w\rangle + \langle\hat{\theta}_w''^*\hat{\tau}_w''\rangle
\end{aligned}$$

Then the right side of the equation A.6 can be written as,

$$\sum_{n_x}\sum_{n_y}\langle\hat{\theta}_w^*\hat{\tau}_w\rangle = \sum_{n_x}\sum_{n_y}\left(\langle\hat{\theta}_w^*\rangle\langle\hat{\tau}_w\rangle + \langle\hat{\theta}_w''^*\hat{\tau}_w''\rangle\right)$$

The first term in the right side includes temporal averages of the Fourier coefficients, which vanish except for the pair $(n_x, n_y) = (0, 0)$. Assuming the time period T is sufficiently large, we can write

$$\sum_{n_x}\sum_{n_y}\langle\hat{\theta}_w^*\hat{\tau}_w\rangle = \langle\hat{\theta}_w^*(0,0)\rangle\langle\hat{\tau}_w(0,0)\rangle + \sum_{n_x}\sum_{n_y}\langle\hat{\theta}_w''^*\hat{\tau}_w''\rangle = \overline{\theta}_w\overline{\tau}_w + \sum_{n_x}\sum_{n_y}\langle\hat{\theta}_w''^*\hat{\tau}_w''\rangle \tag{A.8}$$

Now, we use the results in the equations A.7 and A.8 in the equation A.6, and cancelling the common term $\overline{\theta}_w\overline{\tau}_w$ from the both sides as

$$\overline{\theta_w'\tau_w'} = \sum_{n_x}\sum_{n_y}\langle\hat{\theta}_w''^*\hat{\tau}_w''\rangle \tag{A.9}$$

Similarly, it can be shown that,

$$\overline{\theta_w'^2} = \sum_{n_x}\sum_{n_y}\langle\hat{\theta}_w''^*\hat{\theta}_w''\rangle, \quad \overline{\tau_w'^2} = \sum_{n_x}\sum_{n_y}\langle\hat{\tau}_w''^*\hat{\tau}_w''\rangle. \tag{A.10a-b}$$